国際化推進共同研究概要

No. 1

22EA-1

タ イ ト ル： Dynamical mechanisms of stratospheric control on the tropical troposphere and ocean

研究代表者： UEYAMA Rei

所内世話人： 江口　菜穂

研 究 概 要： 2002 年 8 月 8 日から 9 日にかけて、記録的な大雨が朝鮮半島と日本北部を含む東アジアで発生した。 このいわゆる「100 年洪水イベント」は、境界層汚染物質の全球成層圏への深い対流輸送の影響を研究するための NASA の航空機キャンペーン(The Asian summer monsoon Chemical and Climate Impact Project; ACCLIP)中に発生した。 本報告書では、この記録的な大雨の原因となった上部対流圏と下部成層圏領域での力学過程に関して解析した結果を示す。その解析の過程で、物質循環の理解を容易にする全球対流雲頂高度 [Pfister, Ueyama, et al., 2022] と温位データセットを開発した。これらのデータと客観解析データの初期解析結果から、2022 年 8 月の大雨イベントの物理的要因として、成層圏と対流圏の相互作用に関連する背の高い deep convective clouds の陸域での広域な発生とそれに関連する偏西風の分岐および強化が関係していることを示唆された。

Dynamical Mechanisms of Stratospheric Control on the Tropical Troposphere and Ocean

Rei Ueyama (NASA Ames Research Center)

I. Abstract

On August 8 to 9, 2002, a record rainfall event occurred over eastern Asia including the Korean peninsula and northern Japan. This so-called "100-yr flooding event" occurred during one of NASA's airborne campaigns to study the impact of deep convective transport of boundary layer pollutants to the global stratosphere. We develop a critical dataset of global convective cloud top altitudes and potential temperatures to facilitate the analysis of in situ measurements in the upper troposphere and lower stratosphere. The ultimate objective is to improve process-level understanding of stratosphere and troposphere interactions, such as the mechanism of the heavy rainfall event of August 2022 which appears to have been related to deep convective activity in the tropics.

II. Introduction

One of the important mechanisms of stratosphere and troposphere exchange (STE) is deep convection that detrains mass in the upper troposphere and lower stratosphere (UTLS). These convective storms are especially strong and frequent over the Asian and North American monsoon regions during boreal summer (ASM and NAM, respectively). Water vapor and boundary layer pollutants lofted by deep monsoon convection are typically trapped within the strong anticyclonic circulation in the UTLS and later dispersed throughout the global stratosphere, where they can have a significant impact on radiative and chemical processes, potentially including stratospheric ozone.

The Asian summer monsoon Chemical and Climate Impact Project (ACCLIP) deployed two aircraft – NSF GV and NASA WB-57 – from South Korea during Jul-Aug 2022 to obtain in situ measurements of UTLS composition in the region of ASM outflow to characterize the impact of the ASM on global chemistry and climate (https://espo.nasa.gov/acclip/content/ACCLIP). Overshooting convective storms (i.e., deep convection that penetrates the tropopause) were the target of another recent NASA airborne campaign, Dynamics and Chemistry of the Summer Stratosphere (DCOTSS), which measured the composition of these overshooting convective plumes within the North American monsoon region during summers 2021 and 2022 (https://dcotss.geos.tamu.edu/). The main objective of the DCOTSS mission was to determine the effects of these overshooting storms on the dynamics, chemistry and composition of the stratosphere. Both aircraft campaigns successfully completed their measurement phases, and data calibration and quality checks are currently underway.

In order to place these in situ measurements from ACCLIP and DCOTSS campaigns within the context of large-scale meteorology and examine the dynamical interactions between the stratosphere and troposphere, there is a need for a global dataset of observation-based estimates of deep convection. In this study, we developed and finalized the algorithm for calculating such a global convection dataset and furthermore analyzed Aug 2022 data to explore the mechanism of the "100-yr flooding event" that occurred in South Korea during the ACCLIP deployment.

III. Method/Data

The key datasets used in this study are JRA-55 reanalysis data, NOAA outgoing longwave radiation (OLR) data, surface precipitation measurements from Global Precipitation Climatology Project (GPCP), and satellite-derived global convective cloud top altitudes (Pfister et al, 2022). In particular, the main focus of this year's activity was to finalize the algorithm for the satellite-derived cloud top dataset and publish its methodology in a peer-reviewed journal.

The approach for calculating convective cloud top altitudes and potential temperatures uses the statistics of CloudSat cloud radar deep convective cloud classification product coupled with nighttime CALIOP lidar measurements to effectively "calibrate" the high frequency, high resolution global rainfall and brightness temperature data that is used to derive convective cloud top altitudes. Thus, our product agrees well with the statistics of the CloudSat/CALIOP convective cloud tops, especially in the tropics and over oceanic regions. Agreement is reasonable, but not as good, for land-based convection. The estimated uncertainty in cloud top altitudes in our product is 0.5 – 1.0 km over land areas, with smaller uncertainties over the oceans. The diurnal cycle of the new convection dataset is in good agreement with precipitation radar convective climatology.

IV. Results

Figure 1 shows the incidence of deep convective cloud tops that extend above the local tropopause averaged over December 2006 through November 2009 based on our published algorithm (Pfister et al., 2022). This can be compared with GPM radar climatology (Figure 2c of Liu et al., 2020), but note that absolute values are different because the radar measurements require a minimum dbZ value above the tropopause, whereas our satellite-derived methodology merely indicates that convective cloud is present. Nonetheless, major areas of agreement (and disagreement) are largely where we might expect them based on the nature of the datasets. For example, Fig. 1 largely captures most of the convective land features in the radar-based climatology. However, oceanic convection is more prominent than land convection in our product, clearly opposite from the radar data. Two plausible explanations are as follows: (1) the radar mainly captures the larger particles, which are more likely to be lofted by the substantially higher vertical velocities in land-based convection (Lucas, et al., 1994), and misses the small particles lofted by weaker oceanic convection; and (2) our product has difficulty representing land-based convection as compared to CloudSat/CALIOP data, especially during boreal winter.

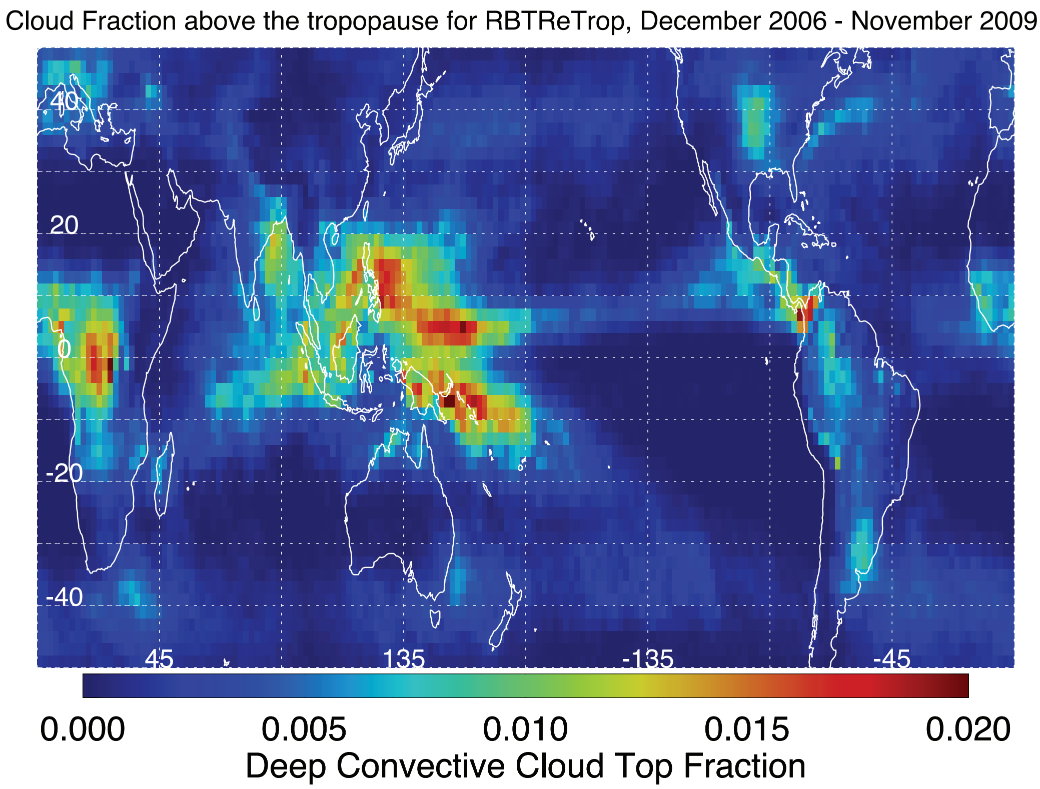

Figure 1: Incidence of deep convection above the NCAR/NCEP reanalysis local tropopause at all times, averaged over 3 years (Dec 2006 – Nov 2009) using the algorithm described in Pfister et al. (2022).

Despite some limitations of the satellite-derived convective cloud top dataset (see Pfister et al., 2002 for details), we have found this product to be very useful in identifying stratospheric-driven response of the troposphere as well as for estimating the degree of stratosphere-troposphere coupling as represented by the altitudes of the deep convective clouds. For example, we found that the "100-yr flooding event" in South Korea (as well as in other parts of eastern Asia including northern Japan) was associated with a zonally-elongated band of convection with anomalously high cloud tops (above 16 km) extending from central China, as shown in Figure 2.

Further analyses revealed that the heavy rainfall over eastern Asia was coupled to enhanced deep convective activity in the tropics especially near Bay of Bengal. A broad region of anomalously deep convective clouds penetrating the tropical tropopause layer (TTL) forced a large-scale meridional circulation with anomalous descent across the Tibetan Plateau, as shown in Figure 3. Associated with this is a northward transport of warm and moist tropical air characterized by low potential vorticity. Preliminary results also indicate the role of Rossby waves and the modulation of the subtropical and low-level jets, though further investigation is needed.

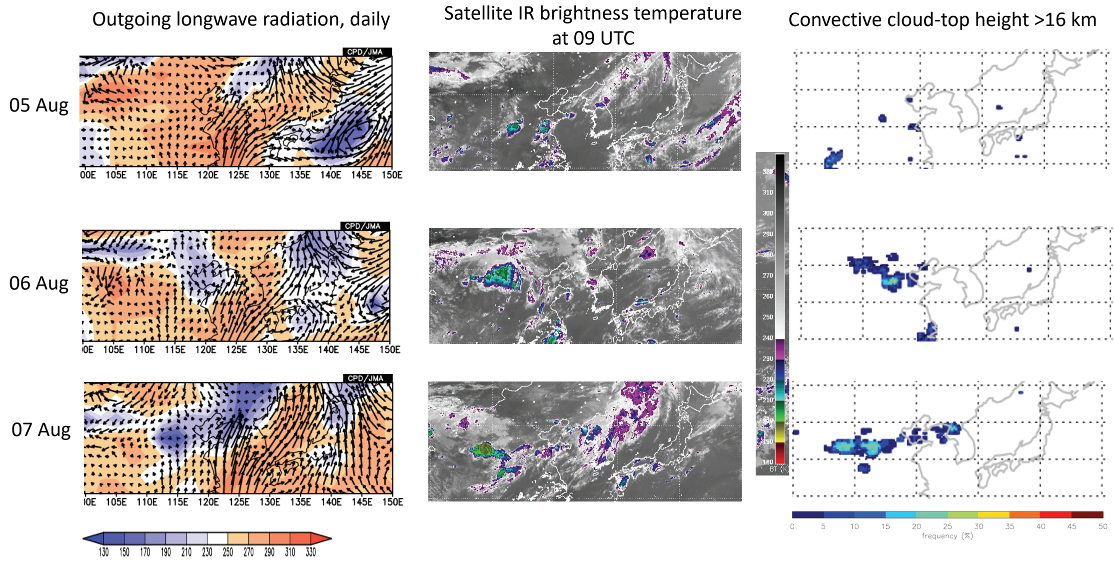

Figure 2: Time sequence from 5 to 7 August 2022 of the convection development as seen in (left) daily outgoing longwave radiation, (middle) once daily satellite IR brightness temperatures at 09 UTC, and (right) occurrence frequency of satellite-derived convective cloud top height above 16 km. The "100-yr flooding event" occurred in South Korea after this sequence of events on 8-9 August 2022.

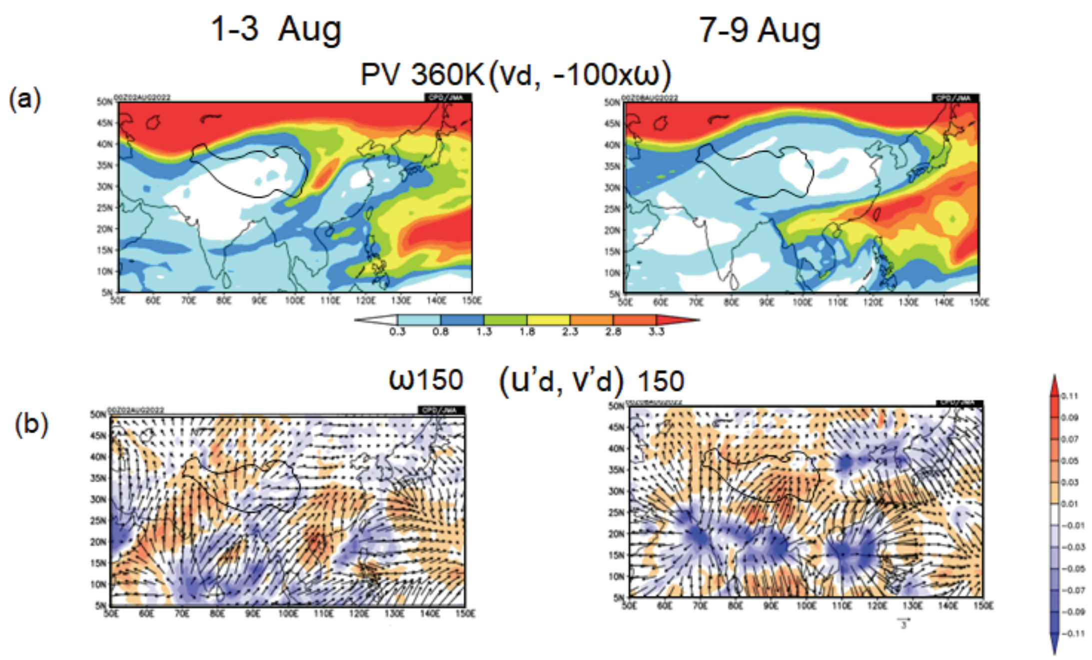

Figure 3: 3-day mean centered on August 2 (left) and 8 (right) of the (a) potential vorticity field at 360 K level and (b) vertical pressure velocity and divergence winds at 150 hPa level (blue represents ascent, red represents descent).

V. Discussion/Summary

In this study, we calculated high temporal (3-hourly) and spatial (quarter degree) resolution data of convective cloud top altitude and potential temperature. We used cloud radar (CloudSat) to calibrate the convective thresholds estimated using rainfall data, and space-based lidar (CALIOP) to calibrate the cloud top height using IR data. We find reasonable agreement with convective cloud top climatologies based on precipitation radar, microwave, and cloud radar data. The statistics of the diurnal variations of this product (not shown here) are also consistent with the statistics from the radar datasets. This global convection dataset is used to estimate the strength and distribution of deep convective activity during the recent ACCLIP and DCOTSS campaigns, and will be analyzed in conjunction with the airborne measurements as they become available in the coming months. Our convection dataset was also analyzed to investigate the cause of the heavy rainfall event which occurred on 8-9 August 2022. Preliminary results suggest that a broad region of enhanced deep convective activity in the tropics with frequent cloud top penetration into the TTL may have induced an anomalously strong meridional circulation, forcing anomalous wave activity and jet structure.

VI. References

Liu, N., Liu, C., and Hayden, L., 2020: Climatology and detection of overshooting convection from 4 years of GPM precipitation radar and passive microwave observations, Journal of Geophysical Research: Atmospheres, 125, https://doi.org/10.1029/2019JD032003.

Lucas, C., Zipser, E. J., and LeMone, M. A., 1994: Vertical velocity in oceanic convection off tropical Australia, Journal of the Atmospheric Sciences, 51(21), 3183-3193.

Pfister, L., Ueyama R., Jensen E., and Schoeberl, M., 2022: Deep convective cloud top altitudes at high temporal and spatial resolution, Earth and Space Science, 9, e2002EA002475. https://doi.org/10.1029/2022EA002475.

VII. List of Publications

Pfister, L., Ueyama R., Jensen E., and Schoeberl, M., 2022: Deep convective cloud top altitudes at high temporal and spatial resolution, *Earth and Space Science*, 9, e2002EA002475. https://doi.org/10.1029/2022EA002475.

VIII. Research meeting and discussion

Rei Ueyama visited Japan between 17 and 27 December 2022 where she met with Dr. Nawo Eguchi and Dr. Kunihiko Kodera for various research discussions. She gave an online seminar (大気科学セミナー) on 22 December 2022, and visited RIAM on 26 December 2022.

IX. Additional information

Rei Ueyama participated in the ACCLIP campaign as a Lead Meteorologist and in the DCOTSS campaign as the Forecasting and Flight Planning Lead.

X. Other members of the joint research team

	RIAM, Kyushu University
Nawo Eguchi	
Kunihiko Kodera	Meteorological Research Institute

国際化推進共同研究概要

No. 2

22EA-2

タ イ ト ル： Analysis of ground-based and satellite observations of ice/liquid precipitation

研究代表者： BALDINI Luca

所内世話人： 佐藤　可織

研 究 概 要：大陸全域での降水量収支の推定に衛星観測が主要な役割を果たす南極大陸等において、悪天候下での連続観測に適した 24GHz 帯地上レーダとレーザーディスドロメータの複合利用から、衛星推定量の検証やブラインドゾーンでの減衰のない 94GHz 帯衛星ミリ波レーダ・ドップラースペクトラムのシミュレーションを可能とする新手法の開発と検証を行った。提案の手法は、南極大陸等における降水量収支推定の向上をはじめ、ドップラー機能を有する衛星ミリ波レーダの観測量や解析プロダクトの検証に役立つと期待される。

Analysis of ground-based and satellite observations of ice/liquid precipitation

Dr. Luca Baldini

National Research Council of Italy, Institute of Atmospheric Sciences and Climate

Rome, Italy

Summary

Research activity has been focused on the challenging environment of Antarctica. Ground-based snowfall observations over Antarctica are rare due to the harsh environment and high logistical, equipment maintenance, and operational costs. Satellite measurements are therefore crucial to provide continent-wide precipitation estimates and this highlights the importance of validating the satellite estimates with measurements collected by ground-based instrumentation for precipitation measurements available at the different Antarctic stations.

The NASA CloudSat satellite, launched in 2006, equipped with a 94 GHz Cloud Profiling Radar (CPR) that provides measurements of reflectivity profiles of clouds and precipitation, has been the major sources of satellite data for precipitation in Antactica. This role it will be played by the incoming ESA/JAXA EarthCARE mission that will add Doppler capability to a 94 GHz radar along with a multisensory payload.

This joint research has explored how the synergy between two instruments available at most Antarctic stations, i.e., the Micro Rain Radar (24 GHz) and laser disdrometer, can be exploited to validate satellite-borne W-band radar measurements, including the Doppler estimates of EarthCARE.

A new validation methodology (K2W) was proposed to combine these instruments for simulating the 94 GHz reflectivity and Doppler measurements from Micro Rain Radar spectra. Assessment of the proposed K2W conversion methodology showed that the CloudSat Ze profiles can be simulated by the method with 0.2 dB mean difference at the lowest satellite radar range bin when time lag within ±12.5 minutes and the distance within 25 km around the CloudSat overpass were considered. With the K2W method, the 94 GHz Doppler velocity below 1 km altitude that would be observed by EarthCARE was obtained, and the standard deviation of the simulated Doppler velocity was found to be smaller than about 0.2 m s-1. Reserchers are confident that the proposed technique, will significantly improve the quantification of precipitation over Antarctica. This methodology is proposed to assess the EarthCARE CPR Doppler velocity measurement accuracy as well as the Level 2 standard products for precipitation in Antarctica and at many other ground observation sites.

Development of K2W

A conversion methodology (K2W) to simulate the W band radar reflectivity and Doppler profiles from ground-based Micro Rain Radar at 24 GHz and laser disdrometer observations, at Antarctic research stations, differently from imaging disdrometer or Ka or W band radar profilers. This instrumentation can also be deployed in harsh and extreme regions, such as other stations in Antarctica, thus increasing the number of validation sites.

To develop the methodology, we have exploited observations from ground-based instruments (i.e., Micro Rain Radar and Parsivel disdrometer) running at the Italian research station “Mario Zucchelli” (MZS), managed by the Italian Antarctic Research Program, located at Terra Nova Bay along the Ross Sea coast of Northern Victoria Land. The MRR was originally designed to detect rainfall, using the relationship between velocity and diameter of falling raindrops. When MRR is employed to measure snow, specific procedures must be applied to improve the sensitivity and obtain dependable snow observations.

Laser disdrometers are widely used to detect the distribution of liquid hydrometeor size and more recently have been also used to determine the particle size distribution (PSD) of solid hydrometeors despite some well-known limitations. In this respect, disdrometers are particularly prone to artifacts in the presence of horizontal wind, as the detection of hydrometeors assumes that particles pass across the measurement area with a vertical trajectory rather than in a slanted path as likely happens in the case of strong wind. Such shortcomings are particularly significant when studying snowfall due to the smaller fall velocity of snow particles than that of raindrops. To mitigate the influence of wind on disdrometer measurements a filter based on reported relationships for raindrop falling velocity was used.

The proposed K2W methodology simulates W-band spectra (target band) from MRR K-band spectra (band of measurements) using appropriate backscattering cross- sections $\sigma(D)$ and $v_t(D)$ terminal velocity-diameter relationship for precipitation with the aid of Parsivel observations and electromagnetic scattering theories. Details of the proposed K2W methodology are provided in Bracci et al. (2023)[1]. The method can be used for any target band, such as Ka.

Validation

For the satellite data, we used the 94 GHz CloudSat radar reflectivity factor data. The CloudSat Ze profiles after hydrometeor/surface clutter masking and correction for gaseous attenuation were further matched to the vertical resolution of MRR. A typical precipitation event over MZS observed by CloudSat was analyzed. The lowest radar range bins with a confidence level of 40, which indicates a high probability of a strong echo from hydrometeors, were compared to MRR.

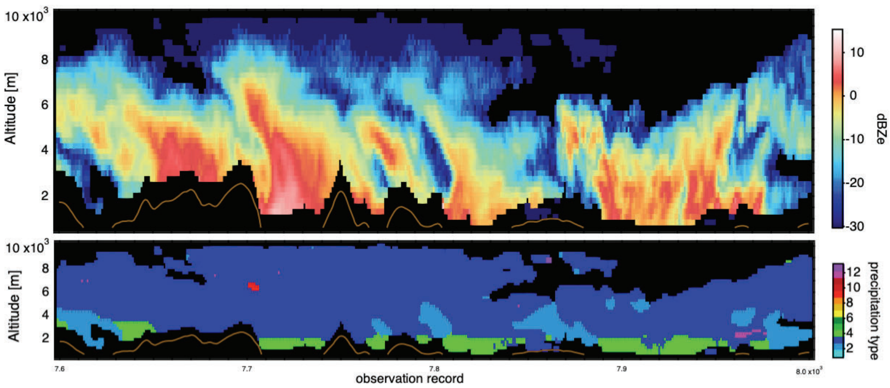

Fig. 1. Validation of the K2W methodology with CloudSat reflectivity profiles during overpass of the satellite

Vertical profiles of W-band reflectivity obtained by K2W around the CloudSat overpass were averaged for comparison with the averaged CloudSat Z_e profiles within a certain distance from MZS. To properly compare satellite and MRR profiles, we computed the mean value of MRR reflectivity using 4 range bins above and 4 range bins below the corresponding CloudSat bins to obtain a similar vertical resolution. It is expected that relatively short spatial and time averaging would provide a good match in the comparison considering the transition of the cloud system.

As horizontal wind speed at the ground during the overpass was around 15 m s^{-1} (about 1 km min^{-1}), we considered this a first approximation of the moving speed of the precipitating system to estimate the one-to-one correspondence between the time and spatial averaging scales. Intensive sensitivity analyses were further conducted to take into account the spatial variability of the precipitation system during the satellite overpass. The Satellite and K2W W-band profiles showed very good agreement with each other. The difference between the W-band and CloudSat was only 0.2 dB at 760 m, 1 dB at 960 m, and about 0.5 dB root mean square difference considering both range bins. It was also found that the K2W procedure developed in this joint research performed better than the empirical formula proposed in previous studies (e.g., Maahn et al. JGR., 2014), which significantly underestimated the CloudSat profiles. The potential of the proposed methodology was further highlighted in Bracci et al, (2023)[1], which showed the estimated Doppler velocity profile in the W-band with standard deviation smaller than about 0.2 m s^{-1}. The ability to derive the 94 GHz Doppler profiles from the MRR K-band Doppler spectrum in addition to the radar reflectivity profiles, regardless of the satellite blind zone, could also be useful for comparing and validating measurements of satellite missions equipped with Doppler observations, such as the upcoming ESA/JAXA EarthCARE mission that will add Doppler capability to 94 GHz radar.

Selected list of co-publications:

<u>Journal paper</u>

[1] *Bracci, A., Sato, K., Baldini, L., Porcù, F. and Okamoto, H.*

"Development of a methodology for evaluating spaceborne W-band Doppler Radar by combined use of Micro Rain Radar and a disdrometer in Antarctica", *Remote Sensing of Environment (in revision), 2023*

<u>Presentations</u>

[2]*Sato, K., Baldini, L. and Bracci, A.*

"Evaluation of EarthCARE Standard and Research Products for Cloud and Precipitation"

The Joint PI Meeting of JAXA Earth Observation Missions FY2022, 8 November 2022

[3]*Bracci, A., Sato, K., Baldini, L., Porcù, F. and Okamoto, H.*

"On Comparing 94 GHz Satellite Measurements with a Micro Rain Radar and Disdrometer Observations in an Antarctic Site"

11th European Conference on Radar in Meteorology and Hydrology, Locarno, 29 August-2 September 2022

[4]*Sato, K., Baldini, L., Bracci, A., Okamoto, H.*

"*Spaceborne doppler radar observation in clouds and precipitation*"

Japan Geoscience Union Meeting (JPGU), May 2022

国際化推進共同研究概要

No.3

22EA-3

タ イ ト ル： Light scattering on atmospheric ice particles for lidar applictions

研究代表者： KONOSHONKIN Alexander Vladimirovich

所内世話人： 岡本　創

研 究 概 要： 巻雲中の氷粒子の微物理特性や放射特性は、気候変動予測の不確定性の重要な要因の一つである。近年衛星搭載雲レーダやライダの巻雲の長期の全球観測データが蓄積され、また 2024 年度に打ち上げ予定の EarthCARE 衛星では、新たに 94GHz 雲レーダと波長 0.355μm の高スペクトル分解ライダの搭載が予定されており、これらの波長で氷粒子の非球形性を考慮した衛星観測量を高精度で解析することが望まれている。本研究では、この２つの観測機器の利用する波長で、８つのタイプの氷粒子形状を考慮した散乱計算を実施し、雲レーダとライダの後方散乱係数の比（χ）で定義される波長比を理論計算から求めた。ライダの波長比が粒子形状で決まるのに対し、χは、サイズに大きく依存し、形状にも依存することがわかった。同じサイズでも、形状の違いによりχの値が 1 桁程度異なることがわかった。

22EA-3 Light scattering on atmospheric ice particles for lidar applications

Alexander Konoshonkin, V.E. Zuev Institute of Atmospheric Optics SB RAS
RIAM Adviser: Hajime Okamoto, RIAM, Kyushu University

Abstract

Poor knowledge of the microphysical and radiative parameters of cirrus clouds (i.e. sizes, shapes and spatial orientation of ice crystals of the clouds and their scattering cross-sections and phase functions) is one of the main sources of uncertainties in the modern numerical models for long-term weather forecasting and the global climate change. Therefore a number of international projects and space missions were focused on such studies. Cloud radar and lidar instruments are powerful and perspective tools for these investigations. However, interpretation of the cloud radar and lidar signals reflected from cirrus clouds is a difficult problem not solved decisively yet.

Last years the RIAM team of the project demonstrated (Okamoto et al., 2019-2021) that synergy use of the cloud profiling radar (CPR) of CloudSat and space lidar CALIPSO provides more accurate retrievals of cloud properties than the single use of CPR or lidar. The products and algorithms for the analysis of cloud microphysics have been developed. Here the problem of non-spherical scatterings in CPR observables was numerically solved by means of the discrete dipole approximation (DDA) and FDTD approximations (Okamoto 2002, Ishimoto 2008).

These algorithms were generalized for application to EarthCARE mission with its CPR and lidar ATLID. The treatment of non-spherical scatterings in ATLID observables is crucial for the retrieval of cloud microphysics and we used the physical-optics approximation developed by the IAO team of the project (Borovoi, Konoshonkin et al., 2017-2021). During the joint research by IAO team and RIAM team we have modified and checked jointly the algorithms based on the synergy use of CPR, lidar ATLID, and multi-spectral radiometer of EarthCARE.

Purpose

Aim of the joint research was to modify and check jointly the algorithms for retrieval of microphysical properties of cirrus clouds based on the synergy use of CPR, lidar ATLID, and multi-spectral radiometer of EarthCARE. While these algorithms have been developed by the RIAM team earlier as far as the cloud radar signals also were calculated by the reliable numerical methods, the main obstacle was to calculate the light scattering by the ice crystals of cirrus clouds for the lidar ATLID.

Method

For the ATLID lidar (λ = 0.355 μm), the light backscattering matrices for nonspherical ice particles were calculated within the framework the physical optics method. The refractive index of ice was taken as 1.3249 + 0i. For the 94-GHz CPR radar (λ = 3189 μm), the backscattering matrices of microwave radiation were calculated within the discrete dipole approximation developed by M. Yurkin; in this case, the refractive index of ice was taken as 1.7864 + 0.0032i.

The following shapes of randomly oriented particles were modeled: hexagonal columns and plates, bullets, droxtals, aggregates, bullet-rosettes, particles of an arbitrary shape, and spherical particles. When modeling by the discrete dipole method, the particles were represented by a set from 4000 to 20000 dipoles depending on the particle size.

It is accepted to define dimensions of large nonspherical cirrus cloud particles by their maximum size (the distance between the most remote points of the particle) $D_{\max}$, but we found that the equivalent radius (R_{eq}) is more relevant property. In our calculations, it varied within the range from about 10 to 1000 μm. Thus, the typical crystal size significantly exceeds the wavelength of the lidar but is less than the wavelength of the cloud radar.

Results

We have obtained the solution of the light scattering problem for the ATLID lidar in terms of Muller matrixes and presented it as a database. As an illustration, Fig. 1a shows the S_{11} element of the Mueller matrix as a function of the equivalent radius R_{eq} of the particle.

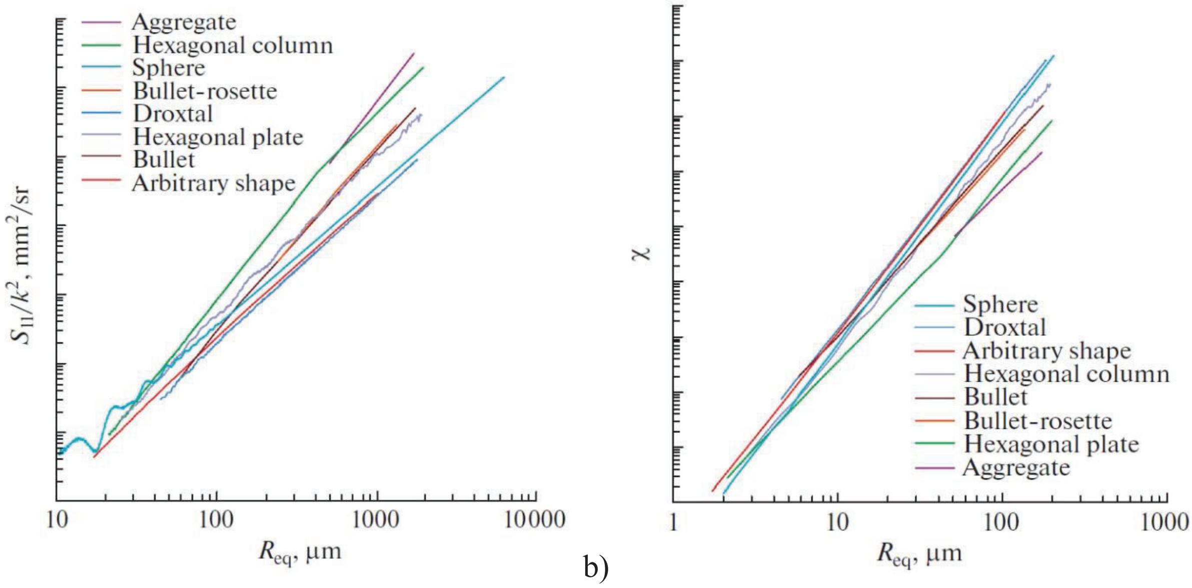

a) b)

Fig.1. The S_{11} element of the Mueller matrix (a), the ratio of the cloud radar to the lidar signal (b)

After we could solve the problem of scattering by cirrus cloud ice particles as applied to the ATLID and CPR, we could calculate the ratio of the cloud radar signal to the lidar signal. Figure 1b shows the ratio of the cloud radar signal to the lidar signal. The ratio was calculated by the equation

$$\chi = \frac{\beta^{radar}}{\beta^{lidar}} = \frac{c\sigma^{radar}}{c\sigma^{lidar}} = \frac{S_{11}^{radar}}{S_{11}^{lidar}} \qquad (1)$$

Discussion

Equation (1) involves the following assumptions: the cloud radar and the lidar observe the same ensemble of ice crystals (although the fields of view of the instruments are different) and the cloud is homogeneous both in the orientation of the crystals and in their size.

Within the scope of this work, we do not consider the question of how such assumptions are allowable; therefore, special attention should be paid to this when interpreting the experimental data. Besides, ice crystals in cirrus clouds are not monodisperse but are distributed by sizes. Since the question of choosing the law of crystal size distribution is still under discussion, we chose as a preliminary estimate the gamma distribution.

The main conclusion of the research is that it is the cloud radar–lidar ratio that is the most informative for retrieve the size of crystals after specifying their shape. The obtained results were used for modified and check jointly the algorithms based on the synergy use of CPR, lidar ATLID, and multi-spectral radiometer of EarthCARE.

Publications

1. Shishko V.A., Timofeev D.N., Konoshonkin A.V., Kustova N.V., Kan N., Tkachev I.V., Masuda K., Ishimoto H., Okamoto H., Borovoi A.G. Backscattering characteristics of optical and electromagnetic waves in joint sensing of cirrus clouds by a polarizing lidar (0.355 μm) and

a 94-Ghz radar// Atmospheric and Oceanic Optics, 2022, V. 35. No. 06. pp. 775–781. DOI: 10.1134/S1024856022060239

2. Konoshonkin A.V., Tkachev I.V., Kustova N.V., Timofeev D.N., Borovoi A.G. Updated databank of backscattering Mueller matrices of cirrus clouds' ice crystals for lidar applications // International Laser Radar Conference, June 26 – July 1, 2022. [S03_P05].

3. Konoshonkin A.V., Kustova N.V., Shishko V.A., Timofeev D.N., Tkachev I.V., Salnikov K.S. Light scattering database for interpretation of lidar sounding of cirrus clouds // Proc. SPIE 12265, Remote Sensing of Clouds and the Atmosphere XXVII, 122650D (2022). DOI: 10.1117/12.2636363

国際化推進共同研究概要

No.4

22NU-1

タイトル： Analysis of plasma fluctuations using 3-D tomographic system for applying plasma-enhanced atomic layer deposition

研究代表者： CHUNG Seung-min

所内世話人： 文 贊鎬

研究概要：

プラズマ励起ALD(PE-ALD)は、オングストロームレベルの分解能で超薄膜を合成するためのエネルギー強化方法であり、循環堆積プロセスの１つのステップでプラズマが使用されます。プラズマ種を反応物質として使用すると、従来のサーマルALD法よりも処理条件の自由度が高くなり、材料特性の範囲がより広範になります。ただし、プラズマからのイオンとラジカルのフラックスと、表面でのそれらの反応は、正確には推定されません。そこで３次元トモグラフィーシステムを用いてPE-ALDの全反応場を大域測定することが本研究の目的である。しかし、PE-ALD プロセスに適用するには時間が不十分であるため、このトモグラフィーシステムは使用されませんでした。一方、将来的に３次元トモグラフィーシステムによるPE-ALDのプラズマ挙動の検証などは、薄膜形成に関する多くの情報を与えてくれ、半導体のプラズマプロセス分野の発展に広く貢献することが期待される。

22NU-1

Analysis of plasma fluctuations using 3-D tomographic system for applying plasma-enhanced atomic layer deposition

CHUNG Seung-min
(Yonsei University, Seoul, Korea)

Atomic layer deposition (ALD) should be a promising technique for the fabrication of nanomaterials, as it enables the deposition of a thin film with good uniformity over a large area. Advantages of the ALD technique include thickness control at the atomic scale, production of highly conformal films, and low-temperature growth. The ALD process is separated into four steps. First, a precursor to being deposited on a substrate is supplied, then the composed atoms are chemisorbed with molecules. As the second step, the precursor is evacuated from the chamber, which means cleaning a by-product on the substrate using noble gas like Ar. The surface is then exposed to the second elemental species, which reacts with the first elemental monolayer to form a compound material. The final step is evacuation, like the second step. This process is repeated as many times as necessary to grow a film of the desired thickness.

Otherwise, plasma-enhanced atomic layer deposition (PE-ALD) is an energy-enhanced method for synthesizing ultra-thin films with angstrom-level resolution in which plasma is employed during one step of the cyclic deposition process. Using plasma species as reactants allows for more freedom in processing conditions and a more comprehensive range of material properties than the conventional thermally-driven ALD method. However, the fluxes of ions and radicals from plasma and their reaction on the surface do not estimate precisely. For example, when admixing two reactant gases in the plasma, new molecules could be formed through gas-phase or surface recombination reactions.

Recently, Carbon research has been actively conducted to increase the joule heating efficiency by increasing the specific resistance of the electrode. Carbon, which exhibits various resistivities depending on the state of atomic bonding, is an attractive material as a PCM (Phase Change Memory) electrode. So far, PVD (Physical Vapor Deposition) and CVD (Chemical Vapor Deposition) processes have been used to deposit thin carbon films. However, it is difficult to deposit a uniform carbon thin film on a three-dimensional structure with the conventional method and control carbon's physical properties. Consequently, the ALD is the key method to solve those problems. Furthermore, the ability could be improved if the plasma-enhanced ALD is used to deposit the carbon. Therefore, the carbon process using ALD and PE-ALD was developed in this study.

Experient Method

The PE-ALD chamber for depositing the amorphous Carbon thin film consists of a showerhead-type injector and a capacitively coupled plasma (CCP) reactor. The sample stage in the chamber's center is heated up to 600 °C. The substrate was pre-treated by O_2 plasma to remove byproducts and CBr_4 exposure to increase the Carbon growth rate. Each ALD cycle consists of four sequential steps: exposure of CBr_4 to the hydroxylated SiO_2 and W substrate, purging of residual precursor molecules by inert Ar gas (step 2), exposure to hydrogen plasma gas or H_2, NH_3 gas exposure, and purging of byproducts and residual H_2 reactant gas using inert Ar gas (step 4). The CBr_4 precursor from Sigma-Aldrich was vaporized at 60 °C, and the boding dissociation energy is 56.2 kcal/mol. The supply line must be continuously heated at a relatively high temperature of ~70 °C to maintain good

CBr_4 flux stability and avoid CBr_4 condensation. The reactants were NH_3 or H_2 for Thermal ALD, and H_2+Ar plasma was used as PE-ALD on the substrate.

Results & Discussion

Amorphous Carbon was deposited on several substrates that are SiO_2, W, and GeS_2, using H_2 or NH_3 gas for studying the chemical reaction. Figure 1 shows that an amorphous Carbon layer was formed on only the W substrate, and this figure appears the NH_3 reactant has a higher growth rate than the H_2 reactant. All reaction energy has been calculated with each enthalpy energy to explain the results. The equation is very simple: the sum of all before energy minus after energy. Finally, we could explain that the NH_3 reactant has a higher chemical reaction than the H_2 reactant with the CBr_4 precursor.

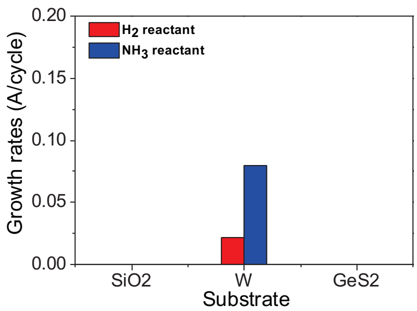

$$\Delta H = \sum BE_{bonds\ broken} - \sum BE_{bonds\ formed}$$

<CBr_4 + H_2 reaction>

$$6\,CBr_4 + 12\,H_2 \rightarrow 6\,CH_4 + 6\,Br_2$$

$\Delta H_{H_2\ reaction}$: -4,254 kJ/mol

<CBr_4 + NH_3 reaction>

$$6\,CBr_4 + 4\,NH_3 \rightarrow 6\,CH_4 + 12\,NBr$$

$\Delta H_{NH_3\ reaction}$: -6,540 kJ/mol

Figure 1. a) Carbon growth rate on several substrates. b) Reaction energy according to the reactant gas.

These two graphs show the growth rate of amorphous Carbon PE-ALD and Thermal ALD at temperatures ranging from 150 to 400 °C. The ALD window is in the temperature range of 200 to 250 °C in the case of PE-ALD. However, the ALD window of thermal ALD shows 250 to 300 °C because plasma has higher reaction energy than only thermal reaction on the effect of chemisorption. The growth rate also supports that the plasma-enhanced ALD process can deposit the Carbon film speedily. We also measured sheet resistance using 4-point prove at several temperatures. The sheet resistance at 250 °C shows that thermal ALD has a lower value than PE-ALD. It could explain the film is formed with amorphous Carbon is different types by different reactant processes.

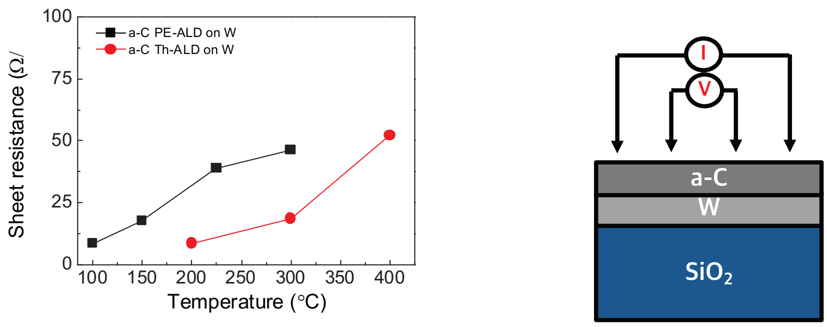

Figure 2. Sheet resistance according to the reactant types & schematic view of 4 points prove.

The 3-D tomographic system was not used in this project because time is insufficient to apply the PE-ALD process. However, we believe that the plasma behavior of certification by 3-D tomographic gives us lots of information about forming a thin film and could achieve the plasma process of semiconductors during our collaboration.

国際化推進共同研究概要

No. 5

22NU-2

タ イ ト ル： Plasma start-up and sustainment in spherical tokamak configuration by RF

研究代表者： TAKASE Yuichi

所内世話人： 出射　浩

研究概要：

令和5年2月2、3日の2日間で国際 WS をハイブリッド形式で開催した。英国から2名、米国から4名、国内から多数の参加があった。QUEST 実験の最近の進展・検討に加え、国内外実験の進展・検討、新たなシミュレーション解析などが議論された。英国から2件、米国から5件、国内で7件の研究成果発表があり、主に非誘導プラズマ電流立ち上げに関し、活発な議論があった。

Plasma start-up and sustainment in spherical tokamak configuration by RF

TAKASE Yuichi
(Tokamak Energy Ltd., United Kingdom)

An on-site and on-line hybrid workshop on “Plasma start-up and sustainment in spherical tokamak configuration by RF” was held on 2nd and 3rd February at Advance Fusion Research Center in Research Institute for Applied Mechanics, Kyushu University. Lively discussions were held following each presentation.

Agenda

2nd February

10:00 -10:10

Yuichi Takase / Kazuaki Hanada

WS purpose and agenda

10:10 - 10:30

Kazuaki Hanada

Dependence of wall saturation time on wall temperature in QUEST

10:30 - 11:10

Takumi Onchi

Report on the ECH experiment in QUEST 2022 campaign

11:10 - 11:50

Ryuya Ikezoe

Probing of fast electrons and corresponding kinetic modes on QUEST

11:50 - 13:30 **Lunch**

13:30- 14:10

Kengoh Kuroda

Development of transient CHI startup using a new electrode configuration on QUEST

14:10 - 14:50

Shin Kubo

Study on the electron Bernstein wave detection using HCN laser scattering on QUEST

14:50 - 15:30

Hitoshi Tanaka

Present Status of LATE Experiment (Remote)

15:30 – 15:50 **Coffee Break**

15:50 - 16:20

Atsushi Fukuyama

Modeling of O-X-B mode conversion on QUEST

16:20 - 17:00

Yuichi Takase

Achievements and Future Plans at Tokamak Energy

17:00 - 17:40

A. Köhn-Seemann

Simulation of the O-X mode conversion in MAST Upgrade (Remote)

17:40 – **Group Photo**

3rd February

10:00 - 10:40

Naoto Tsuji

Studies of RF start-up on the TST-2 spherical tokamak

10:40 - 11:20

Masayuki Ono

X-I mode for efficient solenoid-free ECCD plasma current start-up and ramp-up for fusion reactor

11:20 - 12:00

Luis F. Delgado-Aparicio

Off-axis seed and growth of runaway electrons in MST tokamak plasmas

12:00 - 13:00 **Lunch**

13:00 - 13:40

Luis F. Delgado-Aparicio

X-ray imaging crystal spectrometer US-Japan collaboration for JT60SA

13:40 - 14:20

Syunichi Shiraiwa

Integration of RF sheath BC to a large electro-magnetic wave simulation

14:20 - 15:00

Nicola Bertelli

ICRH simulations of ITER antenna and a comparison with different RF solvers

15:00 - 15:10 **Coffee Break**

15:10 - 16:00

Discussion on future plan in AFRC (QUEST)

All suggested focus and output for this joint drafting session

16:00 -

Drafting of proposals for experiments, diagnosis, and analysis

17:00 -

Summary

Presentation Summary

Kazuaki Hanada

Introduction of Japanese stratagem for ST reactor development and the present standpoint of QUEST were explained. Steady State operation of high-performance plasma is still one of the most important subjects on the stratagem in the view of worldwide data base for long pulse operation of high-performance plasma. The QUEST project has successfully achieved 6 h discharge that is the world record of pulse duration for tokamak-type plasma and is staying at the turning point to go up the performance. To obtain high-performance plasma, it is well known that lowering fuel particle recycling is a key. QUEST has been equipped with capability for wall temperature regulation since 2015. Consequently, 6h discharges could be achieved at the wall temperature, T_W<473K under the cooling down condition of center-stack cover panels (CSPs) made of SS-316L. It can be explained by storing hydrogen into the SS-316L material at low temperature T_W<423K. The time for reaching wall saturation, τ_{WS} has been investigated, collecting longer than 30 min. Higher T_W reduces τ_{WS}, but T_W control can assist to make fuel recycling lower than unity and the pulse duration extended up to more than 3 h from 40 min even T_W ~ 623K that is relevant to future fusion reactors.

Takumi Onchi

- For the QUEST spherical tokamak experiment, Medium scale maintenance of 28 GHz-GYT system was completed in 2022.
- Avoiding RF power absorption into energetic electrons, bulk electrons tend to increase temperature.
- Electron temperature exceeds 1 keV in the small Tokamak-like configuration with retarding electric field.
- ECH + OH realized the density higher than the cut-off density for 8. 56 GHz

Ryuya Ikezoe

Energetic Particle Probe (EPP) was completed, and various information about fast electrons, which had not been observed before, became available. The first experiment showed that it can be used in the following three ways;

1. Fast hard X-ray monitor (Hard X-rays from entire plasma regions)
   Compared to the existing CdTe detectors, the number of counts is very large and fast

phenomena can be measured, leading to the world's first observation of high-frequency fluctuations of fast electrons. Experimental evidence for the interaction of fast electrons and high frequencies modes.

2. Local hard X-ray measurement
   At R <1.3 m, braking X-rays from fast electrons colliding with the probe head are massively measured, which can give the spatial distribution of fast electron flux in SOL. Unlike general lost-particle detectors mounted on the wall, it can measure particles that are not in loss trajectories.
3. Local pitch angle & energy (E, θ) spectrum measurement
   Ultimately, electron velocity distribution is evaluated.

Kengoh Kuroda

Transient CHI current start-up by using newly designed simple electrode has been examined in QUEST.

- The result of LFS and HFS CHI on the initial test system suggested that the HFS CHI was suitable in QUEST configuration.
- In the remodeled HFS CHI system, sufficient injector flux can be formed in the injector region by PF5-1 coil close to the region, the breakdown mainly occurs in the injector region by the NSTX type gas manifold, the space between the electrode and outer vessel wall prevents the absorber arc, and the profile of the injector current is estimated by a number of magnetic sensors of Bt' on the vessel wall.
- In the initial test on the remodeled system, higher toroidal current was repeatedly achieved under higher injector flux condition. However, flux sufficiently expanded only under high vertical field (high PF26 coil current) condition because as the PF26 coil current decreased, the injector current flowing out to the absorber region increased, in which the formation of the closed flux surfaces was not achieved.

In Dec. 2022 CHI exp, we tried to improve the CHI discharge, in which the ceramic cover was installed on outer parts of the electrode to prevent the injector current from flowing out to absorber region, the capacitor bank power supply was modified to apply higher voltage with shorter pulse, and each PF5-1 and PF5-2 coils was individually controlled for forming the injector flux.

- By applying higher voltage (-1925V) with less amount of injected gas (5.5torr*L), the flux evolved largely under the condition of lower PF26 coil current (0.85kA).
- In fast camera images, the formation of the closed flux surfaces was observed, in which the closed flux surfaces shrunk at the center with the decay of the toroidal current, and very high multiplication (100-200) of the toroidal current suggested that the current was no longer the current driven by the injector current, but the confined current in the closed flux surfaces.
- On the discharge of CHI+OH, the confined current persisted with the closed flux surfaces for longer time. If lower density CHI plasma is able to be started-up, the current is expected to be ramped-up by OH.

Shin Kubo

The main purpose of this project is a direct detection of the excited electron Bernstein wave (EBW) near the core region of QUEST. Documentation of the behavior of EBW is important for optimizing EBW heating/current drive. Original plan was to use sub-THz gyrotron (400 GHz) on loan from Fukui Univ. Due to the expiration of the loan term, and moreover, higher frequency has an advantage in detecting higher wavenumber, we have decided to utilize HCN laser (890 GHz) as a scattering source. The original design of the scattering geometry is based on the quasi-optical grating plate on the center post of the QUEST. This configuration is scalable to the 890 GHz. The detection system is to apply sub-harmonic (× 1/2) mixer and harmonic (×10) generator prepared for 400 GHz. Present plan is to extend this sub-harmonic mixer to use as 1/5 and configure narrow band highly sensitive radiometer to cover f0=890 GHz range. Relying on the stability and sharp frequency spectra of the HCN laser as well as that of EBW $f_H = 8.5$ GHz, by modulating the local frequency between $f_0/50$ and $(f_0 \pm f_H)/50$.

Hitoshi Tanaka

- The LATE device was disassembled in 2021 for repair work of the experiment building. Now Re-assembling of the LATE device has completed and preparation for starting the discharge is in progress.
- Background magnetic field around the setting position of LATE was measured and found that there is about 10 times the Earth's magnetic field coming around from the sole plate of WT-3. Correction coils are designed.
- Soft X-ray CT system is developing to investigate the intermittent plasma ejection phenomena. During the plasma ejection phase, there appear a strong emission from the center post at z = 10 ~ 20 cm, near the cross point of LCFS with the center post. It may be emitted from the high energy electrons lost along the LCFS. A Mo rod limiter was set behind the center post out of the sight of the CT cameras.

Atsushi Fukuyama

- Kinetic full wave analysis using the integral form of dielectric tensor was applied to the analysis of the O-X-B mode conversion of electron cyclotron waves in QUEST.
- Some of the power of EBW is absorbed near the ECR, but small amount of collision leads to significant collisional absorption of EBW.
- Two-dimensional analysis on mid plane in tokamak configura- tion (slab model) has shown the spatial structure of O-mode, X-mode, and electron Bernstein wave. It was confirmed that O-mode is efficiently converted to EBW near the optimum injec- tion angle.

Remaining issues

- Better formulation of absorbed power density
- Mid-plane analysis in toroidal configuration
- Poloidal cross section analysis including nonuniform B along B

Yuichi Takase

- ST40, a compact high field ST with copper coils at Tokamak Energy (typical parameters of R_0 = 0.4-0.5 m, A = 1.6-1.8, B_t = 1.5-2.2 T, and I_p = 0.4-0.8 MA) has achieved fusion-relevant ion temperatures of greater than 100 million degrees K (8.6 keV). Plasmas with I_p = 0.3-0.4 MA are formed quickly by merging-compression, followed by a slower ramp up to higher I_p using the solenoid. T_i was increased gradually from < 1 keV in June 2021 to nearly 10 keV in February 2022 through various optimisations, including boronisation and between-shot He GDC which enabled operation in the hot-ion mode, discharge optimization (avoidance of sawteeth, detachment from the inboard wall, optimization of NBI timing, etc.), improvement of NBI performance, operation with D NBI into D plasma, and increase of B_t. A 55 kV NBI (which preferentially heats electrons) was injected from the beginning of discharge, and a 24 kV NBI (which preferentially heats ions) was injected later in the discharge. T_i and T_e were measured using the X-ray crystal spectrometer viewing the He-like Ar line emission. The profiles of density and temperature were inferred by integrated modelling, and the central T_i was confirmed by an independent measurement using the charge exchange recombination spectroscopy. TRANSP analysis indicated that the deuterium temperature is only slightly lower than the measured Ar and C temperatures.

- ST80-HTS, a higher field device using high-temperature superconducting ciols (with nominal parameters $R_0 \sim 0.8$ m, $A \sim 2$, $B_t \sim 4\text{-}5$ T) is being designed. This device will demonstrate successful integration of critical engineering technology building blocks, and demonstrate long pulse operation with high duty cycle, at high plasma performance using D fuel.

A. Köhn-Seemann

The spherical tokamak MAST Upgrade is, among other things, considered as a validation or test- bed for non-inductive current drive methods to be used in STEP, the Spherical Tokamak for Energy Production, which aims on demonstrating net electricity production in the 2040s. MAST Upgrade will be equipped with two dual-frequency gyrotrons, operating at 28 and 34.8 GHz, with a power output in total of 1.8 MW. This microwave heating system will be used to study the current drive capabilities of the EBW at the MW power range. In this project, we performed a full-wave analysis of the coupling to the EBW, where 5 different codes have been used. Scenarios with high conversion efficiencies slightly above 90 % were identified. The deteriorating effect of plasma density fluctuations, based on MAST parameters, was investigated: it was found that only a small reduction of the conversion efficiency on the order of 5 % is expected. MAST Upgrade is thus ideally suited to study and explore heating and current drive by EBWs.

Naoto Tsujii

Non-inductive start-up using lower-hybrid (LH) waves has been studied on the TST-2 spherical tokamak. Plasma current start-up up to 26 kA has been achieved using the top launch antenna which is about a quarter of a typical Ohmically driven discharge. The top launch scenario showed strong thick-target x-ray radiation that indicated substantial LH wave driven fast electron losses that may be limiting the achievable plasma current. To overcome this limitation, the outer-off-midplane launch antenna was newly developed and installed in TST-2. Stronger core absorption and smaller fast electron losses are expected for the new scenario.

Masayuki Ono

The elimination of OH solenoid maybe the most impactful design driver for an economical compact fusion tokamak reactor system. To address this challenge, an efficient solenoid-free start-up and ramp-up scenario utilizing the X-mode at $\omega = \Omega_e$ (X-

I) was investigated to drive ~ 10 MA of plasma current for a compact Sustained High Power Density tokamak facility with a modest ECH power of ~ 10 MW utilizing the 170 GHz gyrotrons. The high ECCD efficiency is due to the strong wave-particle interactions at the Doppler broadened $\omega = \Omega_e$ resonance, together with the accessibility constrained absorption on uni-directional passing electrons. The efficiency of the well localized current drive remains high for a broad range of launched parallel index of refraction suggesting that a relatively simple waveguide launcher placed outboard could be used. As a next step, a time dependent model of the X-I solenoid-free start-up and ramp-up has been developed. Interestingly, the X-I current ramp-up process appears to possess a positive feed-back of key parameters, ECCD, I_p, L-mode confinement time, and Te, where increase in any one of the parameters results in corresponding increases in other parameters resulting in a virtuous cycle of continuous current ramp-up even with a constant applied power. A typical ramp-up time is 200-300 sec. If shorter ramp-up time is desired, it would be prudent to have some T_{e0} control tools such as impurity injection to increase the plasma resistivity and radiation with sufficient ECH power to overdrive ECCD well above 10 MA during the ramp-up. Because SHPD is a high field device, the plasma normalized beta stays well below 1 so the discharge is expected to be MHD stable. As long as T_{e0} stays below 25 keV, the synchrotron radiation is also negligible < 1 MW. The present NI X-I ECH start-up and ramp-up can be tested in any tokamaks/STs with sufficient toroidal magnetic field strength to have the fundamental electron cyclotron resonance within the plasma.

Luis F. Delgado-Aparicio

1) The formation of an off-axis RE population with a linear growth has been resolved for photon energies $\sim(20\text{-}200)\times T_{e0}$
2) Emergence of the seed population in the periphery instead of the core is consistent qualitatively and quantitatively with a lower n_e and E_D as well as hollow $E_\parallel/E_D$ ratios and streaming parameters, all in agreement with theory and numerical simulations.
3) Exponential growths have been spatially resolved for the first time and are consistent with enhanced diffusivity, convective transport of $\gtrsim V_{\mathrm{WARE}}$ and $E\sim10^3\times T_{e0}$.
4) Calculations with BMC successfully resolved the space- and time- dependent dynamic scenarios including RMP suppression @ the edge with large $E_\parallel/E_D$.
5) More experiments @ MST and simulations with BMC and KORC
6) Development of RT diagnostic techniques with Si and CdTe sensors

Shinichi Shiraiwa

The radio-frequency (RF)-induced sheath is the rectification of an RF electric field in a sheath layer, which is formed between a plasma and plasma facing components (PFCs). The resultant DC potential accelerates ions to the PFSs, which potentially causes an impurity in-flux during the ICRF operation. A new formulation to describe the RF sheath physics is proposed, in order to incorporate it into a global 3D full wave simulation. This new formulation is characterized by the non-linear iteration scheme that connects physics variables in a unique order. The new formulation was extensively verified using the various 2D simulations in the literature. The model is applied to the WEST ICRF antenna side limiters, predicting the sheath voltage in 100-200V using a realistic density profile in front of the antenna. Future direction includes acceleration of non-linear sheath calculation using AI/ML was also discussed.

Nicola Bertelli

The ion cyclotron resonance hearing (ICRH) system in ITER consists of two identical ICRH antennas to deliver 20 MW to the plasma (baseline, upgradable to 40 MW). ICRH will play a crucial role in the ignition and sustainment of burning plasmas in ITER and a high-fidelity modeling is a very important aspect as well. Better understanding the interaction of the IC waves with the scrape-off layer (SOL) plasma is required for the ICRH ITER antenna operation. In this work, we present a series of Petra-M [1,2] simulations for ITER ICRH antenna model. Petra-M code is an electromagnetic simulation tool for modeling RF wave propagation based on MFEM [http://mfem.org]. Numerical results for different absorption profiles are presented and discussed together with a comparison of the wave field propagation obtained both for FEM order 2 and order 3. Furthermore, a benchmark between the well tested antenna codes TOPICA [3,4], RAPLICASOL [5,6], which is based on COMSOL [www.comsol.com], and the Petra-M code is also presented. Excellent agreement is found among codes comparing S- and Z-matrices, wave electric field in front of the antenna and the coupled power. Finally, initial Petra-M simulations for the second ITER ICRH antenna model with 8 ports are also presented. Results presented in this work will be published in the AIP Conference proceeding in 2023 [7].

References

[1] 5. S. Shiraiwa and et al, EPJ Web of Conference 157, 03048 (2017).

[2]. S. Shiraiwa and et al, “Towards integrated RF actuator modeling: whole device scale RF fullwave simulation including hot core and 3D sol/antenna regions, [TH/7/2],” aper presented at the 28th IAEA Int. Conf. on Fusion Energy (Virtual Event) (2021).

[3] D. Lancellotti and et al, Nucl. Fusion 46, S476 (2006).

[4] D. Milanesio and et al, Nucl. Fusion 49, 115019 (2009).

[5] J. Jacquot and et al, AIP Conference Proceedings 1689, 050008 (2015).

[6] W. Tierens and et al, Nucl. Fusion 59, 046001 (2019).

[7] N. Bertelli et al, Accepted for publication in AIP Conf. Proc. (2023).

国際化推進共同研究概要

No. 6

22NU-3

タ イ ト ル： Numerical simulation of EC and EBW in QUEST

研究代表者： BERTELLI Nicola

所内世話人： 出射　浩

研究概要：
電子バーンシュタイン波を用いれば、遮断密度を超えた高密度プラズマで加熱・電流駆動が可能となるが、静電波であるため電磁波からのモード変換が必要である。低磁場側入射の場合、遮断密度領域で電磁波の正常波モードから異常波モードへ、さらには高域混成波共鳴領域で静電波の電子バーンシュタイン波へのモード変換が必要である。正常波モードから異常波モードへのモード変換には、最適な磁場に平行屈折率での入射が必要であるが、最適条件から外れた場合でも、遮断域長が波長に比べて短ければ、トンネル効果でモード変換される。波動伝搬を扱う光線追跡法では、トンネル効果でモード変換した場合の波動伝搬が追えない。遮断域の透過率を解析式で与え、遮断域よりさらに高密度側の波動伝搬域を探査し、電子バーンシュタイン波へのモード変換、電子サイクロトロン共鳴吸収を解析した。また、Petra-M による有限要素シミュレーションも実施され、国際ワークショップにて報告された。

Numerical simulation of EC and EBW in QUEST

BERTELLI Nicola
(Princeton University, U.S.A)

Electron Bernstein wave heating and current drive (EBWHCD) scenario in the low-field side injection is considered for non-inductive radio-frequency plasma ramp-up in the QUEST. In this scenario, the incident O-mode wave with a specific optimized refractive index parallel to the magnetic field $N_{//,\mathrm{opt}}$ can convert to the slow X-mode wave at the cut-off layers. The P-cutoff (at $\omega = \omega_{\mathrm{pe}}$) for the O-mode wave coincides to the L-cutoff (at $N_{//,\mathrm{opt}}{}^2 = L$) for the slow X-mode wave, where ω and ω_{pe} are wave and plasma frequencies. Here the parameter L is a Stix's notation describing with ω, ω_{pe} and the electron cyclotron frequency ω_{ce}. Figure 1 shows dependencies of squared refractive index perpendicular to the magnetic field $N_\perp{}^2$ on $\omega_{\mathrm{pe}}{}^2/\omega^2$ for propagations with $N_{//,\mathrm{opt}}$ and $N_{//,\mathrm{opt}+/-0.1}$. The O-mode wave with $N_{//,\mathrm{opt}}$ can propagate to the high-density (over-dense) side after the mode conversion to the X-mode wave at the coincided cutoff layer. There are evanescent layers with $N_\perp{}^2 < 0$ for the O-mode waves without $N_{//,\mathrm{opt}}$ as the two cutoff layers do not coincide. Figure 2 (a) shows ray trajectories, which are analyzed by the TASK/WR code, of the O-mode wave with $N_{//,\mathrm{opt}}$ and $N_{//,\mathrm{opt}+/-0.1}$. In the ray tracing approach, the incident O-mode waves without $N_{//,\mathrm{opt}}$ are reflected to the outside at the cutoff layers. The O-mode wave without $N_{//,\mathrm{opt}}$ should also propagate to the over-dense side through the tunneling, if the evanescent layer thickness is not larger than the wavelength well. Figure 2(b) shows the ray trajectories of the O-mode wave with $N_{//,\mathrm{opt}}$ and $N_{//,\mathrm{opt}+/-0.1}$ when taking the tunneling into consideration. The restart positions after the tunneling (at

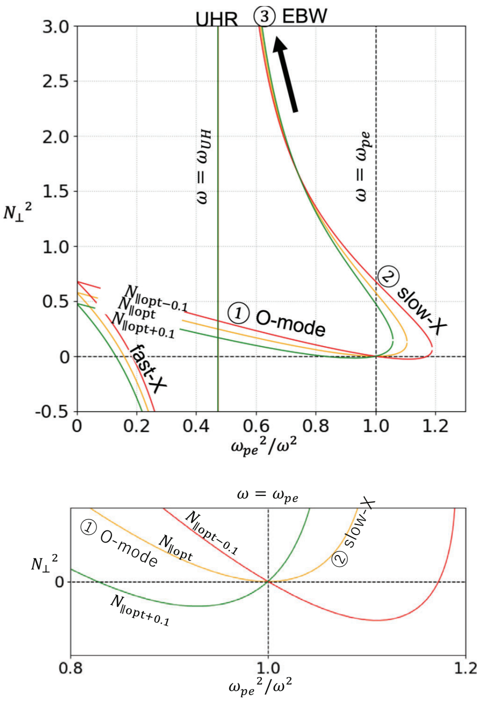

Fig.1. Dependencies of squared refractive index perpendicular to the magnetic field $N_\perp{}^2$ on $\omega_{\mathrm{pe}}{}^2/\omega^2$ for propagations with $N_{//,\mathrm{opt}}$ and $N_{//,\mathrm{opt}+/-0.1}$.

$N_{\perp}{}^{2}$=0) beyond the evanescent layer are searched along the density-gradient directions from the cutoff positions. The transmitted efficiencies at the tunneling are evaluated from an analytical formula [1]. The converted X-mode waves propagate to the low-density side and convert to the electrostatic Bernstein wave (EBW) again at the upper hybrid resonance (UHR) layer. Since the X-mode wavelength becomes short at the UHR layer, the X-mode can convert to the short-wavelength electrostatic EBW. Figure 3 shows the normalized ray powers along the propagations with $N_{//,\mathrm{opt}}$ and $N_{//,\mathrm{opt}+/-0.1}$. The transmitted ray powers are dropped at the tunneling for the propagations with $N_{//,\mathrm{opt}+/-0.1}$, depending on the incident refractive indexes at the cutoff layers. The converted EBWs are absorbed in the up-shift electron cyclotron resonance area. In the figures, the EBW rays are traced until the ray powers become 0.1% for the incident powers. Further investigations are will be conducted to evaluate deposition and driven-current profiles in the EBWHCD scenario by using multiple rays.

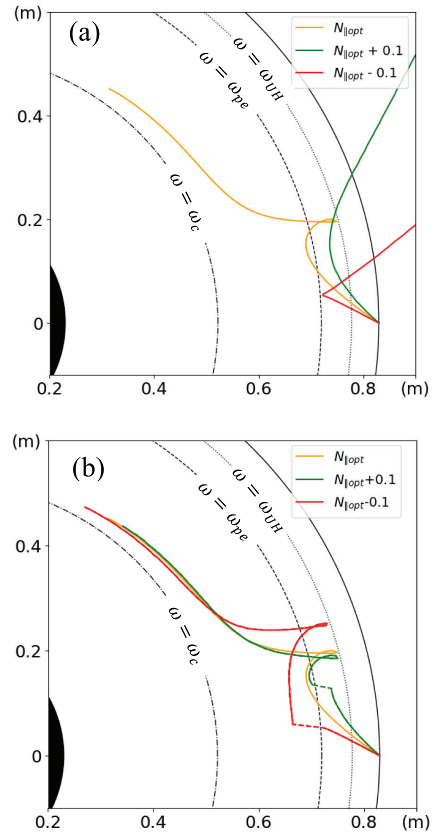

Fig.2. Ray trajectories of the O-mode wave with $N_{//,\mathrm{opt}}$ and $N_{//,\mathrm{opt}+/-0.1}$ (a): with and (b): tunneling.

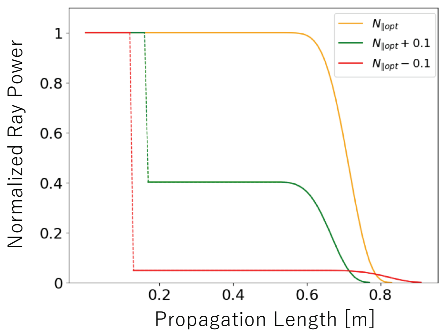

Fig.3. Normalized ray powers along the propagations with $N_{//,\mathrm{opt}}$ and $N_{//,\mathrm{opt}+/-0.1}$.

Full 3D NSTX-U device geometry including realistic antenna geometry and 3D scrape-off-layer (SOL) plasma is also modeled to simulate NSTX-Upgrade plasmas using Petra-M finite-element-method (FEM) [2]. Petra-M code is a state-of-the-art generic electromagnetic simulation tool for modelling radio-frequency wave propagation based on MFEM [https://mfem.org], open-source scalable C++ finite element method library. This subject was presented at a workshop entitled “Plasma start-up and sustainment in spherical tokamak configuration by RF” which was held under a different international RIAM collaboration framework.

[1] E. Mjölhus, J. Plasma Phys. **31**, 7 (1984).
[2] N. Bertelli, S. Shiraiwa, and M. Ono, Nucl. Fusion **62**, 126046 (2022).

国際化推進共同研究概要

No. 8

22NU-5

タ イ ト ル： Design of Electron Cyclotron Emission Diagnostic for Electron Temperature and its Fluctuation Measurements

研究代表者： SUNG Choongki

所内世話人： 文 贊鎬

研究概要：

将来的に PLATO トカマクに ECE（Electron Cyclotron Emission）測定法を確立するため、EKAIMIR（MIRROR Device at KAIST, Korea）において 2.45GHz の O モード波を入射し、EBW 加熱実験を行った。波動入射によるプラズマの蓄積エネルギーの有意な変化は観測されなかったが、光線追跡シミュレーションの結果、背景磁場に対して垂直な方向に波動を発射した場合、O モードから X モードへの変換比が低いことが原因であることがわかった。したがって実験条件に最適な打ち出し角度を見出した。また、打ち出した波の入力電力が最も多くプラズマに吸収されるのは、打ち出し角度が最適値のときであることを確認しました。この結果は、電子温度計測のための O モード EBW 検出には、斜め方向からの検出が必要であることを示しています。今後、シミュレーション結果の検証を行う予定です。

Design of Electron Cyclotron Emission Diagnostic for Electron Temperature and its Fluctuation Measurements

Mingi Choe, Dongguen Oh, Pocholo Nebres, Choongki Sung

Fusion and Plasma Dynamics Laboratory, KAIST, Daejeon, Republic of Korea

Radiation emitted by electron's cyclotron motion when magnetic field is applied, so-called electron cyclotron radiation, has been utilized as a diagnostic tool for electron temperature and its fluctuations in toroidally confined magnetic fusion system[1]. The diagnostic measuring the intensity of electron cyclotron radiation is called an electron cyclotron emission (ECE) diagnostic. To develop an ECE diagnostic, two requirements should be satisfied. First, plasma should be optically thick for the electron cyclotron radiation measured by an ECE diagnostic. To satisfy this requirement, most measurements were performed by measuring fundamental ordinary mode (O-mode) measurements or second harmonic extraordinary mode (X-mode). Here, O-mode refers to the wave propagating on the perpendicular to background magnetic field and polarized parallel to the background magnetic field, and X-mode refers to the wave propagating perpendicularly to the background magnetic field like O-mode while its polarization direction is also perpendicular to the background magnetic field. The other condition is an accessibility. The radiation emitted from the plasma should propagate well to the detector position, located outside of the plasma. Each wave mode has its own cutoff and resonance layers, and it limits an experimental condition that an ECE diagnostic is applicable.

In the collaborative research activity with RIAM last year, it was found that the expected plasma parameters in the PLATO Tokamak[2] were not suitable for ECE measurements. PLATO Tokamak will have an over-dense plasma, which has too high density to access optically thick electron cyclotron radiation modes such as fundamental O-mode and second harmonic X-mode. Instead of electromagnetic wave, electron Bernstein wave (EBW) has been studied for electron temperature measurements for over-dense plasmas like PLATO Tokamak[3]. EBW is an electrostatic wave generated through the mode conversion from slow X-mode wave at the upper hybrid resonance layer[4]. Since EBW does not have a density cutoff[5], EBW is accessible even in over-dense plasmas. A diagnostic measuring the intensity of EBW is an electron Bernstein Emission (EBE) diagnostic. The wave measured by an EBE diagnostic will not be an EBW since EBW will be damped quickly through Landau damping outside of the plasma. We will measure the electromagnetic wave converted from EBW like B-X-O mode conversion[6]. Here, we can measure either O-mode or X-mode wave. As mentioned earlier, X-mode wave can be converted from EBW at the upper hybrid resonance layer. O-mode detection is also possible for EBW measurements since X-mode converted from EBW can be converted to O-mode at the O-mode cutoff layer. Here, we need to consider the conversion efficiency of EBW to either O-mode or X-mode for reliable EBE measurements. In other words, we first need to study EBW physics including conversion efficiency of EBW depending on the experimental condition. As a first step for EBE diagnostic design study for PLATO Tokamak, we first initiate EBW physics study based on the magnetic mirror device at KAIST (KAIST MIRROR, KAIMIR). Here, we installed magnetron system for EBW heating. It is noteworthy that EBW heating is the inverse process of EBE measurements. Thus, we can study EBW physics through EBW heating experiments and the knowledge obtained from this experiment will be applicable for EBE measurements.

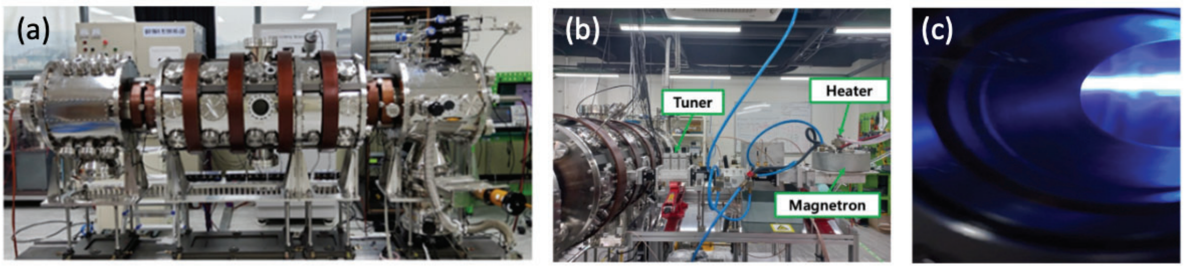

Figure 1 (a) KAIMIR device (b) Magnetron system installed at KAIMIR (c) Example of Plasma at KAIMIR

In KAIMIR, plasma having $10^{18\text{-}20}\,\mathrm{m}^{-3}$ level of electron density is generated and sustained during approximately 40ms by plasma gun system. We installed 10kW 2.45GHz magnetron system for EBW experiments in KAIMIR. Since O-mode cutoff density corresponding to 2.45GHz is $\sim 6\times10^{17}\,\mathrm{m}^{-3}$, 2.45 GHz wave is suitable for EBW experiments in KAIMIR. Considering the expected electron density of PLATO Tokamak is $10^{19}m^{-3}$ [2], we also note that KAIMIR experiments will be relevant to the PLATO Tokamak experiments. In initial experiments, we applied 2.45GHz O-mode wave while varying the voltage applied to plasma gun and the timing of wave launching to generate various density conditions for EBW study. Afterwards, we observed the changes in diamagnetic flux generated by plasma, which is proportional to the stored energy in the plasma, measured by the diamagnetic loop. In this initial experiment, we did not observe any meaningful changes by wave injection. Diamagnetic flux level in the case with wave injection was stayed at the same level within the uncertainty of the measurements in the case without wave injection.

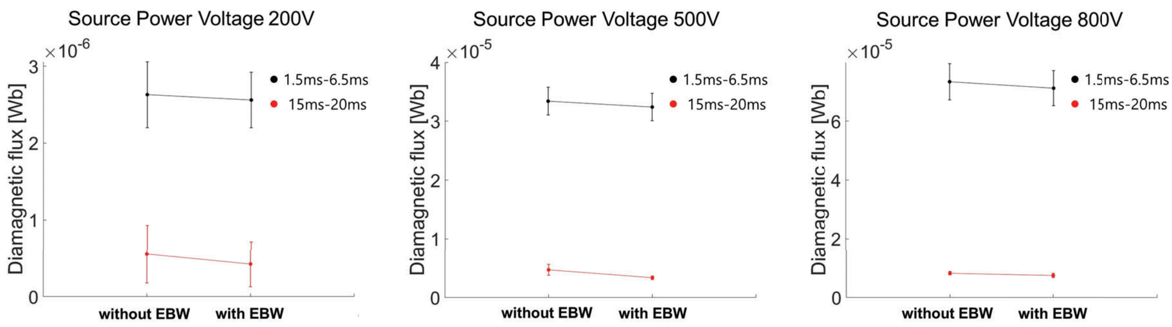

Figure 2 Diamagnetic flux measurements depending on the wave injection in various source power voltage levels and wave injection timings. Here 0ms is the time when the plasma is generated.

Ray tracing simulation code, Genray-C[7], was utilized to understand the experimental results. Figure 3 shows the simulation results for the case when source power voltage is 200V and the wave is launched during 1.5-6.5ms after plasma is generated. It is shown that the launched wave is not absorbed in the plasma. Instead, the wave is reflected at the boundary of the plasma where O-mode cutoff layer is formed. This result indicated that the launched O-mode wave was not converted to X-mode at the cutoff layer.

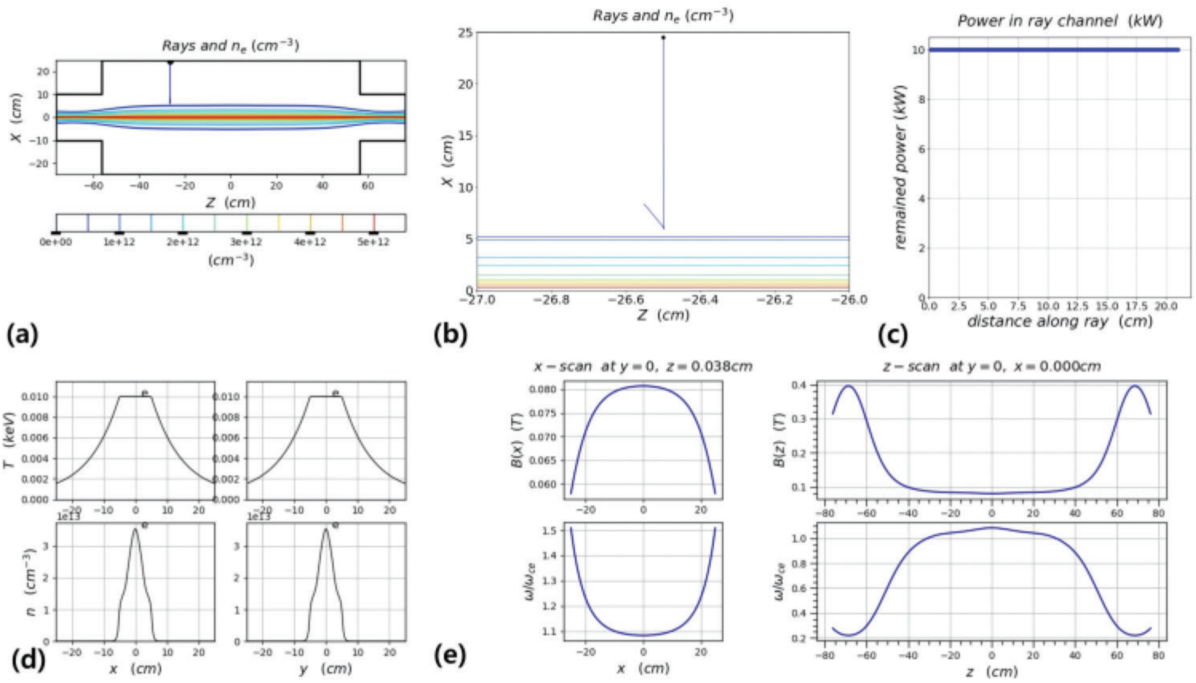

Figure 3 Genray-C simulation results when the wave is launched during 1-5-6.5ms with 200V source power voltage (a) O-mode wave path with electron density contour (b) O-mode wave path near the cutoff layer (c) the remained power of O-mode along the path (d) electron density and temperature profiles (e) magnetic field profiles used in this simulation

It is known that the ratio of the conversion from O-mode to X-mode is affected a function of the refractive indexes of parallel and perpendicular to background magnetic field, i.e., the wave launching angle[8]. We found that the optimum launching angle is approximated 40° when 0° refers to the case of launching perpendicular to the background magnetic field. In the initial experiments, only 0° launching was available. As shown in Fig. 4(a), the conversion to X-mode is almost zero in the 0° launching case, consistent with the experimental results. It is also shown that the launched wave is absorbed well when the launching angle is 40° in Figs. 4(b) and (c). In the future, we will vary the launching angle to check the consistency of the simulation results with the experiment. For EBE measurements in PLATO Tokamak, these results indicate that oblique angle measurements will be required for the O-mode detection.

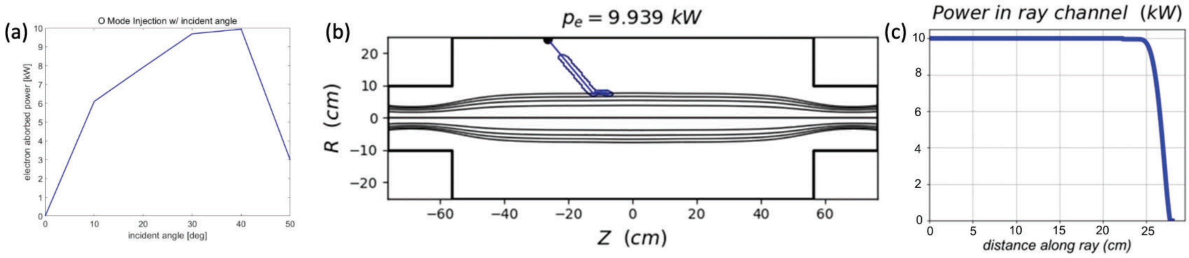

Figure 4 (a) Absorbed power by electrons with the wave launching angle predicted by Genray-C code in the case showing in Fig. 3 (b) O-mode wave path with the density contour (c) the remained power of O-mode along the path for the 40° launching case

In summary, the EBW heating experiments were performed by injecting 2.45GHz O-mode wave in KAIMIR. We did not observe any meaningful changes in the stored energy of the plasma by the wave injection, but the ray tracing simulation results showed that it was due to the low conversion ratio from O-mode to X-mode when the wave was launched perpendicular to the background magnetic field. The optimum launching angle for the experimental condition was found. We also verified that the most input power of the launched wave was absorbed in the plasma when the launching angle was at the optimal value. This result indicates that oblique angle detection is required for O-mode EBW detection for electron temperature measurements. The simulation results will be validated in the future.

REFERENCES

[1] Hutchinson, I. (2002). Principles of Plasma Diagnostics (2nd ed.). Cambridge: Cambridge University Press.

[2] Mochinaga, Shota, et al. "Transport Simulation of PLATO Tokamak Plasma Using Integrated Code TASK." Plasma and Fusion Research (2021): 1403093-1 to 6.

[3] P. C. Efthimion, J. C. Hosea, R. Kaita, et. al., “New electron cyclotron emission diagnostic for measurement of temperature based upon the electron Bernstein wave”, Review of Scientific Instruments70, 1018 (1999).

[4] M. Ali Asgarian, A. Parvazian,m M. Abbasi, et al., “Direct X-B mode conversion for high-beta national spherical torus experiment in nonlinear regime”, Phys. Plasmas 21, 092516 (2014)

[5] Heinrich Peter Laqua 2007, “Electron Bernstein wave heating and diagnostic”, Plasma Phys. Control. Fusion 49 R1 (2007)

[6] H. P. Laqua, H. J. Hartfub, and W7-AS Team, “Electron Bernstein Wave Emission from an Overdense Plasma at the W7-AS Stellartor”, Phys. Rev. Lett. 81, 2060 (1998).

[7] A. P. Smirnov, R. W. Harvey, and K. Kupfer, “A general ray tracing cod GENRAY”, Bull Amer. Phys. Soc. Vol 39, No. 7, 1626 Abstract 4R11 (1944).

[8] F. R. Hansen, et al., “The O-X-B mode conversion scheme of ECRH of a high-density Tokamak plasma” , Plasma Phys. Control. Fusion 27 1077 (1985).

国際化推進共同研究概要

No. 9

22NU-6

タイトル： Distinguish small-scale and large- scale intermittency in magnetized plasma

研究代表者： KNAUER Stefan

所内世話人： 文 贊鎬

研究概要：

私たちは乱流プラズマにおける間欠性を評価するための新しい革新的な方法を探りました。今回の PANAT プラズマの密度は低く、プロファイルは急峻ではありませんでしたが、私たちの予備的な結果は最も有望であり、今後の解析のための貴重な情報です。歪度と尖度を用いてデータの非対称性と尖鋭性を測定したところ、I_{sat} は 90mT でジャンプを示し、間欠性に関する我々の期待に応えた。特に注目すべきは構造関数解析で、I_{sat} と V_{fl} がともに間欠性を示し、I_{sat} は V_{fl} よりも間欠性が高いことが分かりました。さらに、van Milligan が提唱した間欠性パラメータでは、C(1) が予想以上に高く、I_{sat} は 90mT で間欠性挙動が低下していることがわかった。測定時に汚染があり、それが結果に反映されているが、密度勾配の長さスケールをより強く変化させれば、素晴らしい結果が得られると確信している。全体として、構造関数解析は我々の期待に最も近く、評価するための制御可能なステップを特徴とし、孤立波に対する反応が最も顕著であるように見えた。

Distinguish small-scale and large-scale intermittency in magnetized plasma turbulence

KNAUER, stefan; University of Greifswald, Physics department; Researcher

Abstract

Based on five (i to v) intermittency qualifiers typical intermittent scenarios of PANTA will be discussed. These five qualifiers are (i) the skewness, (ii) the kurtosis, (iii) the structure function analysis, (iv) intermittence parameter C(1) proposed by B. Carreras and (v) the ratio of pulse duration and averaged waiting time. Qualifiers (i) and (ii) are usually used in fusion science. Qualifier (iii) is a tool borrowed from the field of neutral fluids and gives inside on the self-similarity. It has been already used in PANTA, qualifiers (iv) and (v) are not utilized in linear plasmas yet. Qualifier (iv) allows also to study self-similarity of the turbulence. It ranges from 0 to 1. Qualifier (v) describes the burstiness. Ideally, small-scale and large-scale intermittency can be distinguished and discussed separately.

Purpose

Intermittency has different meanings and is used ambiguously in different fields and publications. Small-scale (internal) intermittency is the deviation from self-similarity, external intermittency is irregular occurrence of strong disturbances. Often they have something to do with each other. However, it is a subject of on-going debate how to measure and quantify it. We investigated intermittency in a helicon-plasma device. Helicon plasmas are low-temperature plasmas, driven by a radio frequency source and contained in a magnetic field. They are connected to research in fusion plasmas, because both systems feature some linear instabilities. One particular example is the drift wave, which are expected to drive the turbulence in these systems. They alter the intermittency, because intermittency is a universal feature in turbulence. Intermittency is also discussed in other subfields of turbulence, e.g. neutral fluids. Testing different parameters for their intermittency display may help to connect both fields and give an answer to the question, if turbulent plasmas have similarities to these fields.
In the context of fusion plasmas intermittency was described with skewness and (less often) kurtosis [1]. A tool to describe intermittency taken from turbulent flows already used for plasmas is the structure function analysis [2, 3]. An intermittency parameter C(1) [4] was proposed to measure intermittency. And lastly the burstiness is used to measure intermittency [5]. This research aims to compare each method with data collected by the helicon-plasma device PANTA [6] and conclude which is suited to describe intermittency.

Experimental method

The PANTA experiment consists of a NAGOYA-III antenna, an approximately 4m long and 45cm in diameter vacuum vessel, 17 coils to create the magnetic field and a Langmuir probe array with 64 radially aligned probes see fig. 1. All experiments were supervised by Prof. Dr. Chanho Moon and performed by the team from University of Greifswald and RIAM together. The current generating the magnetic field is adjustable. Magnetic field strengths B=[70,80,90,100,110,130] mT were utilized. All experiments were carried out with an argon pressure of p_{Ar}=0.5 Pa and power P = 3kW and heating frequency of 7 MHz.

The magnetic field was varied, because we assumed, that the density gradient between the plasma and vacuum vessel steepens. This would lead to increased drive of the drift wave, turbulence and variation of intermittency. The 64-channel Langmuir probe array [7] features a probe distance to the center of 4cm, where the gradient should be the steepest. The azimuthal distance between the probes is 3.9mm.

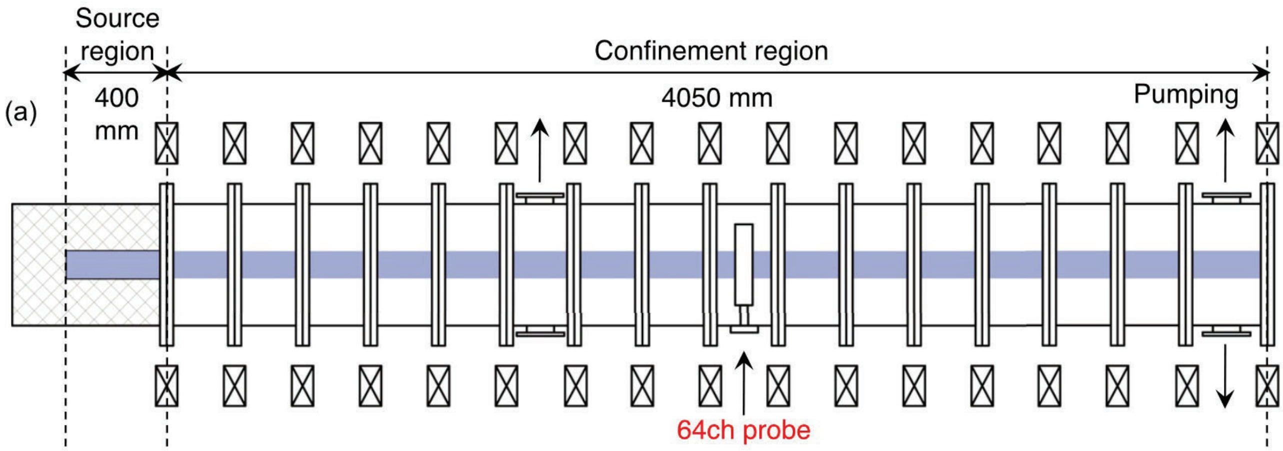

Figure 1: Scheme of the PANTA experiment. Source at the left, termination plate at the right. Crossed boxes indicate field coils. The utilized probe array is placed approximately in the center.

For this research 3 probes were used. One measured the ion-saturation current I_{sat} and two neighbouring probes the floating potential V_{fl}. Both signals of the floating potential were averaged to calculate V_{fl} at the position of the I_{sat} probe. A typical time length of one measurement is 400ms. PANTA features a so-called “solitary wave” at around B=90mT [8]. Whether this wave results in increased or reduced intermittency is a subject of this research and used to value the aforementioned methods. This in combination with the steepening of the density gradients and therefore increasing turbulence are used as qualifiers.

Experimental results

Steepening of gradients

At first we verified that the gradients are indeed steepening with increasing magnetic fields. The density for varying fields at different radial positions is shown in fig. 2. These measurements were recorded with a radial adjustable Reynolds probe located nearby to the probe array.

We are excited to share the findings from our series of measurements, although they have shown densities lower than formerly reported values and below the threshold known as helicon discharges, providing us with valuable new insights. The flanks of the sample were not steepening, which we believe is maybe caused by oxide contamination during measurement, because oxide can act as an electron sink. Our team is actively analysing these preliminary results and is eager to present our findings to the community.

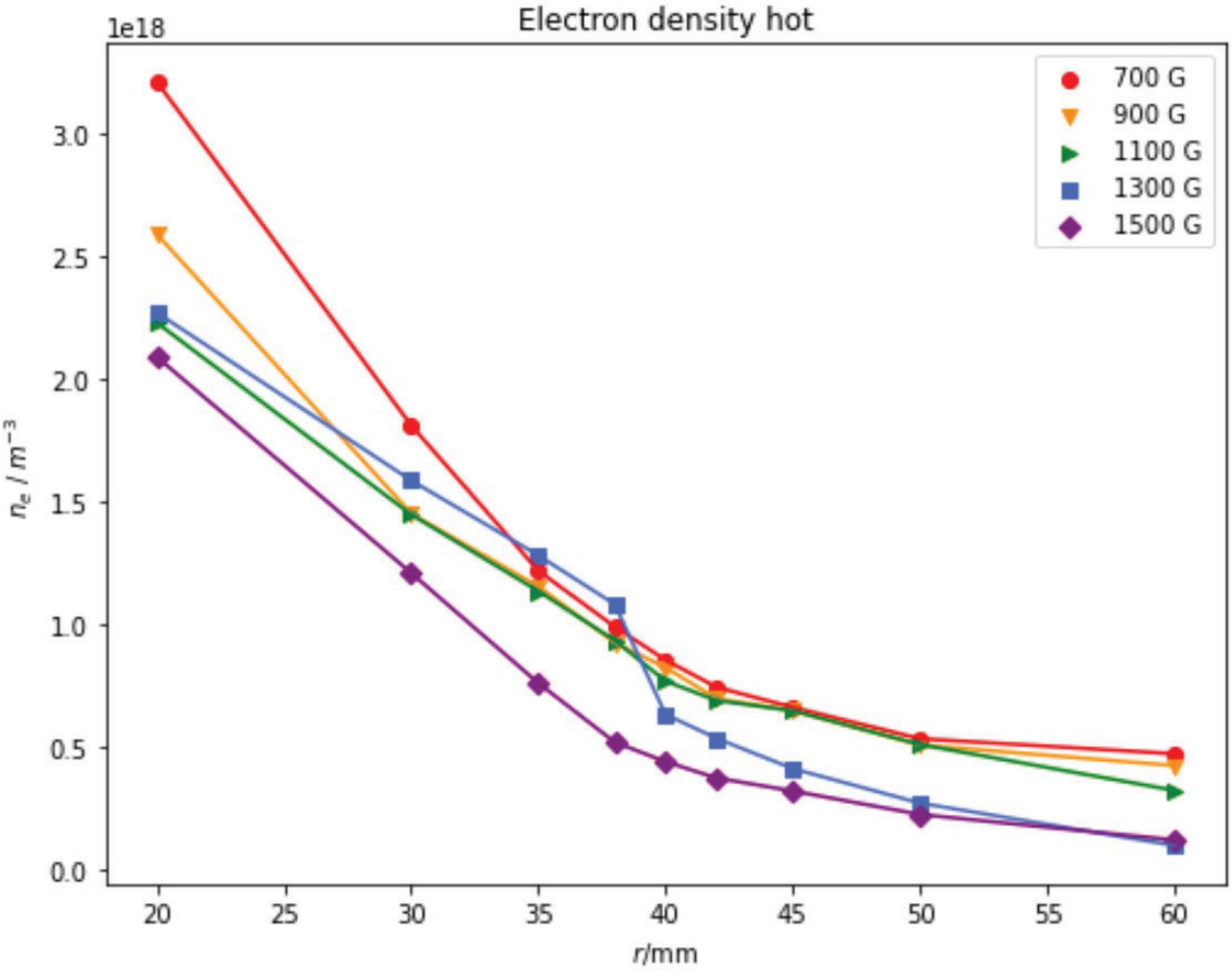

Figure 2: On the y-axis the plasma density is displayed and on the x-axis the radial position of the probe. Colour-coded are different magnetic field strengths

Skewness and kurtosis

Skewness and kurtosis are two important measures in statistics that describe the shape and behaviour of a data distribution. Skewness measures the asymmetry of the data distribution, while kurtosis measures the peakedness or flatness of the distribution. A positive skewness indicates that the majority of the data is on the right side of the distribution, while a negative skewness shows that the majority of the data is on the left. Kurtosis, on the other hand, measures the concentration of data around the mean, with a high kurtosis indicating a tightly packed, peaky distribution and a low kurtosis indicating a flat distribution. Kurtosis is therefore often called the "flatness" parameter. Kurtosis in this research is the excess kurtosis.

Skewness for both I_{sat} and V_{fl} suggests an asymmetry for B < 90 mT. From 90 mT towards higher magnetic field strength, we expect the transition from the phase-locked state to the weakly turbulent state. As turbulence shows near Gaussian statistics, the reduction of skewness and kurtosis can seen as sign of this transition. The kurtosis of V_{ffl} does not seem to follow a general trend and is thus assumed to randomly distributed around zero. The kurtosis of I_{sat} however does exhibit a jump at B = 90 mT, which is at the solitary wave.

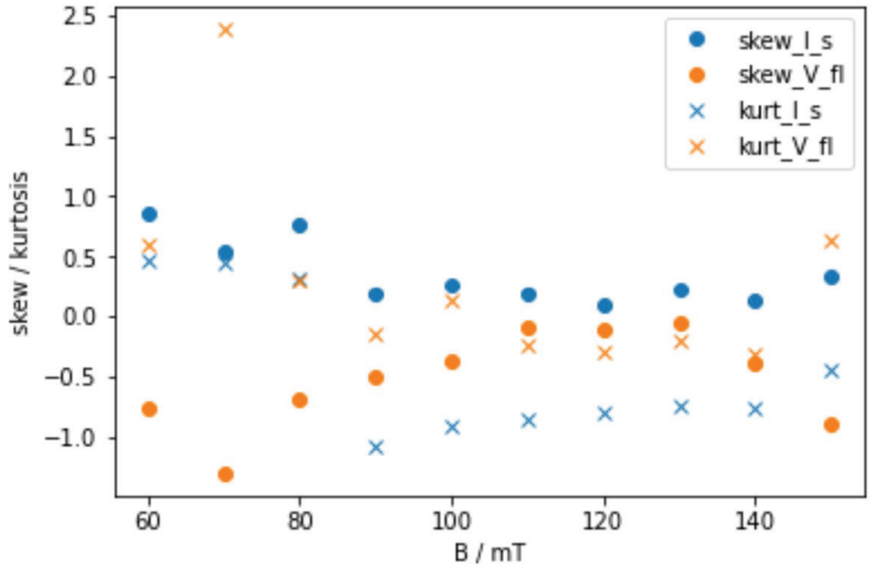

Figure 3: Skewness and excess kurtosis for I_{sat} and V_{fl} as a function of the magnetic field strength.

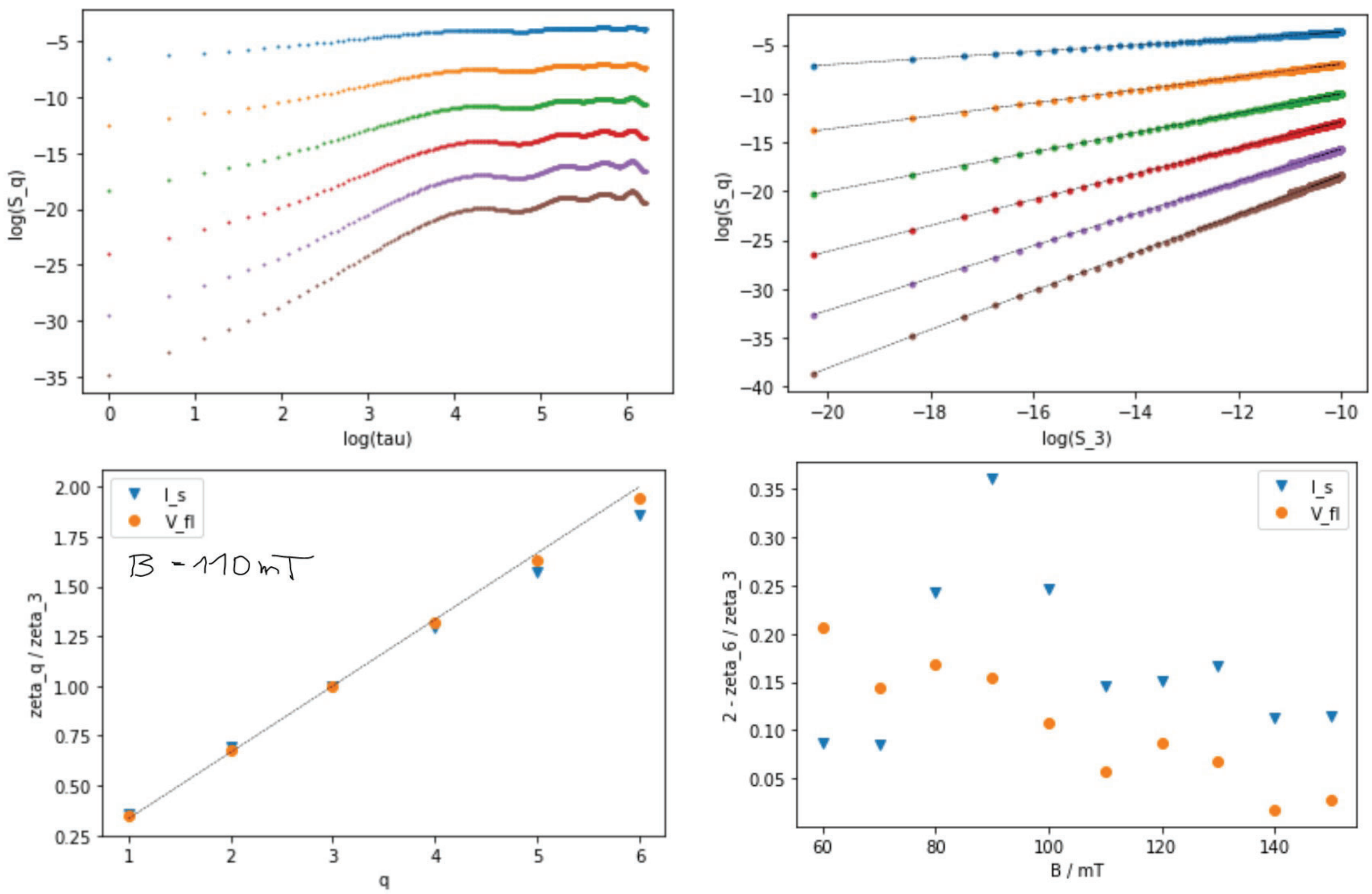

Figure 4: Structure function analysis. Top-left: Example structure functions calculated from $I_{sat.}$ Different colours belong different orders q. Top-right: Structure functions plotted against S_3 to highlight the power-law behaviour. Bottom-left: Structure function coefficients plotted against q with the dashed line being q/3. Bottom-right: Normalized structure function coefficients plotted against magnetic field strength.

Structure function analysis

The calculation of high-order structure functions is a well-established technique in the analysis of turbulence in data series. It offers a more conventional method of examining the intermittency of turbulence. The structure function analysis for this project is summarized in fig. 4. the graph in the top-left shows structure functions against the time delay in a double logarithmic plot. A saturation occurs after 10ms, which two magnitudes above the expectation from fusion devices. By plotting the structure functions against the third-order structure function, a wider region with a power-law scaling becomes apparent, as illustrated in fig. 4 top-right. For fig. 4 bottom left shows structure function exponents calculated from the slopes plotted against their order for I_{sat} and V_{fl} at B=110 mT, the dashed line corresponds to q/3 as proposed by [9] indicating the self-similar case. For q > 3 values divert from the line, which indicates intermittency. I_{sat} shows a larger deviation than V_{fll}, meaning that V_{fl} is more self-similar, but both values show intermittency. Finally fig. 4 bottom-right shows the intermittency level represented by 2-zeta$_6$/zeta$_3$. As expected from fig. 4 bottom-left and previous studies [3] V_{fl} is less intermittent than I_{sat}. As with the kurtosis I_{sat} exhibits a prominent maximum at B = 90 mT. V_{fl} shows a general down-wards trend, as expected for the transition to drift-wave turbulence. Which is in very good agreement with the skewness and kurtosis analysis and our expectations.

Intermittency parameter proposed by van Milligan

A way to calculate the intermittence is proposed by van Milligan et al [4]. By evaluating time windows of a given time series, calculating exponents a so-called intermittency parameter C(1) (for q=1) is gained. It ranges from 0 to 1, while 0 means a monofractal time series. C(1) as a function of B is shown in fig. 5. Our experiments have shown exciting results for C(1), which is higher than expected from previous experiments [4], with values ranging between 0 and 0.15. The data also highlights a remarkable drop in intermittent behavior at B = 90mT for I_{sat}, and a local maximum for V_{fl} at the same magnetic field, further emphasizing the potential importance of C(1) in these studies. These observations suggest that V_{fl} is the more intermittent parameter, providing valuable information for future analysis.

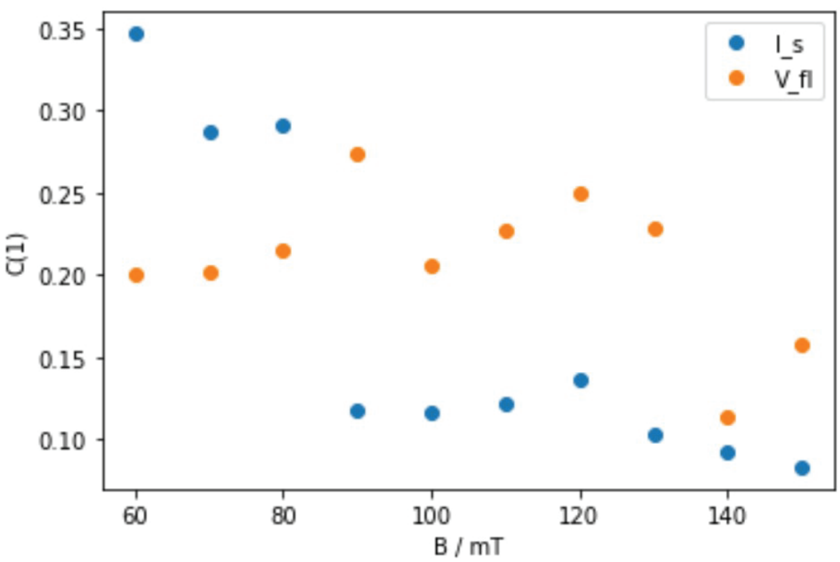

Figure 5: C(1) as function of B for I_{sat} and V_{fl}.

Pulse duration average waiting time and Hurst parameter

Although mentioned the pulse duration has not yet been evaluated. Instead the Hurst parameter was calculated, as the Hurst parameter, also known as the Hurst exponent, is a statistical measure used to quantify the long-term memory or persistence of a time series. It ranges between 0 and 1 and indicates whether a time series has a tendency towards mean reversion (Hurst exponent close to 0.5) or trend persistence (Hurst exponent close to 0 or 1). The Hurst parameter was calculated by two means: first by the scaling properties of the structure function and second by the rescaled range algorithm. The results are shown in fig. 6.

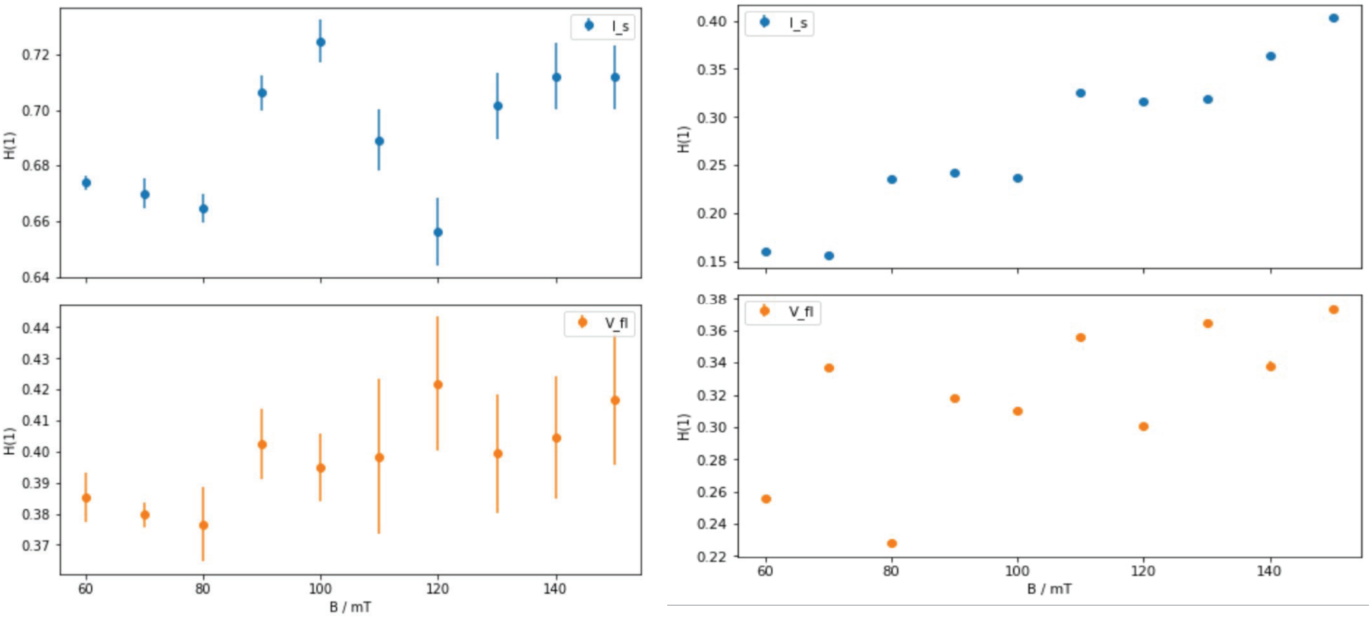

Figure 6: Calculated Hurst exponents. Left: by means of scaling of the structure function. Right: by means of rescaled range.

Both ways agree with each other and our findings with other methods that V_{fl} is almost randomly distributed. However one assumes I_{sat} to be persistently rising and the other persistently falling, confirming differences of both calculation methods already reported for plasma physics [10].

Discussion

Our research team has explored new and innovative methods to evaluate the intermittency in a turbulent plasma. Although the densities were lower and their profiles not steepening our preliminary results are most promising and are valuable information for future analysis. The use of skewness and kurtosis to measure the asymmetry and peakedness of the data was insightful, with I_{sat} exhibiting a jump at 90 mT, that met our expectations for intermittency. The structure function analysis was particularly noteworthy, showing that both I_{sat} and V_{fl} exhibit intermittency, with I_{sat} being more intermittent than V_{fl}. Additionally, the intermittency parameter proposed by van Milligan revealed that C(1) was higher than expected, with I_{sat} showing a drop in intermittency behaviour at 90 mT. While there was a contamination during measurement, which is reflected in the results, we are confident that a stronger variation in the density gradient length scale would yield great results. Overall, the structure function analysis appeared to be the closest to our expectations, featuring controllable steps to evaluate, and the most prominent reaction to the solitary wave.

List of publications

[1] B Nold et al 2010 Plasma Phys. Control. Fusion 52 065005
[2] C. X. Yu et al Physics of Plasmas 10, 2772-2779 (2003)
[3] S. Garland et al Physics of Plasmas 24, 112307 (2017)
[4] B. A. Carreras et al Physics of Plasmas 7, 3278-3287 (2000)
[5] O.E. Garcia Phys. Plasmas 23, 052308 (2016)
[6] T. Yamada et al., Plasma and Fusion Research 3, 044 (2008)
[7] T. Yamada et al., Review of Scientific Instruments 78, 123501 (2007)
[8] T. Kobayashi et al., Plasma and Fusion Research 12, 1401019 (2017)
[9] V P Budaev et al 2008 Plasma Phys. Control. Fusion 50 074014
[10] M. Gilmore et al, Physics of Plasmas 9, 1312 (2002)

List of participants (specify the affiliation, division, and job title)

KNAUER, stefan; University of Greifswald, Physics department; Researcher
MANZ, peter; University of Greifswald, Physics department; Professor
MOON, chanho, RIAM, Assistant professor

国際化推進共同研究概要

No. 10

22NU-7

タ イ ト ル： Quasi-coherent modes in the linear magnetized plasma device PANTA

研究代表者： FAHRENKAMP Nils

所内世話人： 文　贇鎬

研 究 概 要：

直線装置 PANTA における準コヒーレントモードに超統計（Superstatistics）方法を適用してみた。コヒーレントモードによる輸送の時間スケールは、拡散部分と対流部分に主に依存することが分かった。一方、密度乱流の条件 $\kappa=3$ は、平衡的な輸送時間スケールにならなかった。これは磁化プラズマにおける $E\times\mathrm{B}$ 速度の揺動や粒子輸送 Γ を直接計測して、その理由について調べる必要があると考えられる。

Quasi-coherent modes in the linear magnetized plasma device PANTA (10_22NU-7)

N. Fahrenkamp
Institute of Physics, University of Greifswald, Felix-Hausdorff-Str.6, 17489 Greifswald, Germany

I. ABSTRACT

We will describe the quasi-coherent modes in PANTA by superstatistics [1]. The theory of the superstatistics decribes the appearance of non-Gaussian statistics when two different time scales are present. Usually two time scales are important for the appearance of the quasi-coherent mode, a fast and a slow time scale. The slow time scale will be identified as the time scale where the signal shows a behavior close to Gaussian statistics. The statistical analysis can be done with most of the diagnostics in PANTA, but for mode identification a probe head like in [2] is used. For the future also the tomographic system [3] would be very helpful.

II. BACKGROUND

In tokamak based magnetized confined fusion recently edge-localized-mode-free confinement regimes have become of major interest. A main feature of ELM-free regimes is the appearance of quasi-coherent modes leading to continuous transport. (Examples are the WCM in I-mode and QCM in EDA-H-mode.) Interest in this topic from the fusion side is rather since a short time. Quasi-coherent modes have long been observed in PANTA and similar linear plasma devices. Examples in PANTA are the streamer and the solitary wave [4]. Quasi coherent modes tend to behave intermittent in tokamaks [5] and also in PANTA [6]. There has not been a comparison of quasi-coherent modes in tokamaks and linear devices so far. This collaboration with RIAM allows us to study the physics of quasi-coherent modes in detail in linear magnetized laboratory plasmas as it is in PANTA. Findings can then be applied to the edge of magnetically confined fusion experiments.

Transport codes use either a diffusive, convective or a combinational ansatz of both to describe the transport. Likewise, experimental data are interpreted in this way. In particular in the scrape-off layer, turbulent transport does not follow Gaussian statistics and furthermore cannot be decomposed into an effective diffusivity and convective velocity [7–9], it is often desirable to describe the transport in this decomposition.

The decomposition into a diffusive and a convective part may depend on the time scale the transport is considered [10]. Here we want to demonstrate that this is the case.

III. EXPERIMENTAL METHOD

A. Data Aquisition

For this purpose the probe head like in Ref. [2] is used to record a biased saturation current signal I_{sat} and two signals of the plasma floating potential Φ_{fl}. The floating pins are positioned at opposite sides of the biased pin and all three pins are aligned perpendicular to the axis of the main chamber. To estimate the density gradient also a probe array measuring the profile simultaneously is used.

Plasma shots are performed with a total length of $t = 600$ ms. A timeframe is chosen where the plasma is build up fully and stable signals are acquired. This is typically the full time interval between $t_1 = 250$ ms and $t_2 = 500$ ms. The experiment was performed at a magnetic field strength of $B = 1300$ G, a base gas pressure of $p = 0.5$ Pa and a RF-heating power of $P = 3$ kW. The probe head was located at a radial position of $r = 40$ mm in an axial distance of around 2 meters to the plasma-source.

The QCM does occur close to $B = 900$ G, thus at lower magnetic field strength than the case considered here. However, to interpret the results, we first wanted to look at a case without QCM.

B. Convective or diffusive transport

We will estimate the turbulent transport $\langle\Gamma\rangle_\tau = \langle\tilde{u}_r\tilde{n}\rangle_\tau$ averaged for different subwindow sizes τ, with $\tilde{u}_r$ as fluctuations of the radial $E \times B$ velocity and $\tilde{n}$ as density fluctuations. In the used experimental setup of PANTA as a linear magnetized plasma device $\tilde{u}_r = -\partial_y\tilde{\Phi}_{fl}/B$ and $\tilde{n} \propto \tilde{I}_{sat}$. With $\tilde{\Phi}_{fl}$ as fluctuations of the floating potential and $\tilde{I}_{sat}$ as fluctuations of the saturation current of the plasma. Each one of the needed variables is calculated for every subwindow defined by a fixed subwindow size τ to calculate individual Γ. Subsequently they are averaged over all subwindows for a fixed τ to obtain $\langle\Gamma\rangle_\tau$.

This calculated transport is decomposed into convective and diffusive components:

$$\langle\Gamma\rangle_\tau = -D\left\langle\frac{dn}{dr}\right\rangle_\tau + U\langle n\rangle_\tau. \tag{1}$$

This can be best shown as

$$\frac{\langle\Gamma\rangle_\tau}{\langle n\rangle_\tau} = D\frac{-\langle\frac{dn}{dr}\rangle_\tau}{\langle n\rangle_\tau} + U. \tag{2}$$

This linear relationship shows the diffusive part as the slope and the convective part as the offset of the linear function. We estimate also the coefficient of determination R^2 for each τ. This provides a measure of how well the transport is described by the assumption that the transport can be decomposed into convective and diffusive components.

Likely the transport should be more convective at small τ and more diffusive for large τ [10].

C. Superstatistics

As diffusive transport is associated to Gaussian statistics. We extract a long time scale τ_{SS} following the approach of the superstatistic [1]. The time series is divided in subwindows of size τ. By integrating the local flatness $\int_0^{t_{max}-\tau} dt$ over the subwindows $\langle\cdot\rangle_{t,\tau} = \int_t^{t+\tau} d\acute{t}$ and averaging over the ensemble of subwindows

$$\kappa(\tau) = \frac{1}{t_{max}-\tau}\int_0^{t_{max}-\tau} dt\frac{\langle(\tilde{n}-\bar{\tilde{n}})^4\rangle_{t,\tau}}{\langle(\tilde{n}-\bar{\tilde{n}})^2\rangle_{t,\tau}^2} \tag{3}$$

a time scale full filing the condition

$$\kappa(\tau_{SS}) = 3 \tag{4}$$

can be found. Clearly this condition simply implies that we are looking for the simplest SS, a superposition of local Gaussians, which have local flatness 3 or a kurtosis of zero, respectively [1]. This time scale can be compared to the findings above. In Refs. [7–9] one sees that the occurrence of short living fluctuations leads to deviations from linear behavior with respect to Eq. (2). Since diffusive transport is described with Gaussian statistics, this should correspond to the case of a kurtosis of zero. Therefore, one could expect that the transport can be explained well by diffusive transport and the fit with the help of Eq. (2) yields good results for this particular time scale.

IV. EXPERIMENTAL RESULTS

The SS method works. By definition, κ is small for small τ. Since for large τ, κ increases above three (Fig. 1), we can determine τ_{SS}. This is approximately $\tau_{SS} \approx 1.5$ ms. The value is about where one would intuitively guess the equilibrium time of such discharges to be.

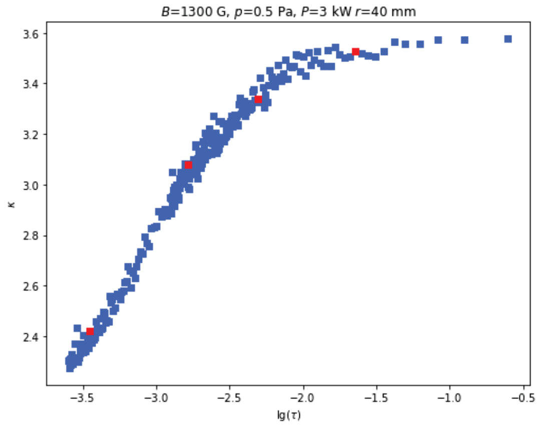

FIG. 1: Values of calculated κ from (3) for a high variation of timewindow-sizes τ. Marked in red are 4 arbitrarily chosen values to be compared. The exact values can be found in Fig. 2

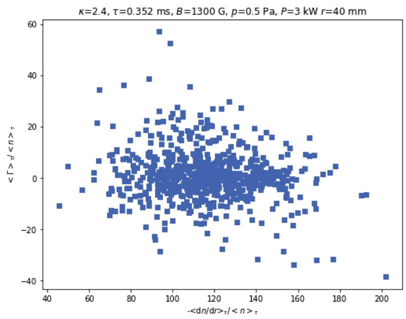

(a) $\kappa = 2.4$ and $\tau = 0.352$ ms

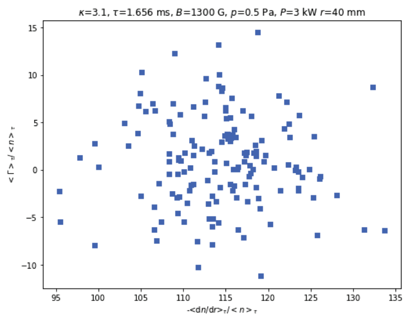

(b) $\kappa = 3.1$ and $\tau = 1.656$ ms

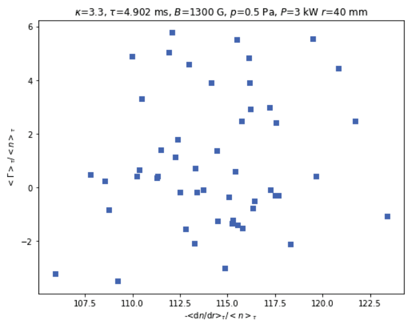

(c) $\kappa = 3.3$ and $\tau = 4.902$ ms

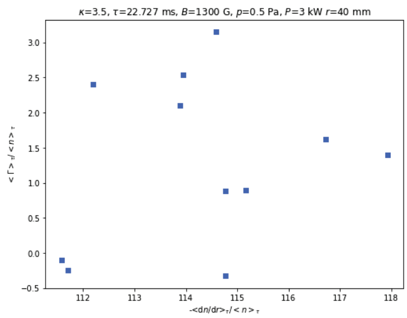

(d) $\kappa = 3.5$ and $\tau = 22.727$ ms

FIG. 2: Plots in reference to (2) for different τ and κ

In the next step, according to Eq. (2) we show $\frac{\langle \Gamma \rangle_\tau}{\langle n \rangle_\tau}$ against $\frac{\langle \frac{dn}{dr} \rangle_\tau}{\langle n \rangle_\tau}$. The slope shows the diffusion coefficent, the offset the convection coefficient and the scatter shows how well the description applies. We show this in Fig. 2 for different κ values ($\kappa \in [2.4, 3.1, 3.3, 3.5]$). For kappa values close to three, we expect better agreement. The measuring points show up as clouds, distinct structures cannot be recognized here. The data are not well describable via this diffusive-convective approach.

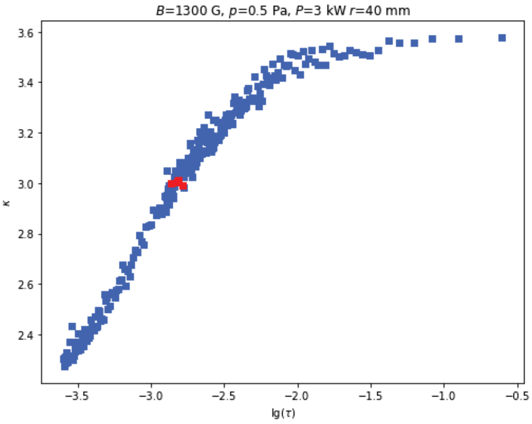

FIG. 3: Values of calculated κ from (3) for a high variation of timewindow-sizes τ. Marked in red are 5 timewindows with a $\kappa = 3.00 \pm 0.01$

.

The determination of diffusion coefficients is also ambiguous. There are different time window widths which all result in $\kappa = 3$. These are $\tau_{SS} \in [1.645, 1.534, 1.524, 1.506, 1.374]$ ms as shown in Fig. 3. If we average them over these window widths, we get completely different slopes and thus completely different diffusion coefficients (Fig. 4). These even show inward or outward transport, so we can't even reliably determine the direction of transport.

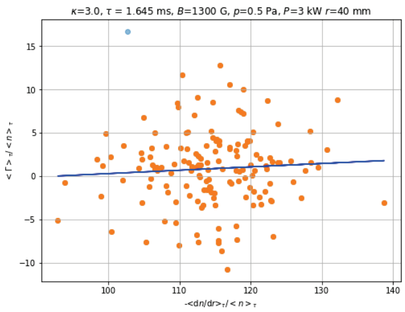

(a) $\tau = 1.645$ ms

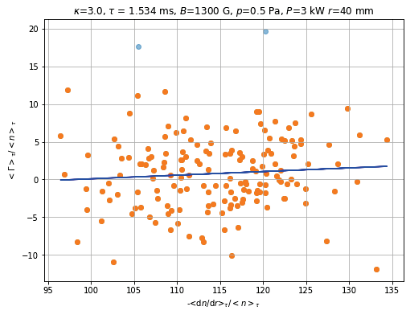

(b) $\tau = 1.534$ ms

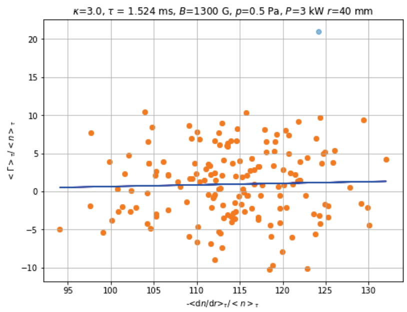

(c) $\tau = 1.524$ ms

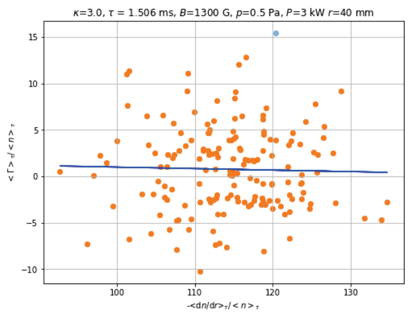

(d) $\tau = 1.506$ ms

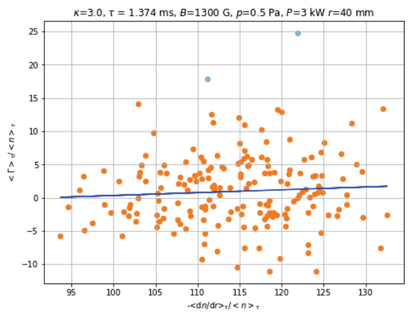

(e) $\tau = 1.374$ ms

FIG. 4: Linear fits of the 5 timewindow-sizes τ marked in Fig. 3

Nevertheless, we did this out of interest. Figure 5 shows the diffusion and convection coefficients as a function of the sub window width τ in a logarithmic representation. The diffusion coefficient D ranges from -0.1 to 0.4 m^2/s depending on the tau. The convection coefficient from $+20$ to -50 m/s. Values below $\kappa < 3$ tend to diffusive inward transport with a clear convective component to the outside. Values around $\kappa = 3$ have low diffusion and convection coefficients. In the range $\lg(\tau)$ between -2 and -1.5 there is strong outward diffusion, which is compensated with a linear inward pinch. It is the other way around, as for small time scales. For the largest time scales, the coefficients are again close to zero. Here the ensemble number is very low, the results here are probably not statistically significant at the longest time scale. In conclusion, the interpretation depends totally on the time scale with which it is considered. The coefficient of determination R^2 increases with the sub window size τ (Fig. 6). But of course this is only due to the fact that fewer measuring points are available. A clear local maximum is not seen here.

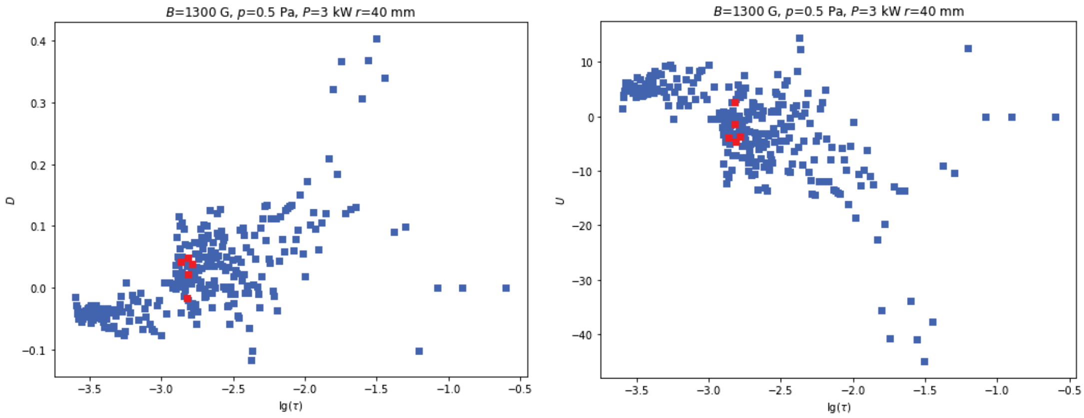

(a) Diffusive part, D, of the linear fit from (2) over $\lg(\tau)$

(b) Convective part, U, of the linear fit from (2) over $\lg(\tau)$

FIG. 5: The diffusive and the convective part, D and U, of the linear fit from (2) for every timewindow-size τ on a logarithmic scale. Marked in red are the 5 timewindows with a $\kappa = 3.00 \pm 0.01$ from Fig. 3

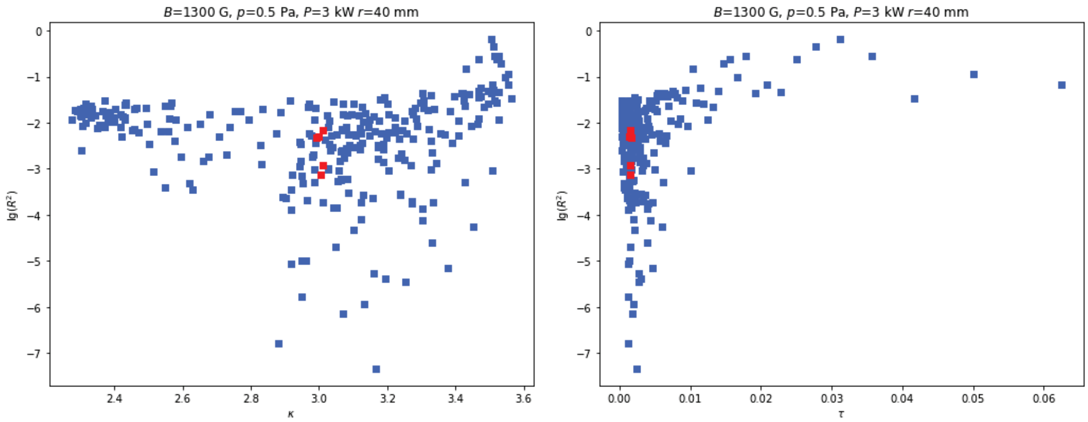

(a) $\lg(R^2)$ over κ

(b) $\lg(R^2)$ over τ

FIG. 6: Coefficient of determination R^2 for each calculated κ and τ. Marked in red are the 5 timewindows with a $\kappa = 3.00 \pm 0.01$ from Fig. 3

V. CONCLUSION AND OUTLOOK

The method of superstatistics is applicable in principle to data from PANTA. We have also shown that the interpretation of the transport depends on the time scale at which it is considered. The condition $\kappa = 3$ for the density fluctuations seems not to provide the equilibrium time scale. But maybe this was the wrong field after all, maybe it would be better to do this with the $E \times B$ velocity fluctuations or directly with the transport Γ.

As a next step, we should determine the superstatistics time scale from these other fields and best find estimates in the literature for the time scale of equilibrium in linear plasma experiments.

[1] C. Beck, E. G. D. Cohen, and H. L. Swinney, Phys. Rev. E **72**, 056133 (2005).
[2] T. Kobayashi, S. Inagaki, Y. Kosuga, M. Sasaki, Y. Nagashima, T. Yamada, H. Arakawa, N. Kasuya, A. Fujisawa, S.-I. Itoh, et al., Physics of Plasmas **23**, 102311 (2016).
[3] C. Moon, K. Yamasaki, Y. Nagashima, S. Inagaki, T. Ido, T. Yamada, Y. Kasuya, N. Kosuga, M. Sasaki, Y. Kawachi, D. Nishimura, et al., Scientific Reports **11**, 3720 (2021).
[4] T. Kobayashi, S. Inagaki, M. Sasaki, , Y. Kosuga, H. Arakawa, F. Kin, , T. Yamada, , et al., Plasma and Fusion Research **12**, 1401019 (2017).
[5] T. Happel, P. Manz, F. Ryter, P. Hennequin, A. Hetzenecker, G. D. Conway, L. Guimarais, C. Honoré, U. Stroth, E. Viezzer, et al., Nucl. Fusion **56**, 064004 (2016).
[6] T. Kobayashi, S. Inagaki, M. Sasaki, Y. Kosuga, H. Arakawa, T. Yamada, Y. Nagashima, Y. Miwa, N. Kasuya, A. Fujisawa, et al., Physics of Plasmas **22**, 112301 (2015).
[7] O. Garcia, J. Horacek, R. Pitts, A. Nielsen, W. Fundamenski, V. Naulin, and J. J. Rasmussen, Nuclear Fusion **47**, 667 (2007), URL `https://dx.doi.org/10.1088/0029-5515/47/7/017`.
[8] O. Garcia, R. Pitts, J. Horacek, A. Nielsen, W. Fundamenski, J. Graves, V. Naulin, and J. J. Rasmussen, Journal of Nuclear Materials **363-365**, 575 (2007).
[9] V. Naulin, Journal of Nuclear Materials **363-365**, 24 (2007).
[10] P. Manz, C. Hufnagel, A. Zito, D. Carralero, M. Griener, T. Lunt, O. Pan, M. Passoni, B. Tal, M. Wischmeier, et al., Physics of Plasmas **27**, 022506 (2020).

国際化推進共同研究概要

No. 11

22NU-8

タ イ ト ル： High power mm wave transmission line technology for advanced fusion devices

研究代表者： LECHTE Carsten Hanno

所内世話人： 出射　浩

研究概要：

国際熱核融合実験炉（ ITER ）実験では、プラズマパラメータ分布の詳細な細部制御により、燃焼プラズマを閉じ込めることが重要である。電子サイクロトロン加熱・電流駆動では、局所的にプラズマ電流を駆動することで不安定性（磁気島）を抑制することが期待されている。磁気島は kHz～10 kHz 程度の周期でプラズマ断面を回転する。磁気島の回転に併せて局所電子サイクロトロン加熱・電流駆動することで高効率な抑制が可能となる。現在、kHz～10 kHz で入射位置を変えるスイッチ素子が開発中である。九州大学での低電力試験後、量子科学技術研究開発機構（QST）で高電力試験を行ったが、スイッチボックス内でアーキングが発生した。アーキング抑制に向け、スイッチボックス内のミラーを精査し、ミラー面での損傷を確認した。今年度はドイツでのミラーシステムの再製作を進め、併せてアーキングの抑制を確実とするため、スイッチボックス内でのストレー波成分を吸収する吸収体の設計を進めた。

Report of international collaboration 2022NU-8 between RIAM and IGVP in FY2022: The MQIV FADIS diplexer for ITER with automatic tuning at QST

Mr. Dr. Carsten Lechte

Introduction: The MQIV diplexer developed at IGVP is a fast switch, power combiner, and mode filter for megawatt power 170 GHz millimeter waves using a Fabry-Perot resonator in a compact box design that is vacuum capable and can be directly interfaced with the 63.5 mm ITER ECRH waveguides which are available at QST. The device has 2 input and 2 output ports, which are connected as shown in Fig. 1. Our technical partners at TNO in the Netherlands have designed and built a fast mechanical tuning control unit for the device that is also vacuum-compatible.

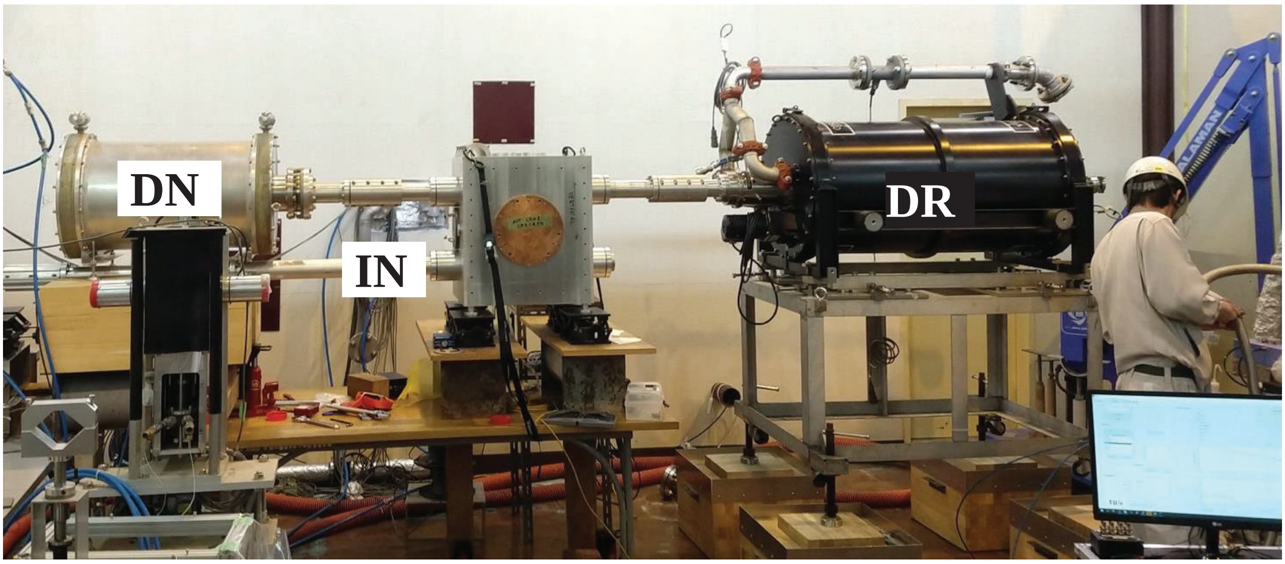

Fig 1: Diplexer integration into the gyrotron test stand at QST. DN and DR are the dummy loads at the non-resonant and the resonant channel, respectively, and IN is the input waveguide.

The highpower tests have demonstrated the switching capability of the device, but also highlighted problems with arcing and stray radiation. Both were addressed in 2022.

Since no travel to Japan was possible in 2022, the work was either of theoretical nature (design and analysis), or parts sent to IGVP for remanufacturing.

Arc mitigation: It was found in 2020 after electropolishing of the problematic mirror surfaces, that the material defects in the surfaces were not just irregularities in shape, but there could also be cavities which outgas material that is then causing the arc. After careful analysis of the video footage from some arcing events, it was decided to return the mirrors to IGVP, where a galvanically deposited “known-good” copper layer will be put down, and the 4 surfaces of the main resonator, which see the greatest incident power, will be re-machined.

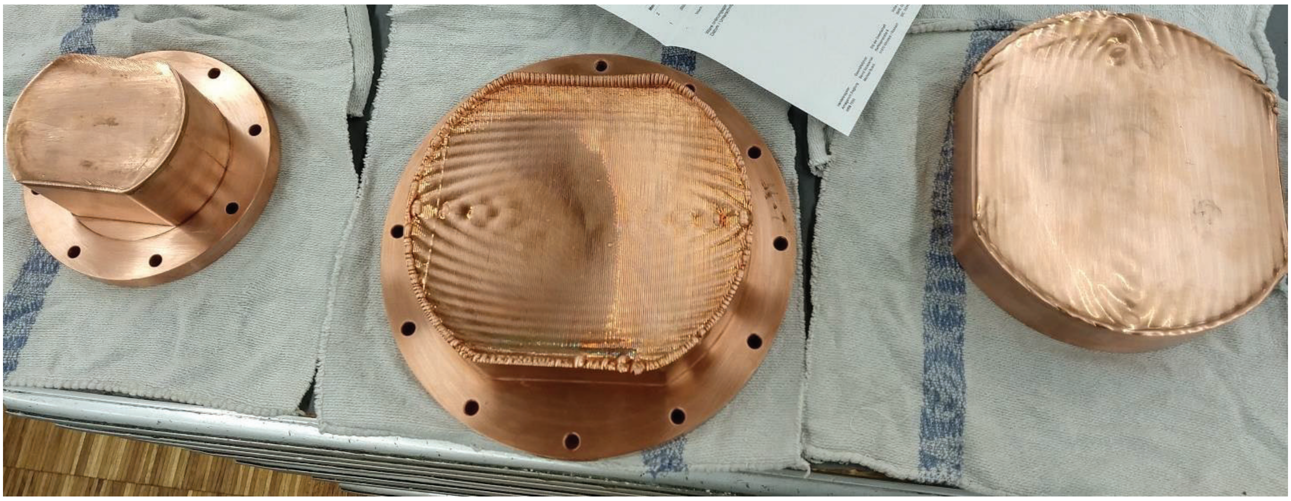

Fig.2: Three of the four mirrors after galvanic treatment, before final machining.

Stray radiation mitigation: IGVP has expertise in designing and fabricating resonant ceramic absorber coatings. Six absorber plates covering the six internal surfaces of the device were designed and are being fabricated at the IGVP workshop and at our collaborating partner IFKB at Stuttgart University.

The absorber consists of 8 mm aluminium plates with coutouts for all the mirrors, waveguide ports, and observation ports that will be press-fit into the diplexer box (see Fig. 3). The absorbing coating of aluminium and titanium oxide is applied by an atmorpheric plasma spraying process to a thickness of approximately 100 µm. It has a high (>70%) single pass absorption at 170 GHz from all but the shallowest angles. Cooling is achieved by radiation and contact with the box structure. Since only a fraction of the input power should end up as stray radiation, the absorbers should be able to cool down between shots if a duty cycle of 1:20 of power on to power off is adhered to. This duty cycle is also the maximum for the main mirrors.

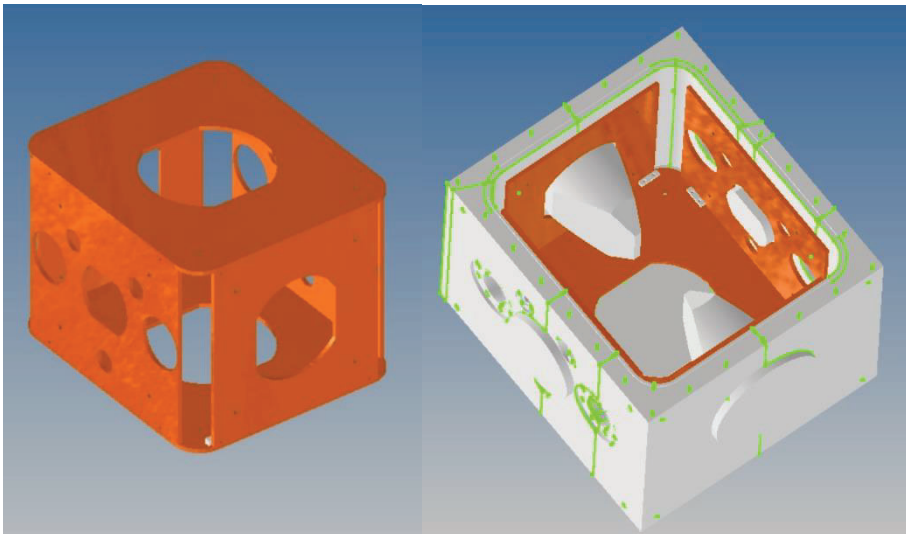

Fig. 3: CAD drawing of the absorber plates.

国際化推進共同研究概要

No. 12

22NU-9

タイトル： Temperature gradient driven self-steepening of solitary drift-waves

研究代表者： MANZ Peter

所内世話人： 文 贊鎬

研究概要：

　孤立ドリフト波は、PANTA および同様の磁化プラズマ装置で広く研究されています。磁化プラズマにおける急峻な波面の形成メカニズムは、以前の研究で提案されています。密度・温度勾配の両方を含む単純な非線形静電ドリフト波モデルでは、電子温度勾配の存在により、Korteweg-de-Vries (KdV) および Burgers 方程式に現れる非線形性が生じます。このような非線形性はトカマクのＩモード閉じ込め領域における密度バーストに関連している可能性があります。I モードのバーストは、孤立した波形を示します。また、I モード閉じ込めは電子温度の強い勾配によって特徴付けられます。 従って、PANTA 実験装置における孤立ドリフト波に対する電子温度勾配の影響を詳細に調べて、トカマクのＩモード閉じ込め体制の結果と比較することが本研究の目的です。

Temperature gradient driven self-steepening of solitary drift-waves (No.12 _ 22NU-9)

Peter Manz , Institute of Physics, University of Greifswald, Germany

Aim : The solitary drift-wave has been extensively studied in PANTA and similar devices [1-5]. A formation mechanism of steep wave fronts in magnetized plasmas has been proposed in [6]. In a simple non-linear electrostatic drift-wave model [7] including both density and temperature gradients, the presence of a gradient in the electron temperature gradient give rise to nonlinearity similar to the nonlinearity appearing in the Korteweg–de-Vries (KdV) and Burgers equations. Such a nonlinearity could be relevant for density bursts in the I-mode confinement regimes of tokamaks [8]. The bursts in the I-mode exhibit a solitary waveform. The I-mode confinement regime is characterized by strong gradients in the electron temperature. It would be interesting to study the impact of the electron temperature gradient on the solitary drift-wave in the PANTA device and compare to results from the I-mode confiement regime in the tokamak.

Background - observations in the I-mode of ASDEX Upgrade Tokamak: Figure 1 shows the amplitude of turbulent fluctuations in L-mode and I-mode in ASDEX Upgrade. In L-mode the fluctuation level is higher, in I-mode it decreases. However, there are density bursts that occur irregularly and carry the transport. The transport in the I-mode is therefore strongly intermittent. The bursts occur as solitary modes. In the conditional average (Figure 2), the waveform appears as a solitary pulse modulated at a lower frequency. In addition, the envelope is asymmetric in time.

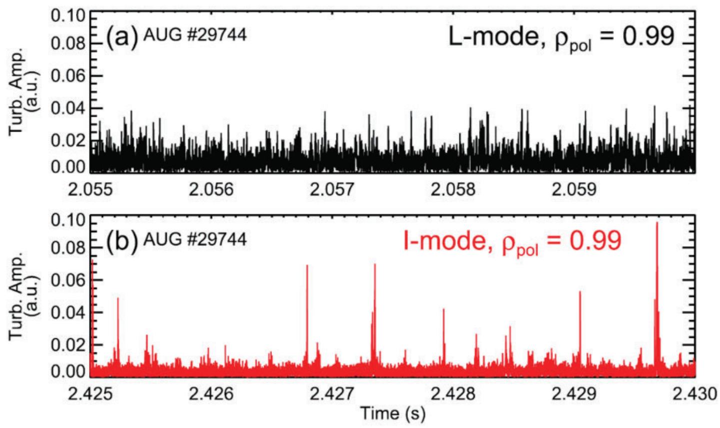

Figure 2Turbulent amplitudes measured with Doppler reflectometry in L-mode and I-mode in ASDEX Upgrade. Figure taken from P. Manz et al. Nuclear Fusion 57, 086022 (2017)

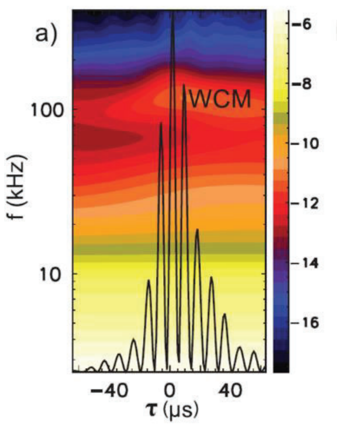

Figure 1 Conditional average of density bursts in I-mode. Figure takenIn from P. Manz et al. Nuclear Fusion 57, 086022 (2017)

experimental method: Experiments have been carried out in the linear magnetized plasma experiment PANTA at RIAM (Kyushu University). The experiments were led by Prof. Dr. Chanho Moon, he was also our first contact. We would like to thank him again for the experiments. PANTA exhibits a length of 4.05 m and a diameter of 45 cm. A homogeneous axial magnetic field up to 150 mT can be generated by a set of Helmholtz coils. The plasma is heated by a double loop helicon source with a diameter of 10 cm at one end of the device. The typical cylindrical plasma radius is 5 cm. At the other end the plasma terminates at a stainless steel end-plate. In PANTA, at higher heating power the electron temperature gradient steepens up [9]. Therefore, it is possible to study the impact of the electron tempertaure gradient on the solitary drift-wave at the same magnetic field strength. Measurements were performed at 3kW, 4.5 kW and 6 kW at the highest possible magent field of 150 mT. Argon has been used as the gas at a pressure of 0.5 Pa. Using radially movable Langmuir probes array, profiles of plasma density and temperature were recorded. In addition, fluctuations in the ion saturation current were measured. These are considered as density fluctuations.

Experimental results:

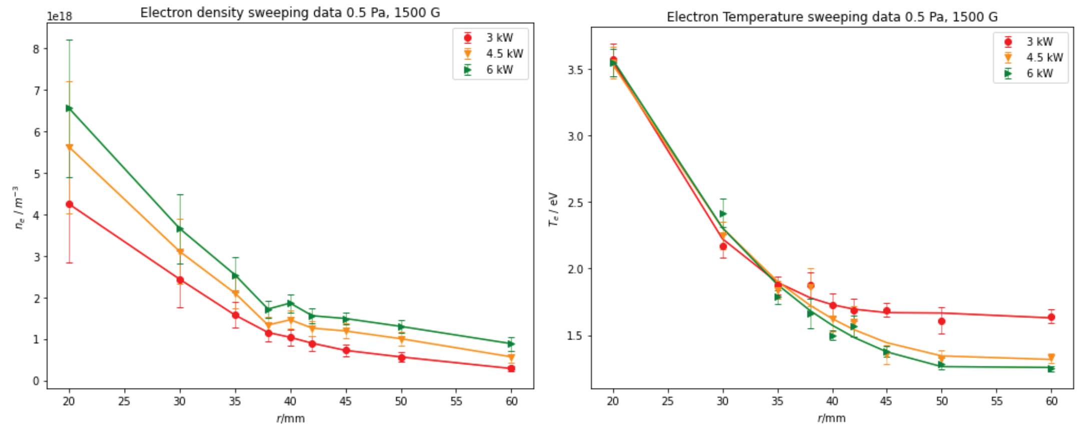

Figure 3 Radial profile of electron density and tempertaure measured in PANTA at B=150 mT, neutral gas pressure 0.5 Pa and heating power P=3, 4.5, 6 kW

The density and temperature profiles are shown here above in Figure 3. The profiles are generally smooth, monotonously falling. These are good measurements. There is a cant at 4 cm in density where the 64ch probe array sits. Unfortunately, this seems to interfere with measurements at higher powers. But this is not so bad right now, we will come back to this later. The plasma densities are slightly lower (factor 2 to 3) than the values usually observed in PANTA. This may not seem so critical at first glance, but it has systematic implications. With increasing heating power, the density in the center increases, the temperature in the center remains rather constant. This is generally the typical behavior for low-temperature plasmas. In the partial balance, ionization (as source) and transport via the sheath (sink) have to balance each other. With more power, more ionization can occur and the plasma density increases with power. In the power balance, heating power and ionization (now as sink) are in balance. In the first order, the temperature is determined by the ionization energy and the plasma volume, which do not change here. Indeed, the temperature in the center does not change much. Helicon plasmas are different, they are characterized by efficient ionization. We would expect that in the center of the discharge, the plasma is almost completely ionized already at 3 kW. This usually seems to be the case, but for some reason we did not reach such high densities this time. Once the plasma is fully ionized, additional heating power cannot be applied for ionization, but the plasma is heated and the temperature rises. The behavior of the profiles with heating power indicates that the plasma densities really were that low.

Nevertheless, we see that in the outer region (r=3.5-4. 5 cm) the temperature gradient becomes steeper with increasing power. Ion-saturation current fluctuations are taken at r=4cm. We substract the mean and devide the data by the standard deviation. The fluctuation are shown as amplitudes to compare with Fig.1.

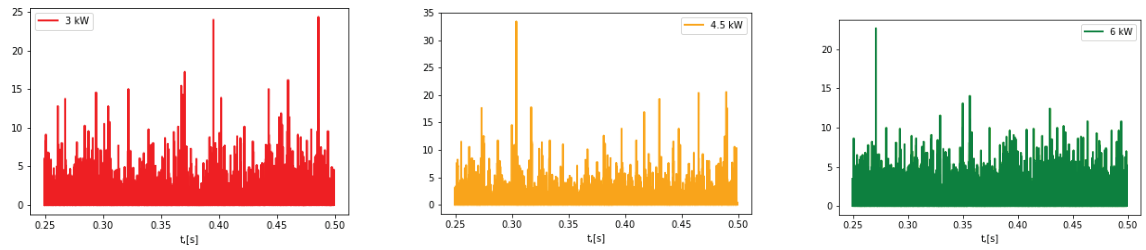

Figure 4. turbulent amplitudes as measured in PANTA at r=4cm, at different heating powers, varying the electron temperture gradient.

Figure 4 shows the turbulent amplitude in PANTA at different heating powers. The base fluctuation levels stays similar. This is different from the I-mode. With increasing heating power, rare strong events become more rare and stronger in amplitude.

We can examine as at r=4 cm whether the waveform becomes more soliton-like. Since we want to investigate rare high amplitude events, we use the conditional averaging technique. For this we define a trigger tau=0, whenever the signal exceeds 2.5 times the standard deviation of the signal and is on the rising edge. Then we cut out subwindows with a half-width of 250 µs from the signal and average over them.

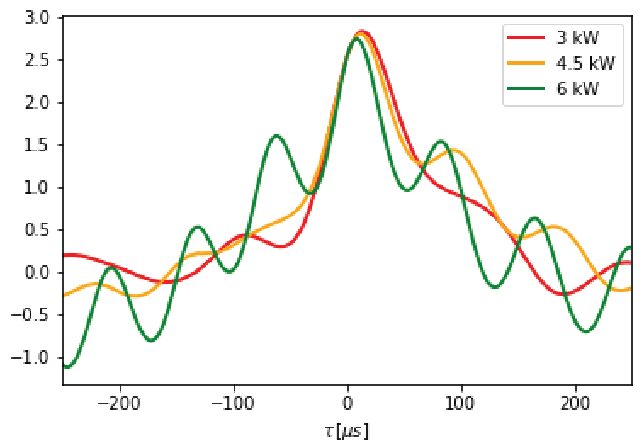

Figure 5. Conditional average of density bursts with varying heating power or electron temperature gradient

The result is shown here on the left hand side. We see a steeper rising edge, and the rising edge also becomes steeper from the power, so the temperature gradient increases. One can already see secondary minima and maxima at 3 kW, but these become more pronounced as the power increases. At 6 kW, mainly the secondary minima and maxima are noticeable. The secondary maxima also move closer to the skin maximum with increasing power. This is remarkable if we look again at the case of the I-mode in ASDEX Upgrade (Figure 2).

Summary and Conclusion: Measurements in PANTA at different electron gradients have been performed. Unfortunately, the densities for helicon discharges were very low. This indicates a bad conditioning of the wall of the experiment. It is necessary to repeat the measurements to confirm the reproducibility of the experiments. With better conditioning, clearer results can be expected. We have made a preliminary analysis. There are similarities to the I-mode turbulence. These results are very promising. Elaborating on these would underscore the importance of smaller laboratory experiments as PANTA to understand turbulence in reactor-relevant regimes of confined fusion plasmas.

References

[1] H. Arakawa et al., Plasma Physics Control. Fus. 53, 115009 (2011)

[2] T. Kobayashi et al., Plasma Fus. Res. 6, 2401082 (2011)

[3] S. Oldenbürger et al. ,Plasma Physics Control. Fus. 54, 055002 (2012)

[4] T. Kobayashi et al. , Physis Plasmas 22, 112301 (2015)

[5] T. Kobayashi et al., Plasma Fus. Res. 12, 1401019 (2017)

[6] M. Sasaki et al., Physis Plasmas 22, 032315 (2015)

[7] H. Tasso, Phys. Lett. 24A, 618 (1967)

[8] T. Happel et al, Nucl. Fus. 56, 064004 (2016)

[9] Y. Kawachi et al., Plasma Fus. Res. 16, 120281 (2021)

国際化推進共同研究概要

No. 13

22NU-10

タ イ ト ル： Improved EFIT code of the plasma equilibrium reconstruction for physical study on QUEST

研究代表者： QIAN Jinping

所内世話人： 花田　和明

研 究 概 要： EAST で実施されている高βｐ放電について世界標準で使用されている平衡計算コード EFIT での解析結果をまとめている。EFIT コードは本共同研究を通じて QUEST にも導入されており、このコードの改善は物理解析にとって重要である。高βｐ放電は、将来中国で建設予定の CFETR での主放電シナリオである。本研究では、EAST で得られた高βｐ放電は高密度化によるもので、高βｐ化によって自発電流が増加することで内部インダクタンスが下がることが示されている。電流分布が計測できている EAST では、内部の電流分布についての議論が可能で、3 種類の密度の放電において明らかな内部インダクタンスの変化が示されている。LHCD＋ECCD 放電における計算した電流密度分布が自発電流の効果で平坦化していることも示され、実験における高βｐ化による電流分布の平坦化と合致することが示されている。最近 QUEST では平衡計算を行うあたり、電流分布の計測の必要性が示されているので、本共同研究で得た知見をもとに検討を進めることとしている。

（様式 11・拠点）

RESEARCH REPORT

Date Feb. 13 2023

Visiting scientist: (name) **Jinping Qian**

(position) **Professor**

(university / institute) **Institute of Plasma Physics,**

Chinese Academy of Sciences

Host scientist: (name) **K. Hanada**

(position) **Professor**

(university / institute) **Kyushu University**

Research period: (from) ________ (to) ________

Research subject: **Develop and improve EFIT code of the plasma equilibrium reconstruction for SSO operation and advanced physical study on QUEST**

Due to COVID-19 pandemic， this year we worked remotely. We analyzed characteristics of current density profile in EAST high poloidal beta scenario. The experimental results are summarized in figure 1, showing the correlation between βp and internal inductance li, revealing the shape of current profile (i.e., decreasing li represents current profile broadening and vice versa.). From this figure, one can find that the current profile becomes broader indicated by lower li at higher βp. On the other hand, figure 1(b) presents the dependence of βp on plasma density, showing elevated βp achieved in higher plasma density. Note that the collected data in figure 1 includes high βp discharges with the heating schemes of both pure RF and NBI plus RF. The current profile broadening with increasing βp can in part attribute to higher bootstrap current considering the proportional relationship between βp and bootstrap fraction.

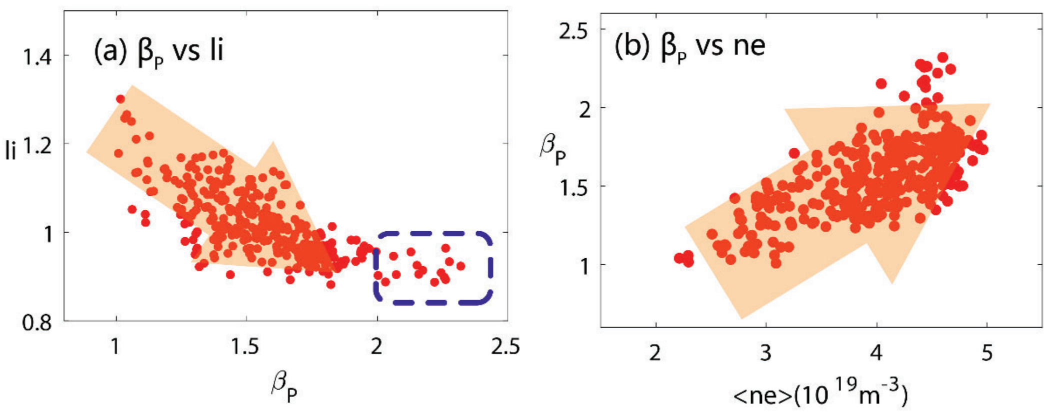

Figure 1. Summary of EAST high βp experiments. (a) correlation between βp and internal inductance and (b) correlation between βp and line-averaged density. Discharges collected in the blue rectangle are driven by both RF and NBI H&CD.

The current profile broadening has been explored by increasing the poloidal beta for higher bootstrap current fraction and changing the LHCD deposition at high density. Figure 2 shows time histories of several parameters for three representative high beta discharges in the development of lower li scenario. Same parameters of Ip=400kA and Bt=2.4T are applied in three discharges while the line-averaged density is set to be 3.0, 3.8 and 4.7 × $10^{19}m^{-3}$, respectively. The internal inductance drops from 1.17 to 0.91 and βp increases from 1.27 to 1.81 with increasing density, indicating that current profiles broaden with increase of both plasma density and βp. Note that even though the ion-cyclotron radio-frequency (ICRF) heating power is applied in three discharges at different time as shown in the shaded area in figure 2(d), there is no effective heating or current drive as no variation is observed in βp and li. The bad coupling of ICRF power may result from limitations of arcing in the ICRF antenna and transmission lines by reflected power.

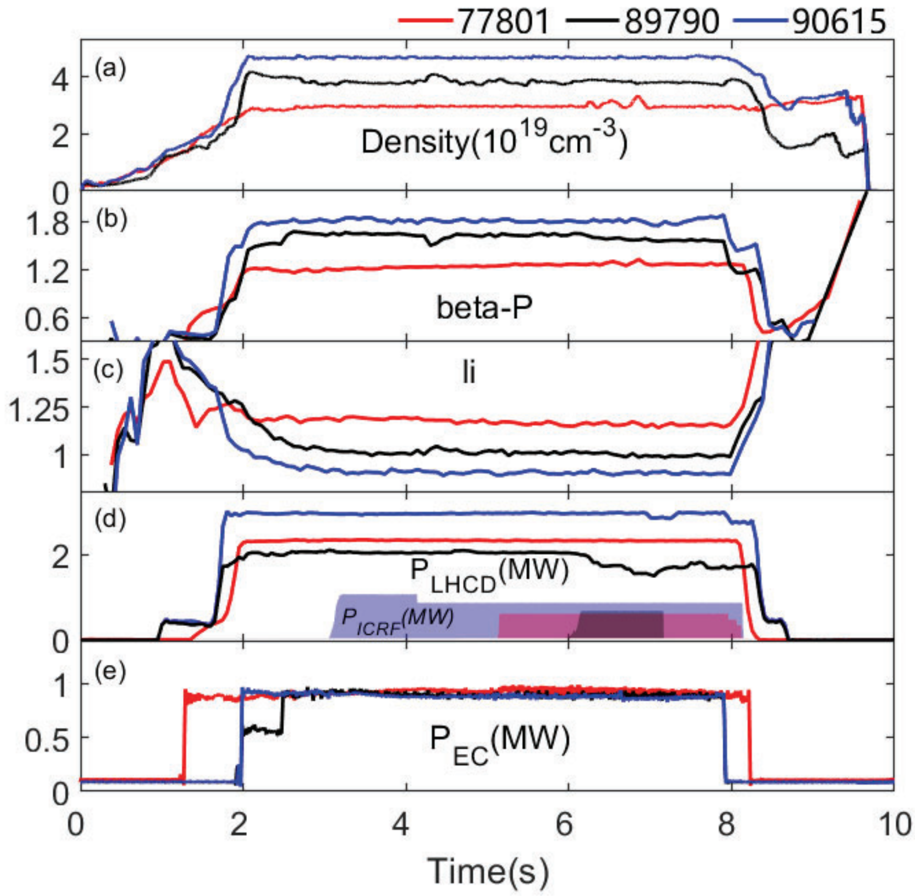

Figure 2. Time histories for EAST shots of #77801, #89790, #90615 with (a) different line averaged density, leading to (b) different βp and (c) internal inductance. Injected power of both LHCD and ICRF in MW is shown in (d), where little effect is observed after application of ICRF in the shaded area; the same flattop power ~ 0.9MW of EC is shown in (e).

Kinetic equilibrium reconstructions constrained by polarimeter-interferometer (POINT) internal measurement and kinetic pressure have been performed, where kinetic pressure consists of density profiles obtained by POINT along with both Thomson scattering (TS) diagnostics and reflectometry, temperature profiles of both electron and ion obtained by TS and X-ray crystal spectrometer (XCS). Note that the ion density is obtained from quasi-neutrality condition and Z_{eff} measurement when there is no direct measurement of ion density diagnostics. The equilibrium reconstruction results are shown in figure 3 combined with density profiles and electron temperature profiles, presenting that the current density profile broadens with increasing density indicated by both safety factor profiles and total current density profiles. However, unlike previous results obtained in L-mode plasmas, where the safety factor profile could grow to be strongly reversed in higher densities, only slight differences are observed in safety factor near core region in H-mode high βp plasmas.

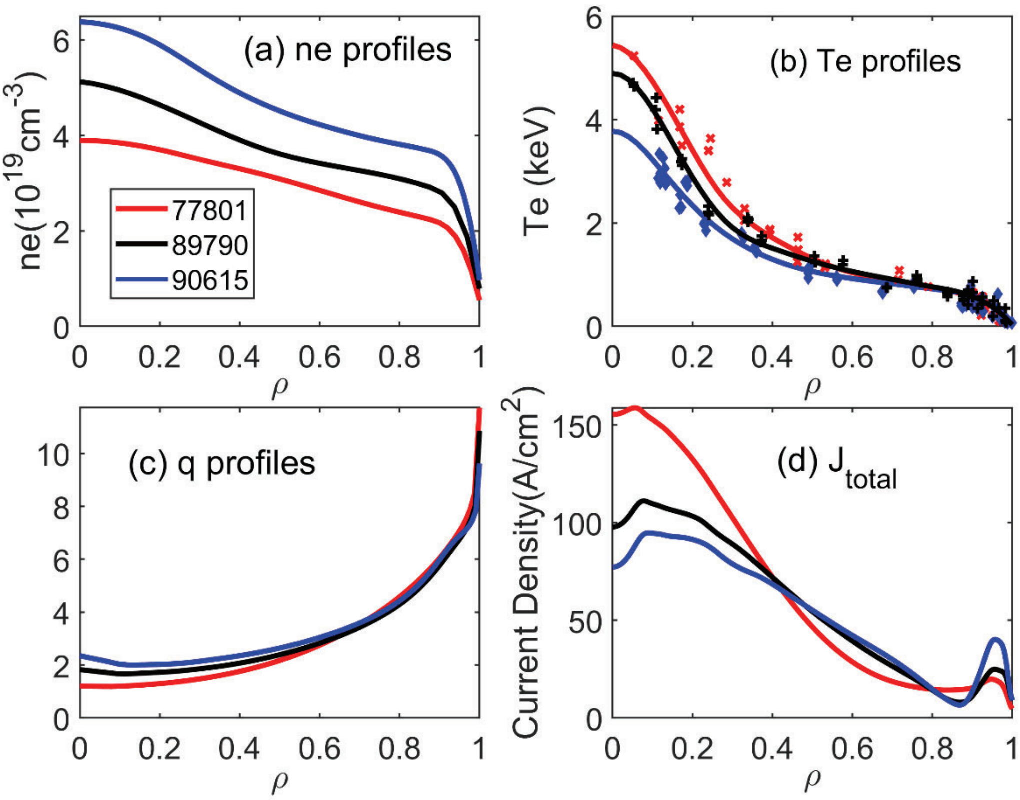

Figure 3. (a) density profiles and (b) electron temperature profiles for discharges #77801, #89790, #90615, note that the scatter points in Te profiles are raw data points came from TS diagnostics. Equilibrium reconstruction results of (c) safety factor profiles and (d) total current density profiles

To understand the current profile broadening in the high βp plasma, fractions of current density are calculated using multiple modelling codes. The results are shown in figure 4. In the simulation, current density profiles and power density profiles of LHCD are obtained from ray tracing code GENRAY and Fokker-Plank code CQL3D with peak $N_{//} = 2.26$, ECCD profiles are simulated by both TORAY code and CQL3D code with toroidal and poloidal angles of EC wave at 200° and 77° respectively, the fraction of bootstrap current is obtained using Sauter model. Note that the radial diffusion of the fast electrons has been considered in CQL3D process for both LHCD and ECCD calculation, where the radial transport diffusion coefficient Dr = 0.9 m^2s^{-1} is applied for LHCD after a list of value scan and Dr = 6 m^2s^{-1} for ECCD when abnormally high value of current drive in the core was obtained using TORAY only. From the results, one can find that the LH current profiles shift outward gradually with increasing density accompanied by decreasing magnitude of current in the core region. Similar trend could be found in LH power density profiles shown in figure 4(b) as well. It is worth noting that the LHCD profile at the highest density case has already shown tendency of off-axis peaking, which is desirable for achieving reverse shear.

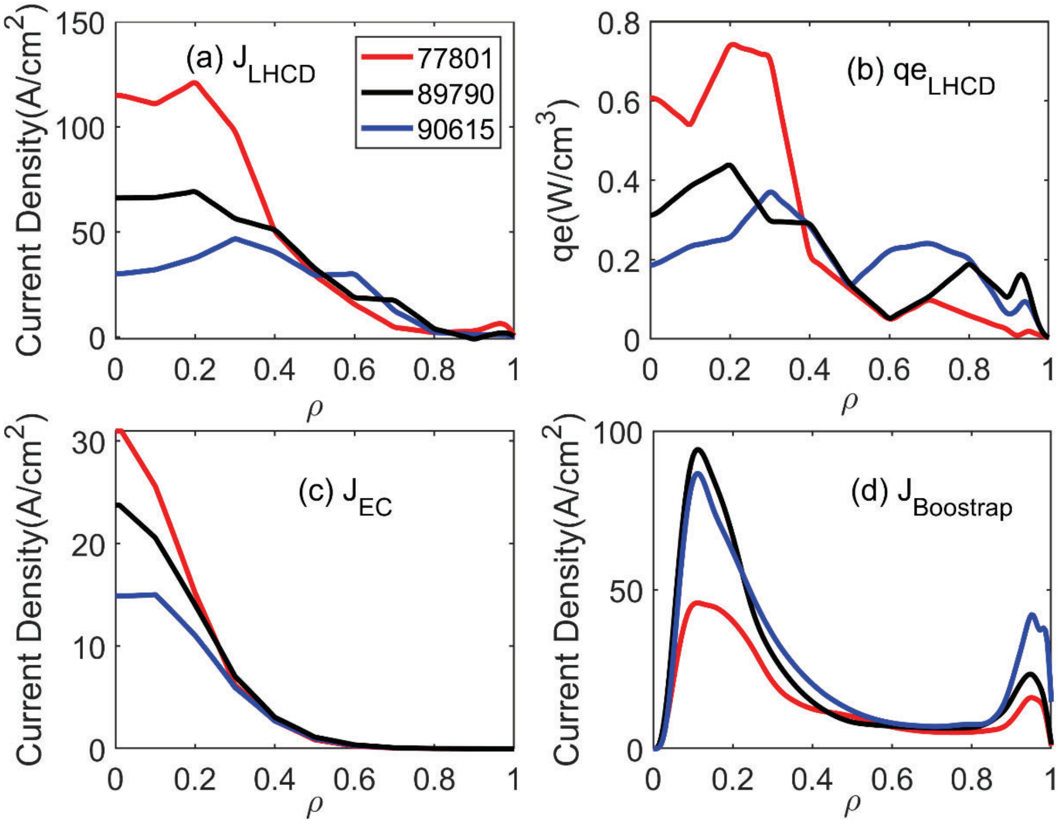

Figure 4. Results of different fractions of current density profiles. (a) current density and (b) deposition power density profiles of LH calculated by GENRAY-CQL3D; (c) current density profiles of EC calculated by TORAY-CQL3D and (d) bootstrap current density profiles by Sauter model.

The characteristics of current density profile in EAST high poloidal beta operation have been demonstrated. By summarizing results of high βp experiments, it is found that parameters of βp, the internal inductance and plasma density are correlated with each other. Higher βp operation is usually achieved with higher density, which would lead to the decrease of li, indicating current density profile broadening. Later analyses in pure RF H&CD discharges with different plasma density confirm that elevated bootstrap current fraction obtained in high βp operation broadens current density profile. Current profile and power density profile of LHCD shifts outward gradually with increasing density, serving as another factor of current profile broadening process.

(Signature) J. Qian

(Name in print) Jinping Qian

国際化推進共同研究概要

No. 14

22NU-11

タ イ ト ル： Joint study of long pulse high beta discharges and related egde turbulence transport in steady state operation (SSO) plasmas on QUEST and EAST

研究代表者： GAO Xiang

所内世話人： 花田　和明

研 究 概 要：下側ダイバータが炭素からタングステンに変更されて熱除去能力の向上が図られて世界的にも有名になった 1056 秒の Super I モード放電（報告書ではこの放電の詳細が示されている。）が実現された。この放電の熱バランス解析を進めており、途中経過を国際土岐会議で発表[1]した。全体の 80%の熱負荷を計測することができたが、まだ計測できてない熱負荷が 20%存在している。EAST が QUEST と同じオールメタル装置となり、今後は粒子バランスが重要になると考えられる。粒子バランスに関する研究は QUEST が進んでおり、その結果は共著で国際会議の招待講演として発表[2]されている。また、現在 IAEA 核融合エネルギー会議 2023 に QUEST の実験結果を共著で発表すべく国内審査に提出している。

国際会議発表

[1] Yunfei Wang, Kazuaki Hanada, Haiqing Liu, Xiang Gao et al., “Power balance investigation in long-pulse high-performance discharges in EAST tokamak” ITC31(2022) P1-3F16

[2] Kazuaki Hanada, …… Xiang Gao, Haiqing Liu et al., “Control of fuel particle recycling using the hot wall on all-metal plasma facing wall in QUEST” IAEA-TM-SSO 2022.11.14-16, Vienna. (Invited Talk)

関係する共著論文発表

[1] Yunfei Wang, Kazuaki Hanada, Haiqing Liu, Xiang Gao et al., ″ Hot spots induced by RF-

accelerated electrons in the scrape-off layer on Experimental Advanced Superconducting Tokamak ″, Nuclear Fusion (2023) Accepted manuscript online. DOI 10.1088/1741-4326/acb726

[2] Yunfei Wang, Kazuaki Hanada, ……, Xiang Gao, et al., “Guiding center orbit simulation of energetic particles in tokamak plasma”, Proceedings of the 8th International Exchange and Innovation Conference on Engineering & Sciences (IEICES 2022).

RIAM JOINT RESEARCH REPORT SUMMARY (English Form)

1. Research ID: No.14_22NU-11

2. Research Title: Joint study of long pulse high beta discharges and related edge turbulence transport in steady state operation (SSO) plasmas on QUEST and EAST

3. Category: International

4. Applicant

Affiliation: Institute of Plasma Physics, Chinese Academy of Sciences

Name: GAO xiang

5. RIAM Attendant: Prof.HANADA Kazuaki

6. Summary (150~200 words in Japanese or 100~150 words in English):

This year, given the situation of COVID-19, the joint research was still done remotely. Steady state operation (SSO) of tokamak plasma is one of the basic requirements for future fusion reactors. Long pulse high beta operation is one of important missions for ITER. Joint study long pulse high beta discharges in SSO plasma research field on QUEST and EAST is strongly supporting ITER experiment from both experience and theory. In 2022, the collaboration research continue focused on the power balance in SSO high performance discharge and coupling of injected energy and plasma during discharge, which is benefit for the SSO high beta discharges of EAST and QUEST. A steady-state plasma with a world-record pulse length of 1056 s was obtained, where the density and the divertor peak heat flux were well controlled, with no core impurity accumulation, and a new high-confinement and self-organising regime (Super I-mode = I-mode + e-ITB) was discovered and demonstrated.

*) Submit either one of Japanese or English forms.

Introduction

This year, given the situation of COVID-19, the joint research was still done remotely.

Steady state operation (SSO) of tokamak plasma is one of the basic requirements for future fusion reactors. Long pulse high beta operation is one of important missions for ITER. Joint study long pulse high beta discharges in SSO plasma research field on QUEST and EAST is strongly supporting ITER experiment from both experience and theory. In this year, the collaboration research continue focused on the power balance in SSO high performance discharge and coupling of injected energy and plasma during discharge, which is benefit for the SSO high beta discharges of EAST and QUEST. A steady-state plasma with a world-record pulse length of 1056 s was obtained, where the density and the divertor peak heat flux were well controlled, with no core impurity accumulation, and a new high-confinement and self-organising regime (Super I-mode = I-mode + e-ITB) was discovered and demonstrated.

New results in 2022

To access long-duration plasmas, experiments have been performed in a double-null magnetic configuration mainly using LHCD and ECRH at Ip =300–400 kA, BT = 2.75 T, R = 1.91 m, and a=0.45 m. BT was chosen to be 2.75 T to simultaneously achieve on-axis ECRH deposition and optimised LHCD power absorption at 4.6 GHz. The line-averaged electron density $\bar{n}$e was approximately 2×1019 m-3. The operational conditions were carefully tuned shot-by-shot, keeping the main parameters, such as heating powers, plasma density, plasma current, and plasma shape, the same.

Both particles and heat exhaust related to plasma–wall interaction must be controlled to operate long pulses. Therefore, real-time feedback control was implemented on EAST using additional relevant techniques. The plasma configuration is double null (DN) during discharge to avoid excessive heat flux on PFCs. A powder dropper was used to inject lithium to mitigate impurities and reduce recycling. This allows control of density and radiated power due to impurities. Note that low particle recycling is favourable for cryo-pumping, which does not suffer from saturation or release of particles back into the plasma when in a low recycling regime.

Repeated tests of the plasma control system were performed each day prior to the experiments to minimise the error due to the offset of integrators of magnetic measurements, which is essential for controlling both the position (zero shift) and shape of the plasmas. Thus, a stable gap (~4 cm) between the plasma and the wall was maintained in the double-null configuration, ensuring sufficient particle exhaust.

After repetitive discharges of hundreds of seconds, a discharge with a duration of 1056 s was achieved, as shown in Fig. 1. A total energy of 2 GJ was injected into the plasma, twice as much as the record previously held by Tore Supra and EAST. The plasma was operated at Ip = 330 kA and $\bar{n}_e = 1.8\times10^{19}$ m^{-3}; it was heated by a total RF power of 1.65 MW (1.1 MW of LHCD at 4.6 GHz, and 0.55 MW of ECRH). As shown in the figure, all the main plasma quantities are stationary during the entire discharge. The radiation power, with tungsten as the major radiating species, is found to be very low (~150 kW). Note that the discharge is fully non-inductive, i.e., the plasma current is mainly driven by LHCD and a moderate bootstrap current (~37%). As illustrated in Fig. 2, in the 1056 s discharge, which is called the Super I-mode, will be described in detail below; the corresponding lower hybrid current drive efficiency estimated by $\eta_{\mathrm{CD}} = \frac{I_{\mathrm{LH}} n_e R}{P_{\mathrm{LH}}} (\mathrm{A/W}/m^2)$ *(23)*is ~0.87×10^{19} A/W/m^2. The current drive efficiency in this discharge is comparable to the experimental value in L-mode plasma, but slightly lower than that in H-mode plasma, where I_{LH} and P_{LH} are the lower hybrid driven current and lower hybrid wave power, respectively.

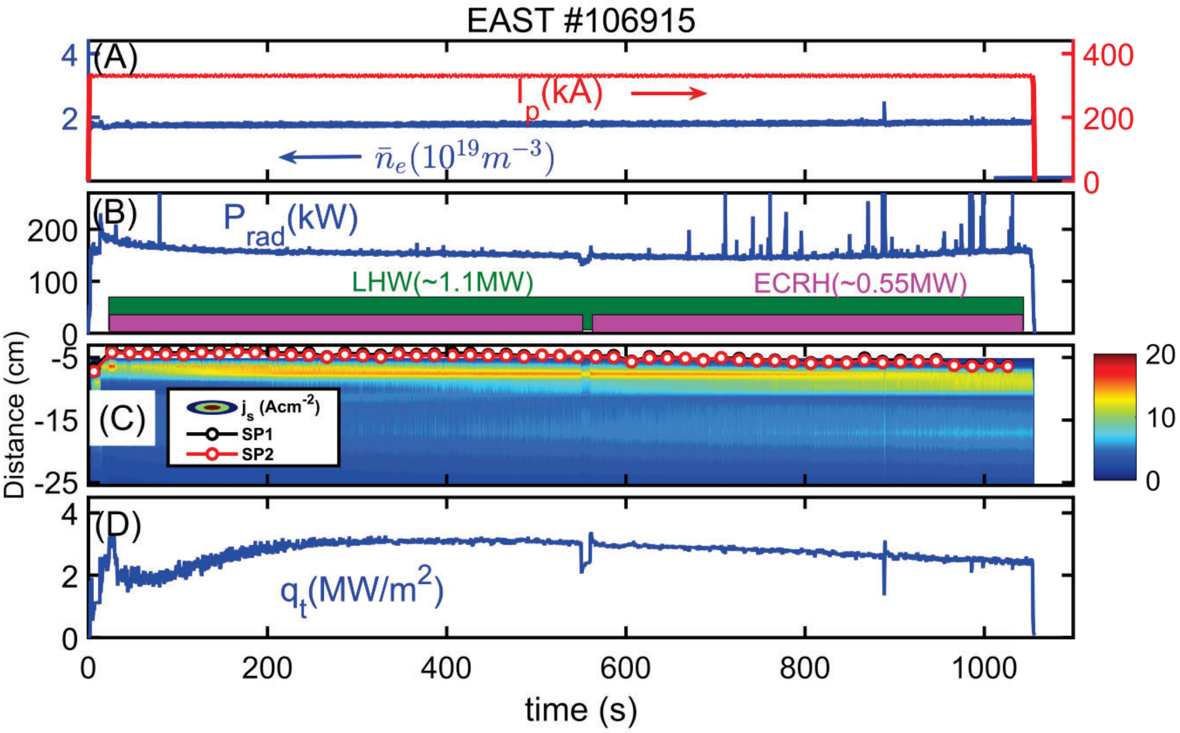

Fig. 1. Waveform of the thousand-second discharge #106915. (**A**) Plasma current I_p and line-averaged electron density $\bar{n}_e$. (**B**) LHCD, ECRH, and radiated powers. (**C**) Contour of particle flux given by the ion saturation current j_s on the divertor target, with the strike points calculated from EFIT equilibrium shown in open circles (SP1 and SP2 are outer strike points for two X-points in double-null configuration, respectively). (**D**) Peak heat flux on the divertor target.

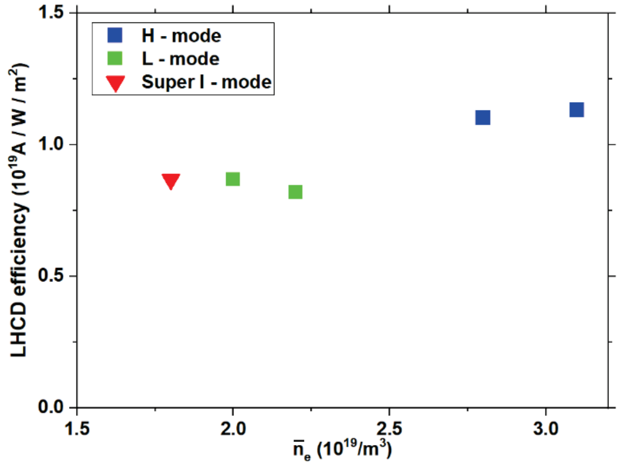

Fig. 2. Lower-Hybrid Current Drive (LHCD) efficiency. Experimental comparison of LHCD efficiency in the L-mode, H-mode and Super I-mode.

Fig. 3 represents the energy confinement enhancement factor H98 as a function of the pulse length for Super I-mode (solid red square), standard I-mode (red square), H-mode (blue triangle), L-mode with ITB (violet circle), and standard L-mode without ITB (black diamond) in EAST. Super I-mode has an energy confinement similar to that of H-mode, but with a pulse length considerably longer than that of H-mode. Further, compared with standard I-mode, Super I-mode exhibits better energy confinement with a 50% higher H-factor. Noted that the present Super I-mode was realized with a very high electron temperature and relatively lower ion temperature. Super I-mode experiments on EAST will be extended towards the case of high ion temperature.

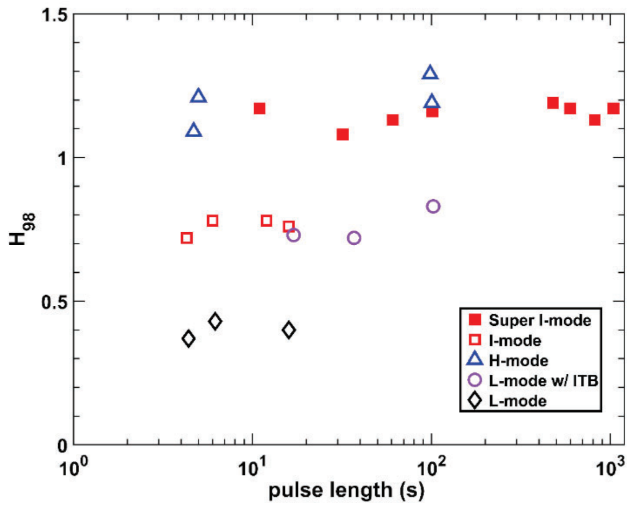

Fig. 3. Comparison of the energy confinement enhancement factor H_{98} and the plasma duration. Various plasma regimes obtained in EAST are compared: Super I-mode (solid red square), standard I-mode (red square), H-mode (blue triangle), L-mode with ITB (violet circle), and L-mode without ITB (black diamond).

Discussions

The major motivation of this project is to realize SSO plasma, based on QUEST and EAST device. In 2022 EAST campaign, we focus on the studying of the wave-plasma physics, such as coupling between LHW power and plasma, for achieving high-parameter SSO of the tokamak. A steady-state plasma with a world-record pulse length of 1056 s was obtained, where the density and the divertor peak heat flux were well controlled, with no core impurity accumulation, and a new high-confinement and self-organising regime (Super I-mode = I-mode + e-ITB) was discovered and demonstrated.

In 2023, this subtheme will continue pursue in long pulse high beta discharges and related pedestal structure and edge turbulence transport in SSO plasma on QUEST and EAST. Comparison and combination study based on the calorimetry and other diagnostics will continue be done on both devices. The combined study will be helpful for understanding the underlying physics and obtaining improved high performance plasma on EAST and QUEST. It is benefit for the long pulse high beta discharges of EAST and QUEST.

Acknowledgement and comments:

Work supported by the international joint research at the Joint Usage of Research Centers for Applied Mechanics for 2022. I would like to thank our host, Professor K. Hanada, who helps a lot during our remotely research and very appreciate the fruitful discussions and comments. We hope that the international joint research at the Joint Usage of Research Centers for Applied Mechanics could continue to enhance China-Japan cooperation on fusion plasma research in the future.

Co-Publications in 2022-2023:

[1] Yunfei Wang, Kazuaki Hanada, Haiqing Liu, Xiang Gao et al., " Hot spots induced by RF-accelerated electrons in the scrape-off layer on Experimental Advanced Superconducting Tokamak ", Nuclear Fusion (2023) Acepted manuscript online. DOI 10.1088/1741-4326/acb726

[2] Yunfei Wang, Kazuaki Hanada, ……, Xiang Gao, et al., "Guiding center orbit simulation of energetic particles in tokamak plasma", Proceedings of the 8th International Exchange and Innovation Conference on Engineering & Sciences(IEICES 2022).

(Signature) Xiang Gao

(Name in print) Xiang Gao

国際化推進共同研究概要

No.15

22NU-12

タイトル： The research on the confinement and loss mechanism of alpha particle through the research of energetic electron on QUEST

研究代表者： JIE Yinxian

所内世話人： 花田　和明

研究概要：

　α粒子の損失は将来の核融合炉である CFETR（中国）や Japan DEMO（日本）の性能に大きくかかわる課題である。CFETR では高βｐ運転が想定されており、本共同研究では米国の TFTR 装置で 1991 年に報告された IPN 配位を参照し、QUEST で得られた高βｐ配位である IPN 配位を研究対象としている。予定では以前設置されていた軟Ｘ線装置を改良してプラズマ全体の計測を行う予定であったが、COVID-19 の影響で進捗が遅れている。高速電子の粒子軌道を計算するコードの整備は完了しているが、IPN 配位での高速電子の損失計測はできていない状況である。将来的には高βｐ配位でのα粒子の損失を高速電子の損失で模擬できるかどうかについても検証する予定である。

今共同研究の内容に直接関連しないが共著論文として

[1] ″Hot spots induced by RF-accelerated electrons in the scrape-off layer on Experimental Advanced Superconducting Tokamak″Wang.Yunfei,... Jie.Yinxian,.... et al .,Nuclear Fusion (to be published.)

がある。

RIAM JOINT RESEARCH REPORT SUMMARY (English Form)

1. Research ID: No.6_21NU-5
2. Research Title: The research on the confinement and loss mechanism of alpha particle through the research of energetic electron on QUEST
3. Category: International
4. Applicant

Affiliation: Institute of Plasma Physics, Chinese Academy of Sciences

Name: Yinxian Jie

5. RIAM Attendant: K. Hanada
6. Summary (150~200 words in Japanese or 100~150 words in English):

Due to COVID-19 pandemic，this year we worked remotely.

Investigation of loss mechanism of the energetic electron in QUEST provides finally a good assistance of confinement of alpha particle in the international thermo-nuclear fusion reactor (ITER) and designing fusion devices such as Japan DEMO and CFETR (China Fusion Engineering Test Reactor) in China. So I discussed the task of particle orbit calculating arranged by Professor K.Hanada with student Mr. Yunfei Wang.

*) Submit either one of Japanese or English forms.

Research subject: The research on the confinement and loss mechanism of alpha particle through the research of energetic electron on QUEST

Due to COVID-19 pandemic, this year we worked remotely.

Soft x-ray spectra system is a very important diagnotic on tokamaks. It is one of the most widely used in measuring the palsma electron tempreture and MHD phenomenons. The whole system needs modification to get more detail date to get the position of IPN and relevant physical research on QUEST.

The mission of QUEST is to develop the scientific basis for achieving a steady state condition at sufficiently high beta (~20%), with high confinement and low collisionality. Operating Tokamak at a high poloidal beta value is usually attactive and this makes the spherical tokamak an interesting choice for future reactors.The maximum achievable β p, however, is limited by a so called equilibrium limit, where an inboard poloidal magnetic field null (IPN) appears at the high field side of the vacuum vessel.Inboard poloidal field null (IPN) configuration in a high Bp discharging was reported first time on TFTR in 1991. In those discharge the evolution of the poloidal field measured at the midplane on the inboard side of the TFTR vacuum vessel was studied.As Ip was ramped down, and Bp increased, the midplane poloidal field decreased and eventually become negative, indicating that the separatrix had crossed the coil position and moved into the vacuum vessel. The separatrixlimited discharge was sustained until the end of the beam heating phase. In QUEST, such an IPN configuration is easily achieved under a high magnetic mirror ratio and high Bz/Bt values ($\approx$ 10%) via electron cyclotron (EC) heating and current drive. A soft x-ray spectra system was set up on QUEST and got some primary date.The whole system needs modification to get more detail date to get the position of IPN on QUEST.

Investigation of loss mechanism of the energetic electron in QUEST provides finally a good assistance of confinement of alpha particle in the international thermo-nuclear fusion reactor (ITER) and designing fusion devices such as Japan DEMO and CFETR (China Fusion Engineering Test

Reactor) in China.

Co-Publications in 2022-2023:

[1] "Hot spots induced by RF-accelerated electrons in the scrape-off layer on Experimental Advanced Superconducting Tokamak"Wang.Yunfei,... Jie.Yinxian,.... *et al* .,Nuclear Fusion （to be published.）

(Signature) Y. Jie

(Name in print) Yinxian Jie

国際化推進共同研究概要

No. 16

22NU-13

タイトル： Joint study of calorimetric measurement of heat load and power balance estimation and measurement and simulation of energetic electrons loss in steady state operation (SSO) plasmas on QUEST and EAST

研究代表者： LIU Haiqing

所内世話人： 花田　和明

研究概要： これまでの共同研究で、中国の超伝導トカマク EAST に SSO 時のパワーバランス計測用の流量計と水温測定器を設置している。下側ダイバータがタングステンに交換される前当時の世界最長の H モードショットを得るために行われた一連の調整放電での熱負荷を解析し、下側ダイバータに形成される Hot spot が SOL 領域でのＬＨ波の衝突吸収が原因であることを見出した。この成果は 2023 年に Nuclear Fusion 誌に共著論文[1]として受理された。QUEST ではパワーバランスに高速電子の寄与が大きく、これを解析するためのコード開発が行われ、その計算方法についても発表[2]されている。また、本共同研究の枠組みから発展した研究として ITB に対する MHD 効果の研究の論文[3]が発表された。

[1] Yunfei Wang, Kazuaki Hanada, Haiqing Liu, Xiang Gao et al., ″ Hot spots induced by RF-accelerated electrons in the scrape-off layer on Experimental Advanced Superconducting Tokamak ″, Nuclear Fusion (2023) Accepted manuscript online. DOI 10.1088/1741-4326/acb726

[2] Yunfei Wang, Kazuaki Hanada, ……, Xiang Gao, et al., "Guiding center orbit simulation of energetic particles in tokamak plasma", Proceedings of the 8th International Exchange and Innovation Conference on Engineering & Sciences (IEICES 2022).

[3] Y. Q.Chu, H.Q.Liu, ……, K. Hanada, et al., ″MHD effect of internal transport barrier on EAST tokamak″, Plasma Science and Technology 24 (2022) 035102.

RIAM JOINT RESEARCH REPORT SUMMARY (English Form)

1. Research ID: No.16_22NU-13

2. Research Title:

Joint study of calorimetric measurement of heat load and power balance estimation and measurement and simulation of energetic electrons loss in steady state operation (SSO) plasmas on QUEST and EAST

3. Category: International joint research

4. Applicant

Affiliation: Institute of Plasma Physics, Chinese Academy of Sciences

Name: LIU Haiqing

5. RIAM Attendant: Prof.HANADA Kazuaki

6. Summary (150~200 words in Japanese or 100~150 words in English):

Due to COVID-19 pandemic， this year the joint research was done remotely. The collaboration research focused on hot spots induced by RF-accelerated electrons in the scrape-off layer on EAST. In 2022, the material of lower divertor has been developed from graphite to tungsten, aiming at achieving higher power handling capability and achieving longer H-mode operations. Combined with the experience of long-pulse operation accumulated in previous rounds of experiments, EAST achieved a long-pulse high-parameter operation with electron ITB with duration 1056.66 s, the plasma configuration is well controlled with improved confinement, called super I mode.

And I have many fruitful discussions with Prof.Hanada's doctor student, Mr. Yunfei Wang, on his doctoral research issues. Three Co-Publications are achieved in 2022-2023.

*) Submit either one of Japanese or English forms.

Introduction

Steady state operation (SSO) of magnetic fusion devices is one of the goals for fusion research. In this year, the collaboration research focused on analyzing and finding the cause of hot spot formation, and comparing the heat load capacity of tungsten and graphite divertors through calorimetry. Hot spots are the outcomes of interactions between the plasma and plasma-facing components (PFCs), which frequently hinder the maintenance of high-performance plasmas through unwanted impurity emissions, such as the longest H-mode discharge on the EAST. Moreover, hot spots can cause the meltdown of PFCs, which results in serious damage to the machine.

Hot spots induced by various radio frequency (RF) power injections have been observed and investigated in EAST and QUEST. The hot spots may be formed by electrons moving along the magnetic field lines that attack the PFCs in the entire SOL.

In the present study, the effect of the SOL magnetic configuration on hot spot formation was investigated in a series of configuration-control experiments, and the magnetic field line tracking in SOL contributed to an intuitive explanation. The findings of this study helped achieve the longest H-mode plasma. Moreover, the energy source of hot spots and the mechanism of hot spot formation were clarified through two-frequency LHW pulse modulation experiments. These experiments showed that collision damping of LHW is a major mechanism for LHW power deposition on the SOL, which subsequently leads to hot spot formation. These results were confirmed through power deposition calculations and a joint simulation between ray-tracing and Fokker–Planck codes.

Recent results in 2022

Preventing impurity emission from hot spots on plasma-facing materials is a critical issue in the maintenance of high-performance plasma on the Experimental Advanced Superconducting Tokamak (EAST). In this study, experimental and theoretical analyses were performed to investigate the mechanism of hot spot formation. In the upper single null magnetic configuration of the EAST, two separatrices were connected to the upper (primary) and lower (secondary) X-points. Experiments on plasma configuration control indicated that the reduction in the gap between the lower (secondary) separatrix and lower hybrid antenna is effective in preventing hot spot formation on the lower divertor, which frequently emits impurities in long-duration discharges. This effectiveness was quantitatively confirmed by magnetic field lines tracking simulation and calorimetric measurement of divertors in the experiment. Two-frequency power modulation of the lower hybrid wave (LHW) was conducted to evaluate power deposition on the scrape-off layer (SOL) during propagation from the LHW antenna to the main plasma. This experiment clarified that LHW-accelerated electrons in the SOL via collision damping deliver their energies to hot spots along the magnetic field line. These findings help alleviate or even eliminate the formation of hot spots and maintain the performance of plasma.

Stable plasma configurations of seven discharges were established from ~2.3 s using the Equilibrium Fitting (EFIT) code; at times before 2.3 s, the configuration changes of these seven discharges exhibited the same trends, and hot spots appeared from ~3 s onwards. Therefore, the temporal evolution (from 3 s to 8 s, at every second) of the positions of the lower outer strike points for #73 991 to #73 998 (except for #73 996) were calculated based on the EFIT reconstruction, as shown in figure 1. The circles in figure 1 represent the heights of the lower outer strike points of these seven discharges in the cylindrical coordinates. Notably, the hot spot and lower outer strike point (from 3 s to

8 s) of all these discharges were on the outer dome of the lower divertor. Figure 6 shows that the distance between the hot spot and lower outer strike point on the divertor had no obvious relationship with the hot spot formation in these discharges, because the position of the lower outer strike point for discharges #73 994 and #73 995 (without hot spots) was almost the same as the discharges with the hot spot.

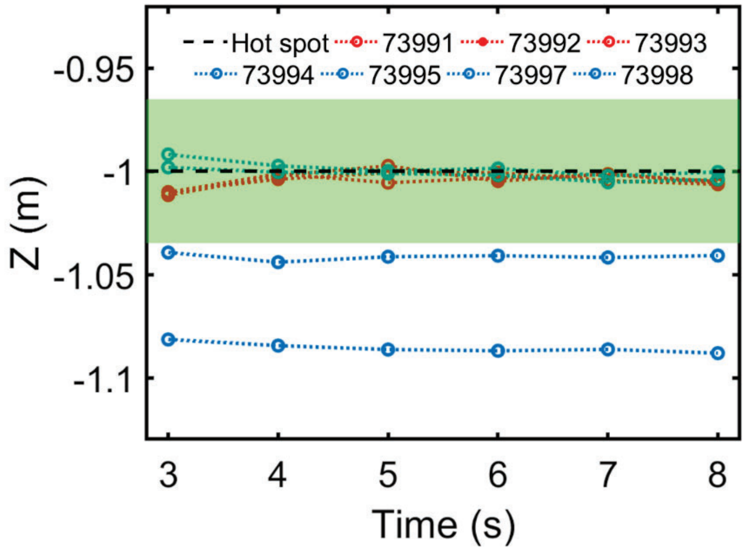

Figure 1. Temporal evolutions of the height positions of the lower outer strike points in cylindrical coordinates. The red circles represent the discharges with hot spots, and the blue circles represent the discharges without hot spots. The black dash line represents the height position of the hot spot on the lower dome, and the green color represents the estimated hot spot area.

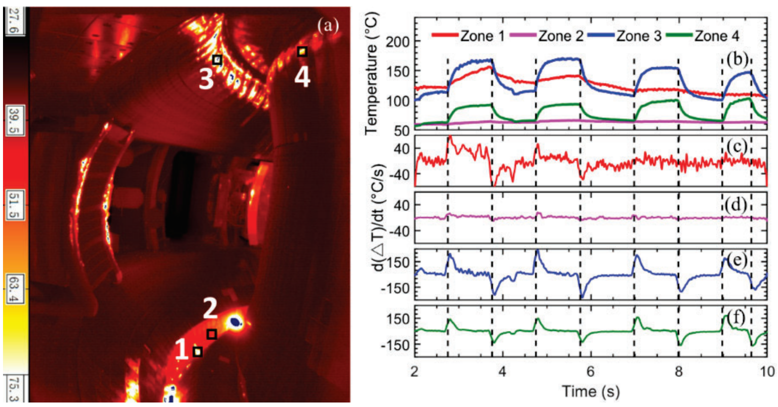

Figure 2. (a) Photograph taken using an IR camera of the vacuum vessel of the EAST and location marks from zones 1 to 4 for discharge #74 864. (b) Temporal evolution of the average temperature (measured using the IR camera) for the four zones marked in figure 14(a). (c)–(f) Time derivatives of temperatures for the four zones.

Figure 2(a) is a photograph acquired using the IR camera in port G; the LHW antenna at 4.6 GHz and its two graphite guard limiters are on the left side of the figure. Figure 14(b) represents the average temperature evolution, and figure 2(c)–(f) shows the time derivatives of the temperature of the four zones over time, marked in figure 2(a). Zones 1 and 2 with and without hot spots, respectively, were on the lower outer divertor; zones 3 and 4 were on the upper outer and inner divertor, respectively. Figure 2(b) shows that the temperature in zone 1 was strongly related to the injection of the LHW at 2.45 GHz; however, after the second heating period of the LHW at 2.45 GHz, the temperature in zone 1 continuously decreased, related to the injection of the LHW at 4.6 GHz. This indicates that the hot spot formation in zone 1 was most likely related to the different performances of the two LHWs. This finding is investigated in the next section.

The temperatures in zone 3 and 4 changed simultaneously with the injection of the LHWs at 2.45 GHz and 4.6 GHz, indicating that the heat load of the upper divertor in the USN configuration discharge originated from the core plasma. Because the time derivative of temperature is directly related to heat flux, figures 2(e) and 2(f) show that the upper divertor can withstand a large heat flux during an LHW injection. Moreover, the location of the hot spot on the lower divertor in zone 1 can also withstand a large heat flux compared with that in zone 2 during an LHW injection at 2.45 GHz, as shown in figures 2(c) and 2(d).

We observed that the collision absorption caused by the LHW at 2.45 GHz was 35.2 kW higher than that of the LHW at 4.6 GHz; this part of energy from the LHW at 2.45 GHz may have caused hot spot formation in the lower divertor, as shown in figure 2(a).

The frequency spectra pertaining to the LHW at 2.45 GHz (blue) and that of the LHW at 4.6 GHz (red) are shown and compared in figure 3. The spectral widths of the two LHWs were almost the same, meaning that the PDI effect is not the primary cause of hot spot formation.

In cases of #73 993 and #73 994, a difference of 3.82 MJ in module E appeared (within 5 s); this was caused by the slight change of the magnetic configuration in the SOL, with 0.43 MW and 1.48 MW being attributed to the LHW injections at 2.45 GHz and 4.6 GHz, respectively. This indicates that, in this calculation, more than 0.76 MW (40% of the LHW power) should be deposited in the SOL, and 20% of the LHW power can expected to be deposited in the SOL through collision damping.

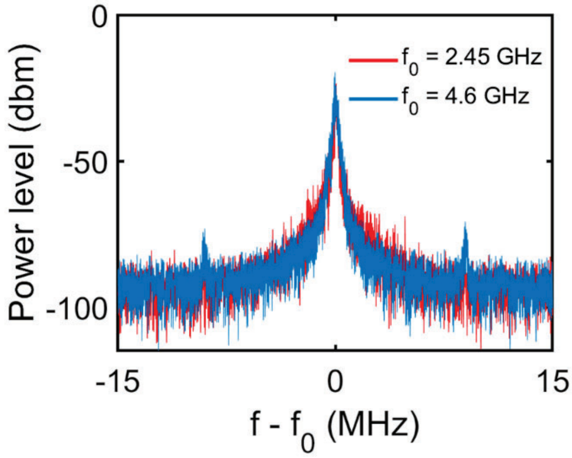

Figure 3. Frequency spectra of the LHWs at 2.45 GHz (red) and 4.6 GHz (blue).

Discussions

This year, the collaboration research focused on the mechanism of the hot spot formation, comparing the heat load capacity of tungsten and graphite divertors through calorimetry. In this year study, we investigated the mechanisms underlying the hot spot formation on the lower divertor during the EAST 2017 campaign and found that two factors, namely the magnetic configuration in the SOL and the energy deposition of the LHW in the SOL, played an important role in hot spot formation. By slightly changing the SOL plasma configuration, the hot spot on the lower divertor was effectively alleviated. This helped achieve a record of steady-state H-mode plasma (#73999) in the EAST for 101.2 s. Experiment analyses and GENRAY/CQL3D simulations showed that the two LHWs had different plasma heating and current driving efficiencies in the main plasma owing to their different frequencies; the LHW at 2.45 GHz likely deposits more energy than the LHW at 4.6 GHz in the SOL through collision damping, which leads to hot spot formation in the LHW modulation experiment.

In this year's joint research, I have many fruitful discussions with Prof.Hanada's doctor student, Mr. Yunfei Wang, on his doctoral research issues. Three Co-Publications are achieved in 2022-2023.

In the near future, the EAST aims to realize a higher performance plasma operation with higher power injection; therefore, it is important to achieve full FoV detection for PFCs on the EAST to monitor the condition of PFCs, including hot spots. Besides, the mechanism of association between the LHW and plasma should be further investigated to improve the efficiency of plasma heating and current driving through the LHW to achieve lengthier H-mode operations and noninductive current driving. These results and further joint research on EAST and QUEST have potential applications in exploring advanced operating modes on CFETR in China and ITER.

Acknowledgement and comments:

Work supported by the international joint research at the Joint Usage of Research Centers for Applied Mechanics for 2022. I would like to thank our host, Professor K. Hanada, who helps a lot during our remotely research and very appreciate the fruitful discussions and comments. We hope that the international joint research at the Joint Usage of Research Centers for Applied Mechanics could continue to enhance China-Japan cooperation on fusion plasma research in the future.

Co-Publications in 2021-2022:

[1] Yunfei Wang, Kazuaki Hanada, Haiqing Liu, et al., " Hot spots induced by RF-accelerated electrons in the scrape-off layer on Experimental Advanced Superconducting Tokamak ", Nuclear Fusion (2023) Aceepted manuscript online. DOI 10.1088/1741-4326/acb726

[2] Yunfei Wang, Kazuaki Hanada, ……, Haiqing Liu, et al., "Guiding center orbit simulation of energetic particles in tokamak plasma", Proceedings of the 8th International Exchange and Innovation Conference on Engineering & Sciences(IEICES 2022).

[3] Y. Q.Chu, H.Q.Liu, ……, K. Hanada, et al., "MHD effect of internal transport barrier on EAST tokamak", Plasma Science and Technology **24** (2022) 035102.

(Signature) Haiqing Liu

(Name in print) Haiqing Liu

国際化推進共同研究概要

No. 17

22RE-1

タ イ ト ル： Development of piezoelectric gels

研究代表者： INSU Jeon

所内世話人： 東藤　貢

研 究 概 要：
本研究では、生体に優しくピエゾ効果を有するセルロースと PVDF を用いて、新規ポリマーゲルを開発した。この 2 種類のポリマーは、構造と特性が大きく異なるものの、開発したハイブリッドゲルは、広範囲な温度領域で、優れた電気的および機械的特性を示していた。開発したゲルは、次世代のエネルギー関連材料として利用価値が高いことが示唆された。

Development of piezoelectric gels

Chonnam National University, Prof. Insu Jeon

Summary

In this research, a novel method is proposed to fabricate stretchable and flexible piezoelectric all gel energy harvesters. Cellulose, a natural biopolymer, with polyvinylidene difluoride (PVDF), an exceptionally piezo active and biocompatible synthetic polymer, were integrated in glycerol, a green organic solvent with extremely high-boiling point and moderately low-freezing point to synthesize the gels. The prepared glycerol gels (GG) exhibited properties with the Young's modulus, tensile strength, compressive strength and piezoelectric charge constant of ~7 MPa, ~2.5 MPa, ~9 MPa and ~2.4 pC N^{-1}, respectively. Moreover, the gels maintained their properties for 7 d over a wide temperature range (−50 to 80 °C). These properties show that the developed gels are prominent candidates for many applications in next-generation stretchable and flexible energy harvesting and energy storage devices.

Method

First, physically isotropic water-equilibrated (Cellulose/PVDF) (x/y) (where x and y are the initial cellulose and PVDF concentrations (wt%), respectively) hydrogels were prepared according to the method described in our previous report with a slight modification. Aqueous glycerol solutions of 25%, 50%, 75%, and 100% glycerol content were used to convert hydrogels to glycerol gels (GG) sequentially for 12, 12, 24, and 24 h, respectively. The as prepared GG was annealed in a closed glass vial at 120 °C for 6 h, whereafter it was slowly cooled to 25°C to obtain the desired Cellulose/PVDF GG (thickness ≈ 2 mm), which was used for further characterization.

Results

A series of (Cellulose/PVDF) (x/y) glycerol gels were fabricated to realize glycerol gel with optimal composition, using the steps illustrated in Figure 1, and evaluated their properties utilizing tensile tests, and electrical output measurements.

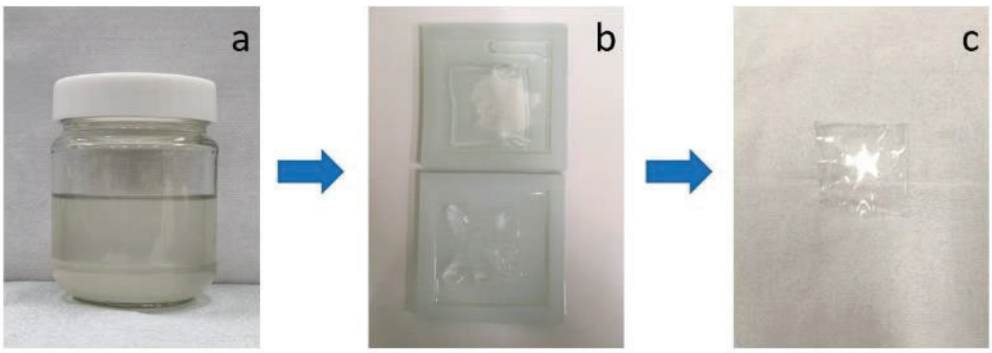

Figure 1. Fabrication process of (Cellulose/PVDF) (x/y) Glycerol gels.

When the PVDF concentration was increased from 0.5 to 2.5 wt% at a set cellulose concentration of 1 wt%, the voltage output and the current output of the glycerol gels increased gradually to a maximum value for PVDF 2 wt% and started decreasing when further increasing the PVDF wt% (Figure 2). Further characterizations were performed for this optimum composition of Cellulose 1 wt% and PVDF 2 wt% glycerol gel. The piezoelectric output of the glycerol gels strongly depended on the final PVDF concentration and relative cellulose and PVDF concentration in the gels.

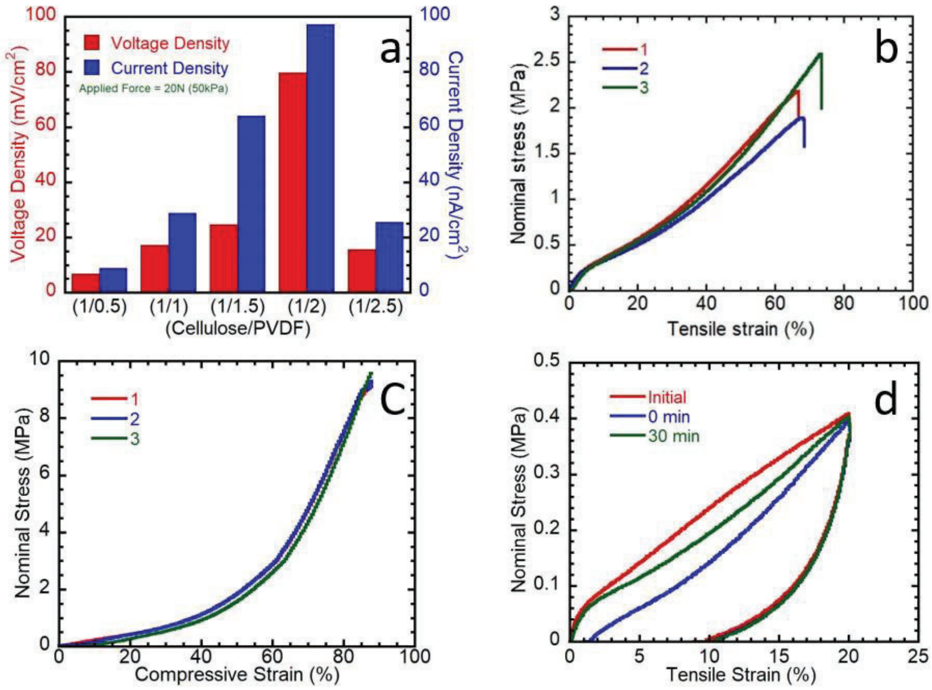

Figure 2. (a) Output voltage density and current density (under 20 N tapping force) of the isotropic (Cellulose/PVDF) glycerol gels prepared by varying the PVDF concentration in the range of 0.5–2.5 wt% at a set cellulose concentration of 1 wt%. Cellulose/PVDF (1/2) wt% glycerol gel, (b) tensile stress–strain (500% strain rate per min), (c) compressive stress–strain (20% strain rate per min), and (d) time evolution of residual strain (100% strain rate per min) curves at 25 °C.

Conclusion

A novel class of gels were developed by integrating cellulose and PVDF, which are bio-friendly, piezo active polymers, in glycerol, a green organic solvent. Even though there are significant differences in structure and properties of the polymers, a hybrid gel with excellent electrical and mechanical properties, and extremely high stability over a wide temperature range was fabricated following the proposed fabrication method. Considering these remarkable properties and facile synthesis, the developed gels are expected to have high potential for numerous applications in next-generation flexible energy harvesting and energy storage devices.

国際化推進共同研究概要

No. 18

22RE-2

タ イ ト ル: Coupled numerical framework development of hybrid floating offshore wind turbine (FOWT) and oscillating water column (OWC) wave energy converters with power take-off (PTO) control

研究代表者： ZHANG Dahai

所内世話人： 劉　盈溢

研究概要： 浮体式洋上風力発電機と振動水柱型（OWC）波力発電機の統合は、ハイブリッド洋上再生可能エネルギーの有望なソリューションとして注目されていた。周波数領域に基づく従来の方法とは異なり、本研究では、統合された空力、水力、弾性、制御、係留における時間領域連成数値ツールを開発した。数値解析結果は、様々な環境条件での 1:50 スケール実験モデルに対して検証した。さらに、OWC の動力取出し制御策が提案された。設計した制御策は、従来の線形減衰制御と比較して、浮体構造物の運動応答と風力発電機の構造荷重を軽減するのに有効であることがわかった。具体的には、浮体のピッチ運動を 15% 軽減し、タワーベースの疲労荷重も 6% 減少された。このような数値的な枠組みに基づき、多目的最適パワーテイクオフ制御設計に関する更なる研究を行うことができる。

国際化推進共同研究報告書

No.18_22RE-2

タ イ ト ル:　Coupled numerical framework development of hybrid floating offshore wind turbine (FOWT) and oscillating water column (OWC) wave energy converters with power take-off (PTO) control

研究代表者:　ZHANG, DAHAI （Zhejiang University）

所内世話人:　劉 盈溢

Introduction

Offshore wind energy plays an important role in accelerating the transition of global net-zero greenhouse gas emissions [1]. In deep water areas, the floating offshore wind turbine (FOWT) is regarded as a more feasible and economical form than fixed-bottom solutions [2]. However, FOWT still has a high cost of energy (CoE) due to the expensive floating platform and mooring system. At the same time, there will be more vigorous motions and structural loads due to the additional motion degree of freedom (DoF), which may increase the failure risk and shorten the operational lifetime.

In order to reduce the CoE and improve the dynamic behaviour of FOWT, many studies have been carried out on the integrated optimisation of floating platforms [3], wind turbines [4], and mooring system configuration [5] etc. Alternatively, as there usually exists abundant wave energy in deep-sea regions [6], integrating wave energy converters (WECs) into the floating platform could not only increase the overall energy production [7], but also possibly reduce the motion responses and structural loads of FOWT by the synergy effect between the floating platform and WECs [8]. Therefore, combining FOWT with WECs has been widely seen as a promising solution for improving its power gain and load behaviour [9]. Compared with oscillating-body devices, oscillating water column (OWC) WECs have better reliability due to the structural simplicity, as the only moving component is the air turbine located above water level. Therefore, incorporating OWC WECs into FOWT could be a more promising solution in aspects of cost and reliability.

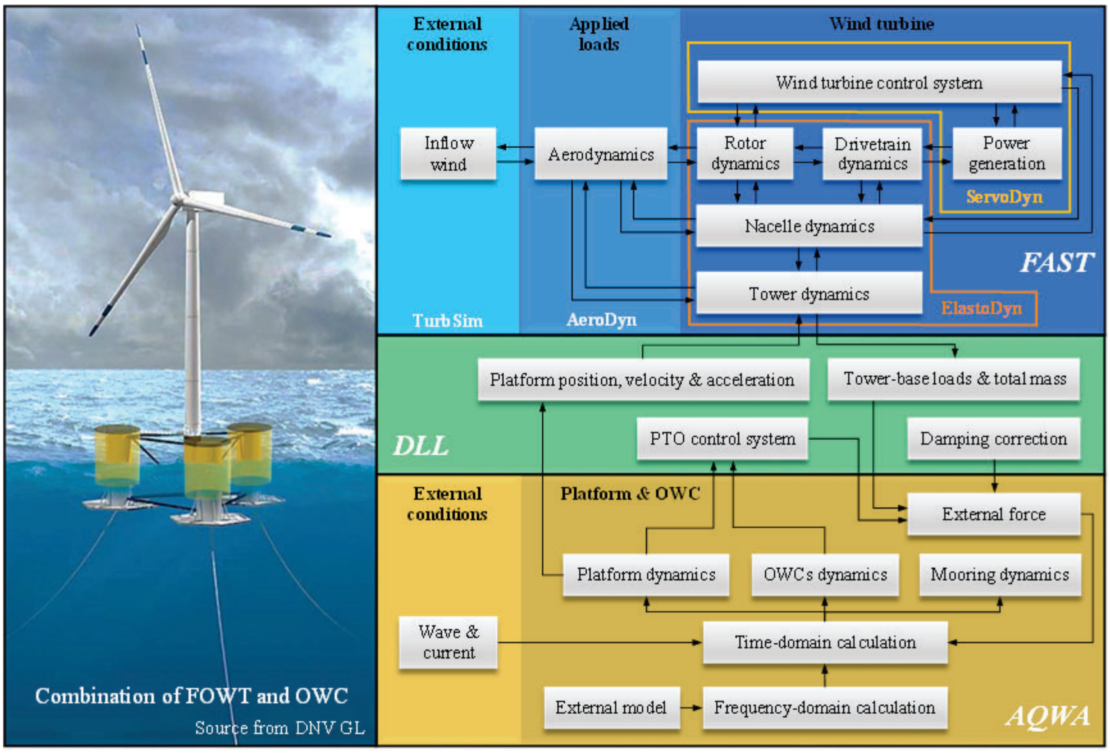

Fig. 1 The aero-hydro-servo-elastic-mooring coupled numerical framework for FOWT-OWC dynamic analysis.

In this study, an aero-hydro-elastic-servo-mooring coupled numerical framework is introduced for integrated time-domain analysis of FOWT-OWC hybrid platforms in this work. This framework is established by coupling the offshore structure hydrodynamic and mooring analysis tool ANSYS-AQWA [10] with the wind turbine aero-elastic code FAST [11]. In particular, the OWC is modelled as an equivalent virtual oscillating body within AQWA environment so that the time-series of OWC free surface variation could be obtained, and then the OWC PTO control effect on wave energy production as well as platform motion could also be evaluated. Moreover, the multi-body dynamics of utility-scale wind turbines are described by FAST so that the ultimate and fatigue loads on critical structures, such as the tower and blades, could be assessed. In order to demonstrate the feasibility of the established coupled numerical framework, a DeepCwind-OWC combined design is proposed and seen as the study case in this work, where the coupled numerical simulation results have been compared and validated against the experimental data of a 1:50 scale model wave basin test. Furthermore, different OWC PTO control strategies have been comparatively studied to investigate their influence on platform motion responses, wind turbine fatigue loads, as well as overall power production.

Methodology

The coupling between AQWA and FAST is achieved through the user-defined DLL and FAST modules, as shown in Fig. 1. FAST modules, such as AeroDyn for aerodynamics, ServoDyn for control, and ElastoDyn for structural dynamics, are completely compiled into the DLL, which could be called by AQWA during time-domain simulations. In particular, the OWC WEC is modelled as an equivalent virtual oscillating body in AQWA, and the formulations of OWC viscosity correction and PTO control actuation are also compiled into the DLL. More details of the established numerical framework are described below.

Platform and Mooring Modelling

The hydrodynamic loads of the floating platform are calculated within AQWA based on linear potential flow theory with viscosity correction. It is assumed that flow is inviscid, incompressible, and irrotational. The added mass, radiation damping, viscous drag effect, and OWC-platform hydrodynamic interactions are all included in the AQWA simulation. The motion equation of the platform can be represented in an integral convolution form as

$$\left(M + A_{\infty}\right)\ddot{X}(t) + C\dot{X}(t) + K(t) + \int_0^t R(t-\tau)\dot{X}(\tau)d\tau = F_{hydro}(t) + F_{mooring}(t) + F_{tower}(t) + F_{OWC}(t) \tag{1}$$

where M is the platform mass, A_{∞} is the added mass matrix at infinite frequency, C is the damping matrix, K is the stiffness matrix, R is the velocity impulse function matrix, and τ is the variable of the convolution term. X denotes the displacement vector. The external loadings include the hydrodynamic loads F_{hydro}, the mooring loads $F_{mooring}$, the tower-base loads F_{tower} acting on the platform, and the OWC induced loads F_{OWC}. Besides, the lumped-mass approach is adopted for modelling the mooring system.

Wind Turbine Modelling

FAST is used in the proposed numerical framework to predict the dynamic response and structure loads of utility-scale horizontal wind turbines mounted on floating platforms. In this work, the HydroDyn module within FAST is not used since the hydrodynamic loads are calculated in AQWA. The aerodynamics are calculated by AeroDyn based on the blade element momentum approach. The wind turbine control, including generator-torque control, blade-pitch control, and yaw control, is handled by the ServoDyn module. The wind turbine blades and tower are modelled as flexible bodies with prescribed mode shapes for structural load calculation, and the dynamics of the turbine could be solved through the ElastoDyn module based on Kane's equation [12]

$$\boldsymbol{F}_r^* + \boldsymbol{F}_r = 0 \tag{2}$$

where $\boldsymbol{F}_r^*$ is the generalised inertia force vector, and $\boldsymbol{F}_r$ is the generalised active force vector.

Oscillating Water Column Modelling

The OWC is modelled as an equivalent point absorber in the proposed framework within AQWA.This rigid water column with the same density of seawater is assumed to have only one motion DoF along the vertical axis. Here, the viscous effect is simplified as linear damping, the coefficients of which could be approximated from model test results through parametric identification. Then, the dynamics of the assumed rigid OWC could be described by the following equation based on the Cummins theory

$$\left(M^{OWC} + A_\infty^{OWC}\right)\ddot{z}(t) = F_{buoy}^{OWC}(t) + F_{radiation}^{OWC}(t) + F_{viscous}^{OWC}(t) + F_{excitation}^{OWC}(t) + F_{PTO}^{OWC}(t) \tag{3}$$

where M^{OWC} is the mass of the equivalent point absorber, A_∞^{OWC} is the added mass of the point absorber at infinite frequency, z is the heave displacement of the point absorber, F_{buoy}^{OWC} is the hydrostatic restoring force, $F_{radiation}^{OWC}$ is the radiated force acting on the body, $F_{viscous}^{OWC}$ is the viscous damping force, $F_{excitation}^{OWC}$ is the excitation force acting on the body bottom, and F_{PTO}^{OWC} denotes the pneumatic force acting on the water free surface. Based on this approximation approach, the time-domain variations of the OWC free surface and wave power production could be evaluated within the same numerical dynamic analysis framework of FOWT.

Experimental Validation

In order to evaluate the feasibility of the proposed aero-hydro-elastic-servo-mooring coupled numerical framework, a novel hybrid FOWT-OWC concept is proposed in this work, and numerical simulations for a number of environmental conditions have been conducted based on the established coupled framework. At the same time, experimental results for 1:50 scale model wave basin tests are also presented for comparison and validation, as shown in Fig. 2.

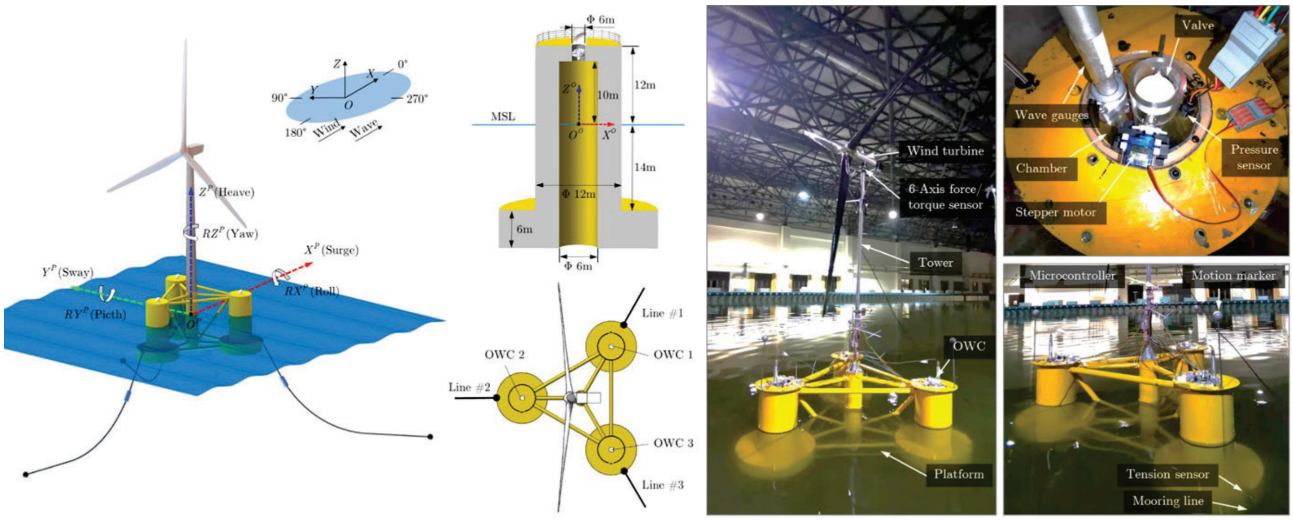

Fig. 2 Concept Description and the 1:50 Scale model of the DOC concept.

The PTO damping is caused by the air pressure variation inside the OWC chamber due to the free surface oscillation and the air mass flow through the top outlet. It is assumed that the OWC thermodynamic processes are isentropic and adiabatic, involving incompressible ideal gas [13]. Thus, the air mass flow through the top outlet is expected to be equal to the air mass variation in the chamber, which can be represented as

$$\dot{m}_{air}(t) = \frac{d}{dt}\left[\rho_{air}(t) \cdot S_{chamber} \cdot \left(L_0 - z(t)\right)\right] \tag{4}$$

where m_{air} is the air mass in the chamber, ρ_{air} is the air density in the chamber, $S_{chamber}$ is the cross-sectional area of the chamber, L_0 is the vertical distance between the mean sea level and the chamber top, and $\dot{z}$ is the relative velocity between the internal free surface and the platform column in the water oscillation direction. Then, the instantaneous wave power production of each OWC can be obtained by

$$P_{OWC} = \Delta p(t) \cdot S_{chamber} \cdot \dot{z}(t) \tag{5}$$

where Δp is the increased pressure in the chamber relative to the atmospheric pressure. In the experiment, tuning the valve opening will lead to different PTO damping coefficients, which can be approximated by the following linearised function

$$B_{PTO} = \frac{\Delta p(t) \cdot S_{chamber}}{\dot{z}(t)} \tag{6}$$

where the B_{PTO} denotes the equivalent PTO damping coefficient [14].

The obtained PTO damping fitting results for 5 ° valve opening under regular waves with different periods are shown in Fig. 3, where a strong linear correlation can be observed. Then, the OWC PTO damping force in the established time-domain numerical framework could be determined by the identified linear damping coefficient table and OWC internal free water surface elevation velocities, thus enabling the OWC PTO control design and assessment for FOWT-OWC hybrid platforms.

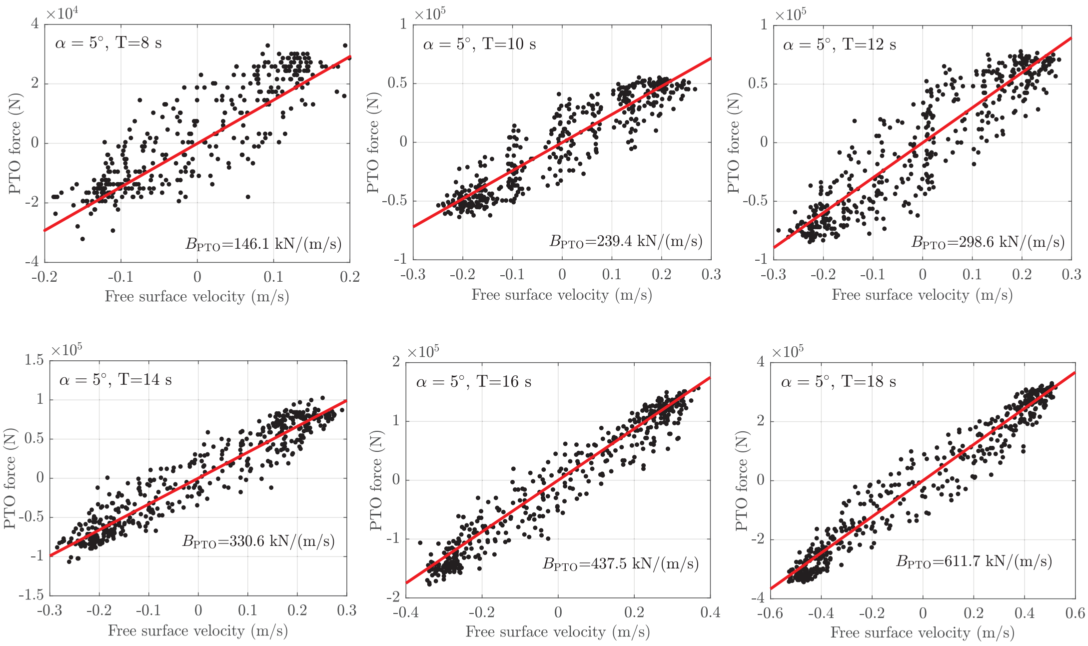

Fig.3 PTO damping fitting results for OWC under regular waves with different periods (α = 5 °).

Results

Regular Wave Tests

The regular wave tests without wind loads have been carried out with different PTO damping configurations. The examined wave height is 3 m in full scale with a series of typical wave periods from 6 s to 18 s, and four openings are set to 5 °, 30 °, 60 ° and 90 °.

Experimental and numerical result comparisons for the platform motion RAOs under regular waves with different periods are shown in Fig. 4. It is shown that the numerical results agree well with the measured data, but still, there are certain deviations. Especially for pitch motion, when the wave period is between 10 s to 16 s, the numerical model over-predicts the RAO, while it is under-estimated when the wave period is 8 s and 18 s. It is also worth noting that a resonance peak can be observed for platform pitch motion at the wave period around 10 s, which corresponds to the OWC natural frequency [15].

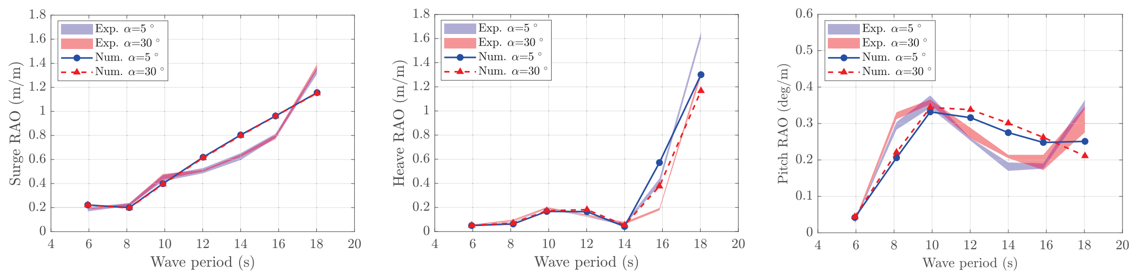

Fig.4 Comparisons of motion RAOs between experimental and numerical results with valve openings 5 ° and 30 °.

Irregular Wind and Wave Tests

To further investigate the prediction performance of the proposed numerical model, two irregular wave tests with wind loads have also been conducted. The JONSWAP spectrum with factor γ=3.3 is used for irregular wave generation, and the OWC valve opening is set to 30 ° for these cases. The wind generation system in the wave basin is used to bring wind loads on the rotor, and the corresponding aerodynamic thrust has been measured by the 6-Axis force/torque sensor. Then, the obtained data is scaled up and imposed onto the rotor in the numerical time-domain analysis process in order to ensure the consistency of the aerodynamic loads between experiments and simulations.

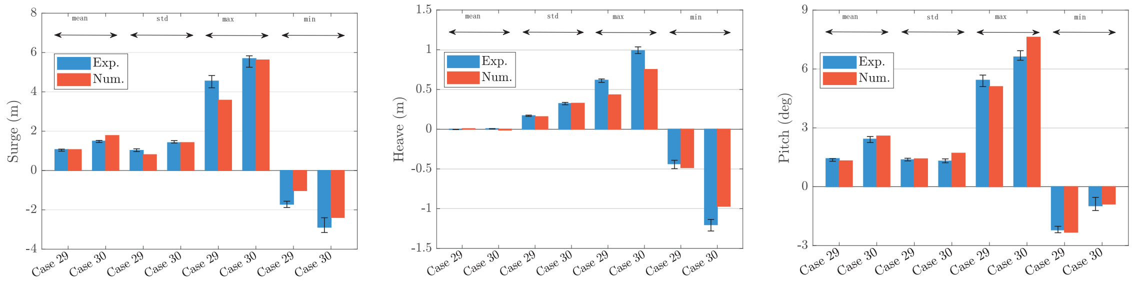

Fig.5 Result comparison of DOC platform motion responses.

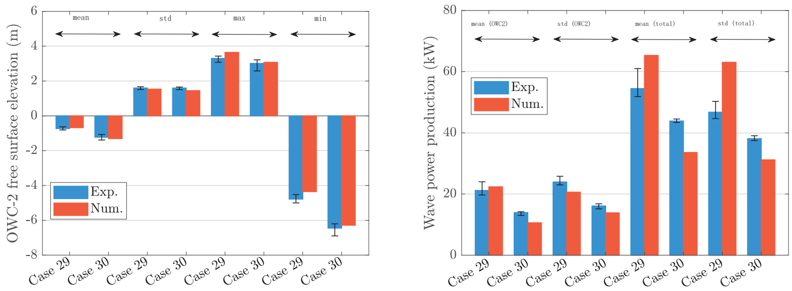

Fig.6 Result comparisons of OWC free surface response and power production.

Statistical comparisons of the DOC platform motion responses under selected combined wind-wave test conditions are presented in Fig. 5, which again shows data consistency. Fig. 6 presents the result comparison of OWC free surface responses and wave power production, where good agreement can also be observed.

In summary, it can be seen that, compared with scale model wave basin experimental test results, the proposed numerical framework can well predict the dynamic responses of FOWT-OWC hybrid platforms as well as the OWC free surface variation and wave power production, demonstrating the feasibility of the established coupled numerical framework [16].

References

[1] Council G W E. GWEC| GLOBAL WIND REPORT 2021[J]. 2017.

[2] Michailides C, Gao Z, Moan T. Experimental study of the functionality of a semisubmersible wind turbine combined with flap-type wave energy converters. Renewable Energy, 2016, 93: 675-690.

[3] Xu S, Murai M, Wang X, et al. A novel conceptual design of a dynamically positioned floating wind turbine[J]. Ocean Engineering, 2021, 221: 108528.

[4] Hegseth J M, Bachynski E E, Martins J R R A. Integrated design optimisation of spar floating wind turbines[J]. Marine Structures, 2020, 72: 102771.

[5] Xu K, Larsen K, Shao Y, et al. Design and comparative analysis of alternative mooring systems for floating wind turbines in shallow water with emphasis on ultimate limit state design[J]. Ocean Engineering, 2021, 219: 108377.

[6] Zhang H, Zhou B, Zang J, et al. Optimisation of a three-dimensional hybrid system combining a floating breakwater and a wave energy converter array[J]. Energy Conversion and Management, 2021, 247: 114717.

[7] Kamarlouei M, Gaspar J F, Calvario M, et al. Experimental study of wave energy converter arrays adapted to a semi-submersible wind platform[J]. Renewable Energy, 2022, 188: 145-163.

[8] Perez-Collazo C, Pemberton R, Greaves D, et al. Monopile-mounted wave energy converter for a hybrid wind-wave system[J]. Energy Conversion and Management, 2019, 199: 111971.

[9] Astariz S, Iglesias G. Selecting optimum locations for co-located wave and wind energy farms. Part I: The Co-Location Feasibility index[J]. Energy Conversion and Management, 2016, 122: 589-598.

[10] ANSYS A. AQWA Theory Manual [J]. Canonsburg, PA 15317, USA, 2013.

[11] Jonkman J M, Buhl Jr M L. FAST user's guide[J]. Golden, CO: National Renewable Energy Laboratory, 2005, 365: 366.

[12] Lackner M A, Rotea M A. Passive structural control of offshore wind turbines[J]. Wind energy, 2011, 14(3): 373-388.

[13] Cengel Y A, Boles M A, Kanoglu M. Thermodynamics: an engineering approach[M]. New York: McGraw-hill, 2011.

[14] So R, Bosma B, Ruehl K, et al. Modeling of a wave energy oscillating water column as a point absorber using wec-sim[J]. IEEE Transactions on Sustainable Energy, 2019, 11(2): 851-858.

[15] Zhang D, Chen Z, Liu X, et al. A coupled numerical framework for hybrid floating offshore wind turbine and oscillating water column wave energy converters[J]. Energy Conversion and Management, 2022, 267: 115933.

[16] Chen Z, Rong Z, Yu H, et al. Control Oriented Modelling of Oscillating Water Column Wave Energy Converters[J/OL]. Proceedings of the CSEE, 2022.

国際化推進共同研究概要

No.19

22RE-3

タ イ ト ル: AI-based Interactive Integrated Design, a novel method for Floating Offshore Wind Turbines Design and Optimisation

研究代表者: HU Zhiqiang

所内世話人: 胡　長洪

研 究 概 要:
浮体式洋上風力発電システム用のセミサブ型浮体の運動特性解析に Software-in-the-Loop 法と AI 技術を応用する国際化推進共同研究について今年度は予定通り実施した。特に、SADA 手法に対して検討を行い、有望な成果が得られた。R4 年１月に応研で開催されたオンライン国際研究集会「The 1st International Symposium on Marine Renewable Energy System Dynamics」に参加し、「Offshore Wind and Artificial Intelligence: real-time monitoring and predictive maintenance for offshore wind turbines」のタイトルで共同利用成果の発表を行い、参加者との研究交流を行った。

Report for 2022 RIAM International Joint Research Project

[22RE-3]

AI-based Interactive Integrated Design, a novel method for Floating Offshore Wind Turbines Design and Optimization

Zhiqiang Hu
Marine, Offshore and Subsea Technology, School of Engineering, Newcastle University, UK

Collaboration research between RIAM Kyushu University and MOST group, Newcastle University was initiated at the beginning of year 2022, aiming to propose an AI-based interactive Integrated Design and Optimization method. This method is proposed based on the concept of SADA proposed by Zhiqiang Hu and Peng Chen in year 2020. The fundamentals of SADA were introduced on RIAM symposium in year 2021 and an engineering practice case-of-study was also presented on RIAM symposium in year 2022. Although the Newcastle University research team couldn't attend the RIAM symposiums at Kyushu University in person due to pandemic, the collaborative research outcomes were disseminated during the symposiums online.

After the symposium of year 2022, Zhiqiang Hu led his research team and devoted into investigations on AI+FOWTs, on purpose of improving the SADA concept to a higher level which is suitable for real engineering practice and benefit offshore wind industry. During the year of 2022, the collaborative research outcomes are listed as below.

1) The 3rd International Symposium on Novel Computational and Experimental Methods for Complicated Fluid-Structure Interactions was held online at RIAM Kyushu University in Jan 2022. Zhiqiang Hu made a presentation on the topic of 'Application of SADA method on Dynamic Performances Analysis of FOWT: Case of Study with Full-Scale Hywind Data'.

2) During year 2022, the collaborative research is carried out to propose the AI-based Interactive Integrated Design method, simplified as IID. This investigation also received kind support from ORE Catapult UK, as they provided the valuable suggestions and experiences from UK offshore wind industry. The IID method aims to find a trade-off design method and reconcile the contradictions between the wind industry and offshore industry. During the development of floating wind farm in UK, there are existing some contradictions between wind turbine design companies and offshore companies, due to the commercial confidential. IID uses AI technology to reconcile this contradiction and it is expected that the IID method will be proposed by mid of year 2023.

   Besides the proposing of IID method, the collaborative research teams also began an investigation on the application of IID to digital twin level and propose IID+ method. This IID+ digital twin will be started in year 2023.

3) Based on the research in year 2022, a collaborative conference paper entitled 'Dynamic

Performance Prediction of Hywind Floating Wind Turbine based on SADA Method and Full-Scale Measurement Data' has been published on MARTECH Conference 2022. This paper summaries the advantages of SADA method and its engineering values. The first author, Dr Peng Chen presented this paper online in MARTECH2022 Conference and a fruitful discussion was made after the presentation.

In year 2023, the collaborative research between Newcastle University and Kyushu University will be conducted to a further step. The research will be extended to enhance IID method to a higher level to be IID+, which will include the digital twin engineering practice. In UK, there are high demands for the development of digital twin system application for offshore wind farms to effectively reduce cost of O&M. In addition, the research team is also extending collaborations with experts in Geotechnology field, aiming to build the digital twin system not only serve for wind farm structures, but also for sea environment monitoring. This is a very new idea and it is expected more fruitful research outcomes will emerge in year 2023.

国際化推進共同研究概要

No.20

22RE-4

タイトル: CFD Simulation of Offshore Wind Turbine in Realistic Ocean Environment

研究代表者: LI Ye

所内世話人: 胡　長洪

研究概要:

本国際化推進共同研究について、共同研究・研究集会とも予定通り実施した。共同研究について、浮体式洋上風車に関する高性能CFD手法の開発や、複雑洋上風況のモデリングに関する研究などが行われ、関連の研究成果は 8 編の学術論文に纏められ投稿された。R5年2月24日にオンライン国際研究集会「The 1st International Symposium on Marine Renewable Energy System Dynamics」が開催され、中国、韓国、英国、台湾から 6 件、日本から 6 件の講演があり、洋上風力ファームに関する数値シミュレーション、各種の海洋再生可能エネルギー技術の研究開発などに関して有意義な国際研究集会となった。

Report for 2022 RIAM International Joint Research Project

[22RE-4]

CFD Simulation of Offshore Wind Turbine in Realistic Ocean Environment

Ye Li
School of Naval Architecture, Ocean and Civil Engineering, Shanghai Jiao Tong University, China

1. Purpose

Offshore wind turbine (OffWT) and onshore wind turbine (OnWT) have different working conditions, design loads and wake characteristics. In-depth analysis of the influence of the incoming atmospheric characteristics and wake evolution characteristics of OffWT and OnWT on the design value of wind turbines is important to reduce the cost and improve the power coefficient. In order to understand the differences between OffWT and OnWT, this joint research project focuses on the analysis of atmospheric conditions, wakes and their interactions with wind turbine loads. The project also provides an opportunity for researchers, including but not limited to SJTU and RIAM, to exchange knowledge on the renewable energy research.

2. Research Plan

This research project is planned for two years. FY 2022 is the first year of the project. The major research topic is the development of wind turbine simulation methods, advanced atmospheric turbulence generation methods and wave models for the ocean waves, especially on the wake and load analysis of wind turbines under typical offshore and onshore atmospheric conditions. At the end of FY2023, as the main event of this international joint research project, the 1st International Symposium on Marine Renewable Energy System Dynamics will be carried out. Researchers involved in this joint research project will present and discuss their research progresses.

The members involved in this collaborative research are shown in the following table.

Researcher’s Name	Name of University or Institute	Present Status or Grade (graduate students)	Researcher role
Ye Li	SJTU	Professor	Representative person (CFD)
Changhong Hu	RIAM	Professor	RIAM Attendant
Zhiteng Gao	SJTU	Assistant Professor	Co-researcher (CFD)
Xiaobo Zheng	SJTU	Associate Professor	Co-researcher (CFD)
Shangming Wang	SJTU	Assistant Professor	Co-researcher (CFD)
Hongliang Wang	SJTU	Assistant Professor	Co-researcher (CFD)
Seiya Watanabe	RIAM	Assistant professor	Co-researcher (CFD)
Yingyi Liu	RIAM	Research Fellow	Co-researcher (CFD)

3. Summary of Collaboration Research

In 2022, due to the epidemic and international travel restriction, the discussions have been made between the two research groups through the Internet. Main topics that have been studied include (1) next generation CFD development; (2) wind turbine and wake modeling; (3) advanced atmospheric turbulence generation methods; (4) machine learning application to hydro- and aerodynamic analysis and (5) related ocean renewable energy technologies. Most of the research results will be presented at the 1st International Symposium on Marine Renewable Energy System Dynamics, which will be held in a hybrid way in 24 February 2023.

Research papers related to this joint research project in 2022~2023 are listed as follows.

[1] Fan Z, Li S, Gao Z, Zhang L, Zheng X, Zhu W, Shen W, Sjoholm M, Mikkelsen T, Wang T, Li Y*. On the importance of wind turbine wake boundary to wind energy and environmental impact. Energy Conversion and Management, 2023, 277:116664.

[2] Leng J, Wang Q, Li Y*. A geometrically nonlinear analysis method for offshore renewable energy systems—Examples of offshore wind and wave devices. Ocean Engineering, 2022,250: 110930.

[3] Gao Z, Feng X, Zhang Z, Liu Z, Gao X, Zhang L, Li S, Li Y*. A brief discussion on offshore wind turbine hydrodynamics problem. Journal of Hydrodynamics, 2022, 34(1): 15-30.

[4] Zhang L, Li Y*, Xu Wenhao, et al. Systematic analysis of performance and cost of two floating offshore wind turbines with significant interactions. Applied Energy, 2022, 321: 119341.

[5] Zheng X and Li Y*. Aerodynamic response of a pitching foil to vortex shedding - some inspiration for the vertical-axis wind turbine. 3rd International Symposium on Novel Computational and Experimental Methods for Complicated Fluid-Structure Interactions, online, January 21st, 2022.

[6] Zhang L, Li Y, Zhao Z, Hu C, Chen M. Numerical and Experimental Study of a 1MW Semi-submersible Wave Energy Floating Platform. Renewable Energy. (Under review)

[7] Xu W, Li G, Zhao R, Zhang L, Shi H, Li S, Gao Z, Hu C, Li Y. Feasibility analysis of large-scale offshore vertical-axis wind turbines. Energy Conversion and Management. (Under review)

[8] Wang H, Zheng X, Pröbsting S, Li Y, Wang Q, Hu C. An Unsteady RANS Simulation of The Performance of An Oscillating Hydrofoil at High Reynolds Number. (Under second round review)

As a main event of this international joint research project, 'The 1st International Symposium on Marine Renewable Energy System Dynamics' will be held on February 24, 2023. Due to the global pandemic situation of COVID-19, the symposium will be held online. On the symposium, overseas and domestic scholars are invited to present their recent researches on their recent research results on development of computational and experimental methods for complicated fluid-structure interactions. The program of the symposium is as follows.

The 1st International Symposium on Marine Renewable Energy System Dynamics

Organized by Research Institute for Applied Mechanics, Kyushu University

Date: February 24, 2023 (From 10:10 Japan time)

Venue: Research Institute for Applied Mechanics (RIAM), Kyushu University
6-1 Kasuga-koen, Kasuga, Fukuoka 816-8580, Japan
Online participation:
https://riam-kyushu-u-ac-jp.zoom.us/j/82592030283 (ID: 825 9203 0283, PW: riam0224)

TIME TABLE

10:10 -10:20	Opening Address by Changhong Hu

Session 1 ***Advanced CFD for Wind Turbine Simulation***

10:20 - 11:00	**Takanori Uchida** (RIAM, Kyushu University) Invited Lecture Wind Turbine Wake Simulation by using RIAM-COMPACT LES Model
11:00 - 11:30	**Seiya Watanabe** (RIAM, Kyushu University) Numerical Simulation of Wind Farm by Lattice Boltzmann Method
11:30 - 12:00	**Yos Panagaman Sitompul** (Tokyo Institute of Technology) Simulation of Foam Formation Using LBM with MPF Model and AMR Method, Incorporating a Large Number of Bubbles

12:00 - 13:00	Lunch break

Session 2 ***Ocean Renewable Energy Technologies***

13:00 - 13:30	**Ye Li** (Shanghai Jiao Tong University, China)

	An overview of China-Australian Jiont Research Center for Offshore Wind and Wave Energy Harvesting
13:30 - 14:00	**Yusaku Kyozuka**, Yusuke Kitajima, Gin Miake, Yuichi Yokoi (Nagasaki University) A Wave Energy Convertor Making Use of Eccentric Rotating Mass Device
14:00 - 14:30	**Ryoya Hisamatsu**, Tomoaki Utsunomiya (Kyushu University) Experimental and Theoretical Investigation on the Dynamics of a Water Intake Riser for a Floating OTEC
14:30 - 15:00	**Lei Li** (Zhenjiang Ocean University, China) Study on Vortex-Induced Motion Characteristics and Suppression of a Circular Cylinder

15:00 - 15:20	Break

Session 3 ***Offshore Wind Energy Technologies***

15:20 - 16:00	**Shiu-Wu Chau** (National Taiwan University, Taiwan) *Invited Lecture* Performance Prediction of a 15MW Floating Wind Turbine System Using Semi-Submersible Taida Floating Platform in the Hsinchu Offshore Area
16:00 - 16:30	**Zhiteng Gao** (Shanghai Jiao Tong University, China) Aerodynamic Characteristics of Wind Turbine in Plateau Area
16:30-17:00	**Watchara Tongphong** (Korea Maritime & Ocean University, Korea) A Fully Coupled Aero-Hydrodynamic Analysis of a 10 MW Floating Offshore Wind Turbine using High-Fidelity Computational Fluid Dynamics
17:00 - 17:30	**Xiaobo Zheng** (Shanghai Jiao Tong University, China) Experimental and numerical study on the aerodynamic response of a pitching foil to the vortex shedding
17:30 - 18:00	**Zhiqiang Hu** (Newcastle University, UK) Offshore Wind and Artificial Intelligence: real-time monitoring and predictive maintenance for offshore wind turbines

18:00 - 18:10	Closing Address by Ye Li

Contact:
Changhong HU, Professor
Research Institute for Applied Mechanics, Kyushu University
6-1 Kasuga-koen, Kasuga, Fukuoka 816-8580, Japan

国際化推進共同研究概要

No.21

22RE-5

タ イ ト ル：Numerical prediction of annual power production of wave farms at an Australia or Japan localised site under multi-directional irregular sea wave conditions

研究代表者： DING Boyin

所内世話人： 劉　盈溢

研究概要： 波力発電所とは、海の波のエネルギーを利用するために、海中に設置された変換器の集合体である。波力発電所は通常、海岸線や沖合の島々の近くなど、波が強く一定のパターンを持つ場所に設置される。波力発電装置間の流体力学的な相互作用と、現地での波浪スペクトルが発電に不可欠である。本研究では，点状吸収装置からなる波力発電所における海洋波の多重散乱を検討した。また、波力発電所の年間性能を評価するための数値計算法を提案した。

Introduction

Ocean waves can supply a significant source of clean and renewable energy due to the vast ocean area on the earth [1]. The ocean wave energy can be harnessed by a wave farm, a group of wave energy converters that are deployed together in the ocean to generate electricity from the kinetic energy of ocean waves. Wave farms locate near the coast or offshore and typically consist of multiple devices, such as floating buoys, oscillating water columns, or other wave energy converters, that are connected to the electrical grid. A conceptual design of wave farm is shown in Figure 1.

At present, there are some challenges associated with wave farms [2]. Due to that the technology is still in its early stages of development, the cost of deploying and maintaining wave farms can be high. Additionally, wave energy converters must be designed to withstand harsh conditions of the ocean environment, which can be challenging and expensive. This study investigates the multiple scattering of ocean waves in a wave farm consisting of arrays of heaving point absorbers. A numerical method is proposed to evaluate the annual performance of the wave farm.

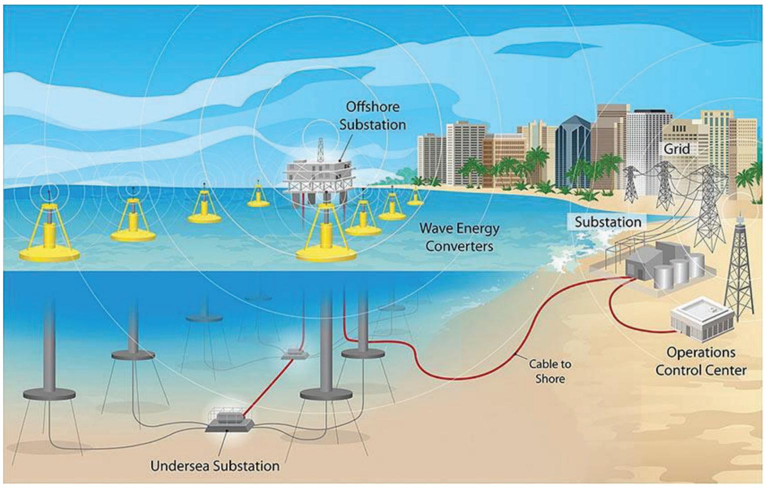

Figure 1 A conceptual design of wave farm. Illustration by Alfred Hicks, NREL [3].

Methodology

Let us consider a train of regular incident waves that propagates to the positive x-direction with a small amplitude A, a heading angle β measured from the positive x-axis, and a wave number k, in water of a finite depth h. The ambient wave potential incident to body j can be written as

$$\phi_j^A(x_j, y_j, z_j) = -\frac{\mathrm{i}gA}{\omega}\frac{\cosh k(z_j+h)}{\cosh kh}e^{\mathrm{i}k[(x_j+\bar{x}_j)\cos\beta+(y_j+\bar{y}_j)\sin\beta]}, \tag{1}$$

where $(\bar{x}_j, \bar{y}_j, 0)$ refers to the origin of the local coordinate system of body j in terms of the global Cartesian coordinates and (x_j, y_j, z_j) refers to an arbitrary spatial point in terms of the local Cartesian coordinates. By converting the local Cartesian coordinates to the polar coordinates (r_j, θ_j, z_j), Eq. (1) can be expanded as a summation of partial cylindrical waves incident to the body j in the form of matrices

$$\phi_j^A(x_j, y_j, z_j) = \{a_j^I\}^T\{\psi_j^I\}, \tag{2}$$

where $\{a_j^I\}$ is a scalar vector of expansion coefficients, and $\{\psi_j^I\}$ is a scalar vector of the basis function that is also named as the incident partial wave component.

In arrays of floating bodies, each individual body experiences not only the ambient incident plane wave but also the outgoing waves that are scattered from all the other neighboring bodies in the arrays. Based on Graf's addition theorem, the scattered waves from body *i* can be expressed as incident waves to body *j* as the following equation

$$\phi_i^S(r_i, \theta_i, z_i) = \{A_i^S\}^T [T_{ij}] \{\psi_j^I\}, \tag{3}$$

where $\{A_i^S\}$ is a scalar vector of the scattering coefficients, and the *T*-transfer matrix yields

$$[T_{ij}]_{nn}^{mq} = \begin{cases} H_{m-q}(kL_{ij}) e^{\mathrm{i}\alpha_{ij}(m-q)}, & n = 0, \\ K_{m-q}(k_n L_{ij}) e^{\mathrm{i}\alpha_{ij}(m-q)} (-1)^q, & n \geq 1. \end{cases} \tag{4}$$

Using a so-called diffraction transfer matrix $[D_j]$ as the form that is defined in Liu et al. [4] based on the hybrid dipole-source formulation, the scattered wave from body *j* and all the incident waves to the same body can be connected based on the following relation

$$\{A_j^S\} = [D_j] \left(\{a_j^I\} + \sum_{i=1, i \neq j}^{N_B} [T_{ij}]^T \{A_i^S\} \right), \quad (j = 1,2, \dots N_B), \tag{5}$$

where N_B is the number of wave energy converters. From Eq. (5), scattering coefficients and the wave potentials can be solved numerically. Wave excitation forces, etc., can be calculated via pressure integration over each body using matrix operations.

Wave farm assessment

It is common to use the so-called interaction factor to evaluate the performance of arrays of wave energy converters. The interaction factor q is defined as a function of the wave number k and the incident wave angle β [5]

$$q(k, \beta) = \frac{k}{N_B P_W} \left(\sum_{i=1}^{N_B} P_j(k, \beta) \right)_{max}, \tag{6}$$

where $P_j(k, \beta)$ is the maximum absorbed power of each device in the farm, P_W is the time-averaged incident wave power per unit crest width

$$P_W = \frac{\rho g A^2 \omega}{4k} \left(1 + \frac{2kh}{\sinh 2kh} \right). \tag{7}$$

At a localised site in irregular waves, the annual power production of a wave farm can be evaluated as

$$P_{Annual} = \sum_{T_p} \sum_{H_s} \Psi(H_s, T_p) J(H_s, T_p), \tag{8}$$

where $\Psi(H_s, T_p)$ denotes the occurrence probability and $J(H_s, T_p)$ denotes the power matrix. These are both functions of the significant wave height H_s and the peak wave period T_p.

Results

As a wave farm usually comprises several arrays of devices, hydrodynamic interactions amongst arrays are investigated first [6]. An example is shown as below. Figure 2 presents the variations of the q-factor vs the device spacing s, the wave heading angle β, and the wave angular frequency x for a uniform line array consisting of seven CorPower-like point absorbers. The most distinctive result herein is that there are some remarkable "bright spot" regions, indicating that the wave energy absorption there is locally optimized against wave conditions. With regard to a uniform line array, it is found that the lower the wave frequency is, the larger the wave heading tends to be in association with the center of a spot region. In addition, the number or the density of the spot regions are found to increase with the device spacing.

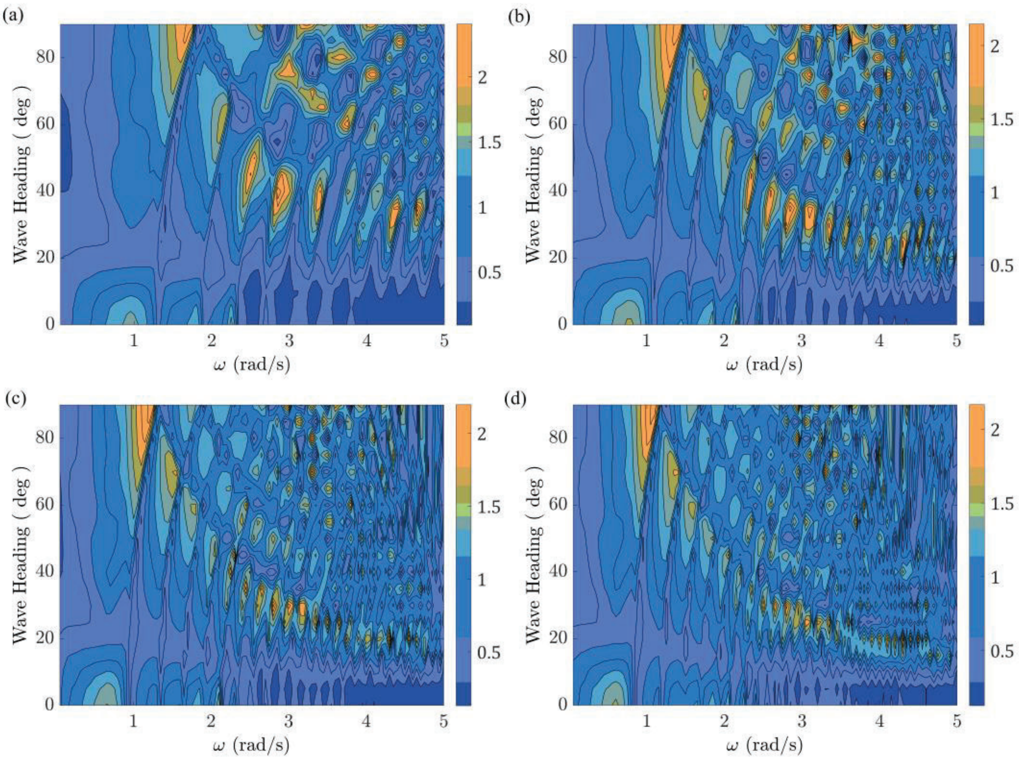

Figure 2. q-factor variation of a uniform line array of wave energy devices against the angular frequency x, the wave heading β, and the device spacing s (h = 100 m): (a) $s = 2D$, (b) $s = 3D$, (c) $s = 4D$, and (d) $s = 5D$.

References

[1] Isaacs, J. D., and Schmitt, W. R., "Ocean energy: Forms and prospects," Science 207, 265–273 (1980).

[2] Astariz, S., & Iglesias, G. (2015). The economics of wave energy: A review. Renewable and Sustainable Energy Reviews, 45, 397-408.

[3] https://www.nrel.gov/water/wave-array.html

[4] Liu, Y., Liang, H., Kashiwagi, M., & Cong, P. (2021). Alternative approaches of evaluating diffraction transfer matrix and radiation characteristics using the hybrid source-dipole formulation. Applied Ocean Research, 114, 102769.

[5] Fitzgerald, C., and Thomas, G., "A preliminary study on the optimal formation of an array of wave power devices," in Proceedings of the 7th European Wave and Tidal Energy Conference, Porto, Portugal (2007), pp. 11–14.

[6] Liu, Y., Zheng, S., Liang, H., & Cong, P. (2022). Wave interaction and energy absorption from arrays of complex-shaped point absorbers. Physics of Fluids, 34(9), 097107.